12-2020

Embedded-Atom-Method Modeling of Alkali-Metal/Transition-Metal Interfaces

Jake D. Christensen
Utah State University

EMBEDDED-ATOM-METHOD MODELING OF ALKALI-METAL/TRANSITION-METAL INTERFACES

by

Jake D Christensen

A thesis submitted in partial fulfillment
of the requirements for the degree

of

MASTER OF SCIENCE

in

Physics

Approved:

D. Mark Riffe, Ph.D. Major Professor	Charles Torre, Ph.D. Committee Member
T.C. Shen, Ph.D. Committee Member	Janis L. Boettinger, Ph.D. Acting Vice Provost of Graduate Studies

UTAH STATE UNIVERSITY
Logan, Utah

2020

ABSTRACT

Embedded-Atom-Method Modeling of Alkali-Metal/Transition-Metal Interfaces

by

Jake D Christensen, Master of Science

Utah State University, 2020

Major Professor: D. Mark Riffe, Ph.D.
Department: Physics

Bimetallic interfaces become increasingly important as technological devices shrink down to the nanoscale. The smaller a device is, the larger the ratio of surface area to volume, making surface effects more prevalent. It is important to study surface influenced properties (such as heat transport) to understand these systems. This thesis applies the Embedded Atom Method (EAM) model to several bimetallic systems, which include slabs of tungsten and molybdenum oriented to the (110), (100), and (111) surfaces, with adsorbate layers of alkali metals.

In this project, we develop a computer program called Alkali Lattice Explorer (ALE) to perform the calculations to characterize the vibrational properties of bimetallic surface systems. We then develop models of the potential energy interaction of homogeneous tungsten, molybdenum and the alkali metals. We use these potential energy models to construct a heterogeneous potential, using the Johnson prescription. Our work shows that this prescription fails to accurately describe the interaction between atoms of very different sizes. We develop a new model of the interaction between the alkali and transition metals. This potential energy model is used to calculate dispersion curves, densities of states, and Debye temperatures of several systems of interest.

(162 pages)

PUBLIC ABSTRACT

Embedded-Atom-Method Modeling of Alkali-Metal/Transition-Metal Interfaces

Jake D Christensen

Understanding the thermal properties of materials is essential to using those materials for technological advancement which can benefit civilization. For example, it has been proposed that essential components of tokamaks, devices which perform fusion, be made out of tungsten with a thin layer of lithium on the surface. To that end, this thesis seeks to calculate the thermal properties of a layer of alkali atoms, like lithium and sodium, on tungsten and molybdenum substrates. We use an Embedded Atom Method (EAM) model to perform our calculations. This type of model has been widely used to describe the interaction between atoms of the same type (i.e., how two lithium atoms interact). There is also a standard prescription for building the interaction between two atoms of different types (i.e., how a lithium atom and a tungsten atom interact). However, we have discovered that the prescription fails when trying to describe the interaction of atoms with much different sizes. To remedy this, we explore several different types of models and compare their results.

ACKNOWLEDGMENTS

This work could not have been completed without the love and support from my friends and family. Although I am listed as the author of this thesis, I am just a single member of a large network of people who have come together to help complete this research.

I would like to thank Dr. Mark Riffe for his mentorship and guidance. I have always admired Dr. Riffe's organization and methodical approach to research, teaching and presentations, and I thank him for taking the time to show me how to step back and look at the bigger picture. I cherish the skills and mindset I learned from him, and hope to put them to good use in the future.

I want to thank my colleagues in the Physics department. It was incredibly helpful to be able to go them to bounce off new ideas or get some quick feedback. Quick, small, seemingly insignificant interactions with friends have have helped me see new approaches to problems, and put things in a clearer perspective.

Finally, I especially want to acknowledge the contributions of my wife, Rebecca. Much of this thesis was written during the Covid-19 quarantine, and there is simply no way this work could have been completed without her constant love and support. I want to thank her for helping me with the transition to the stay-at-home orders, and quickly adapting to an entirely new way of life.

Jake D Christensen

CONTENTS

LIST OF TABLES

LIST OF FIGURES

CHAPTER 1
INTRODUCTION

Bimetallic interfaces are important for several technological reasons, especially at the nanoscale. In this size regime the fraction of material close to an interface can be quite large, often resulting in the dominance of interfaces on key physical properties of devices. A most important property is heat transport.

One of the main theoretical approaches to modeling interfacial heat transport utilizes embedded-atom-method (EAM) modeling of the interactions between atoms. EAM models have been extensively used in molecular dynamics simulations to study the transmission and reflection of thermal energy at interfaces between dissimilar metals [1–3].

As a practical example, there has been recent work done on studying the effectiveness of using tungsten (W) and molybdenum (Mo) as first wall divertors for tokamak reactors. These materials boast important properties for fusion, such as a high melting point, high thermal conductivity, high physical sputtering threshold energy, and low tritium retention [4–6]. However, when subject to the high-energy neutron irradiation environment of a tokamak, W and Mo tend to suffer defects such as voids and dislocations [7]. It has been proposed that adding a layer of liquid lithium to the wall can help overcome these challenges [8]. Our investigation into the interaction of Li on Mo and W will add to the understanding of this important sytem.

In order to begin to investigate inter-facial physics, we propose to study single-layer alkali metal (AM) atoms adsorbed onto transition-metal (TM) substrates. Our study shall reveal key vibrational properties associated with the AM/TM interface, including dispersion relations and densities of states, from which thermal properties such as specific heat, entropy, and mean-squared vibrational amplitudes can be calculated. These calculations will also be useful in the interpretation of experimental core-level photoemission spectra, which are influenced by inter-facial vibrational dynamics [9].

1.1. Overview of Thesis

This thesis will examine W and Mo substrates, with a layer of alkali metals adsorbed on the surfaces. To probe the importance of the density of substrate atoms three surfaces will be examined. In order of least to most dense the surfaces are (111), (100) and the (110). To examine the importance of the adsorbate atom density the adsorbate atoms will be arranged in increasingly higher coverages. Here coverage refers to the ratio of the number of atoms in the adsorbate layer to the number of atoms in the first substrate layer.

On the (110) surface of W and Mo, we study an adsorbed layer of lithium (Li) in coverages of a sixth, quarter, third, and full monolayer. Each of these structures have been observed experimentally [10, 11]. Since higher coverages involve packing absorbate atoms more densely, looking at multiple coverages give insight into the inter-adsorbate atom effects.

For the (100) surface of W, adsorbed layers of K at a half and quarter monolayer will be studied. Each of these systems has been observed experimentally [12–14].

Finally, for the (111) surface of W, Li, Na, K and Cs will be examined using a full monolayer, once again because each has been experimentally observed [15].

The analysis will include generating dispersion curves, calculating (i) layer resolved densities of states, (ii) near-surface atomic layer relaxation values, and (iii) layer resolved Debye temperatures. These results are sufficient to describe the vibrational thermal properties of these systems.

The remaining chapters of the thesis will cover the material necessary to understand the research that has been done. Chapter 2 will discuss in detail the inner workings of Alkali Lattice Explorer (ALE), the program used to perform the calculations. This section is intended as a "how to" guide for future students who will continue work on the project. It will explain the key features and design paradigms of the program, as well as explaining how the program is run. This chapter will conclude with instructions on making changes to ALE's code base. Chapter 3 will focus on work that has been done to build EAM models for the alkalis, tungsten, and molybdenum. This chapter will include comparisons of different models for all the studied materials with experimental data, as well as comparisons to other high-quality EAM and density

functional theory calculations. Chapter 4 will focus on building an appropriate heterogeneous pair-potential model. Finally, Chapter 5 will show the results from the models constructed in Chapter 4. These results will include dispersion curves, densities of states, and near-surface atomic-layer relaxation values.

1.2. Theory

1.2.1. The EAM Model

The EAM model is a semiempirical approach to modeling the potential energy of a crystal. It treats the energy as coming from two sources. The main contribution comes from pair-wise interactions of atoms in the lattice through some potential function $\phi(r)$. The second piece of the EAM model is known as the embedding energy, usually written as $F(\rho)$. The idea is that each atom in the lattice is embedded in some charge density ρ, and the interaction of the atom with charge that it sees contributes to the potential energy of the crystal.

Up until the early 1980's, models using only pair potentials were widely used [16]. However, certain important features of a metal are incorrectly described by purely pair potential models. For example, a pair potential model predicts that the Cauchy pressure – a quantity related to linear elastic constants of a material – is zero [17]. It is experimentally well known that the Cauchy pressure is nonzero. This failure of a pair potential model is often referred to as the Cauchy discrepancy [18].

The EAM approach to resolving the Cauchy discrepancy is to introduce the embedding term $F(\rho)$ to the potential energy. This term accounts for the many-body interactions in a crystal lattice through the charge density $\rho(\mathbf{r}_{n\alpha})$. The charge density should be thought of as a function of position, and arises due to individual charge density contributions from each atom in the lattice, usually written as $f(r)$.

Thus we arrive at the complete EAM model, where the energy of a crystal is written as

$$E = \frac{1}{2}\sum_{n\alpha}\sum_{m\beta}\phi_{\alpha}^{\beta}(r_{n\alpha}^{m\beta}) + \sum_{n\alpha}F_{\alpha}\left(\rho\left(\mathbf{r}_{n\alpha}\right)\right). \tag{1.1}$$

Throughout this thesis, n and m will label unit cells. The letters α and β are used to label

atoms in a unit cell. Thus, $\mathbf{r}_{n\alpha}$ is the location of atom α in unit cell n. To label vectors between atoms, the shorthand

$$\mathbf{r}_{n\alpha}^{m\beta} \equiv \mathbf{r}_{m\beta} - \mathbf{r}_{n\alpha} \tag{1.2}$$

is used. The sums in (1.1) are therefore sums over each unit cell and each atom in a unit cell in the crystal. These are sometimes referred to as lattice sums.

The labels α and β on ϕ_α^β and F_α refer to the models for atoms α and β. For example, the pair potential interaction between two lithium atoms looks different than the pair potential between a lithium atom and a tungsten atom. Thus, it is necessary to have a model for both ϕ_{Li}^{W} and ϕ_{Li}^{Li}.

As noted earlier, the charge density $\rho(\mathbf{r}_{n\alpha})$ comes from a lattice sum,

$$\rho(\mathbf{r}_{n\alpha}) = \sum_{m\beta} f_\beta(r_{n\alpha}^{m\beta}), \tag{1.3}$$

where

$$r_{n\alpha}^{m\beta} = |\mathbf{r}_{n\alpha}^{m\beta}|. \tag{1.4}$$

Thus, in order to specify a particular EAM model, it is sufficient to specify the functions $\phi(r)$, $F(\rho)$, and $f(r)$.

1.2.2. Dynamical Matrix

To understand the vibrational properties of metallic systems, we will be working under the harmonic approximation. This means that we will only be looking at dynamics in which the atoms in the lattice move very close to equilibrium. In this regime, the energy of the crystal can be expanded in a Taylor series with displacements from equilibrium labeled by $s_{n\alpha i}$, with the Cartesian direction indicated by i and j,

$$E \approx E_0 + \frac{1}{2}\frac{\partial^2 E}{\partial r_{n\alpha i}\partial r_{m\beta j}} s_{n\alpha i} s_{m\beta j}. \tag{1.5}$$

Here, $s_{n\alpha i}$ is the displacement from equilibrium of atom α in unit cell n in the i direction. This view of the crystal is very suggestive of a set of coupled harmonic oscillators. To that end, it is

useful to talk about force constants associated with the second derivatives of the energy, which we define as

$$K_{m\alpha i}^{n\beta j} \equiv \frac{\partial^2 E}{\partial r_{n\alpha i} \partial r_{m\beta j}}. \tag{1.6}$$

We take the following approach to work out the available normal modes of oscillation. Because each unit cell of the lattice is identical, analyzing the dynamics of a single unit cell is sufficient to understand the dynamics of the entire system. Consider then the equation of motion for the displacement from equilibrium in the i direction $\mathbf{s}_{n\alpha i}$ obtained by applying Newton's second law to atom α in unit cell n. Using (1.5) and (1.6), we have that

$$M_\alpha \ddot{s}_{n\alpha i} = -\sum_{m\beta j} K_{m\alpha i}^{n\beta j} s_{m\beta j}, \tag{1.7}$$

where M_α is the mass of atom α. Here we see the advantage of using (1.6). This equation of motion looks just like that of a mass attached to several springs.

We assume normal mode solutions that take the form of plane waves with wavevector $\mathbf{k}$ and frequency ω, so that

$$s_{n\alpha i} = \frac{1}{\sqrt{M_\alpha}} u_{\alpha i} e^{i(\mathbf{k}\cdot\mathbf{r}_n - \omega t)}. \tag{1.8}$$

Here, $u_{\alpha i}$ is the i component of the polarization of atom α. Note that $\mathbf{r}_n$ is a vector that points to a fixed location in unit cell n, not the atom α in that unit cell. As it turns out, this choice makes excellent use of the symmetry of the lattice. Inserting (1.8) into (1.7) and applying some simplifications, we get

$$\frac{1}{\sqrt{M_\alpha M_\beta}} \sum_m K_{m\alpha i}^{n\beta j} e^{i\mathbf{k}\cdot(\mathbf{r}_m - \mathbf{r}_n)} u_{\beta j} = \omega^2 u_{\alpha i}. \tag{1.9}$$

The left hand side of (1.9) contains an element of one of the most important objects to the computational approach we are taking, namely the dynamical matrix. We define it as

$$\mathbb{D}_{\alpha i}^{\beta j}(\mathbf{k}) \equiv \frac{1}{\sqrt{M_\alpha M_\beta}} \sum_m K_{m\alpha i}^{n\beta j}. \tag{1.10}$$

This allows us to write (1.9) as

$$\sum_{\beta j} \mathbb{D}_{\alpha i}^{\beta j}(\mathbf{k}) u_{\beta j} = \omega^2 u_{\alpha i}. \tag{1.11}$$

Equation (1.11) is crucial to our study of crystal dynamics. It allows us to find all of the normal modes associated with a wave vector $\mathbf{k}$. This is done by calculating the dynamical matrix and finding its eigenvalues ω^2 and eigenvectors $u_{\alpha i}$. We interpret each eigenvalue and eigenvector pair as describing a normal mode with frequency ω and polarization $u_{\alpha i}$. Thus, in order to computationally work out all possible normal modes, we could simply compute the dynamical matrix for all meaningful wave vectors. Luckily, the symmetry of the crystal sheds some light on what it means for a wave vector to be physically meaningful.

1.2.3. Wave Vectors

The normal modes $\mathbf{s}_{n\alpha}$ from (1.8) are characterized by a wave vector $\mathbf{k}$. It is the wave vector that determines the dynamical matrix, and thus the frequencies of a mode. Because the wave vectors are so important to the analysis, it is useful to describe the space in which they live.

We call the space of wave vectors reciprocal space. For any lattice characterized by the primitive vectors $\mathbf{a}_1$, $\mathbf{a}_2$, and $\mathbf{a}_3$, a reciprocal lattice can be constructed using the reciprocal lattice vectors $\mathbf{b}_1$, $\mathbf{b}_2$, and $\mathbf{b}_3$. These reciprocal lattice vectors are related to the primitive vectors by

$$\begin{aligned} \mathbf{b}_1 &= 2\pi \frac{\mathbf{a}_2 \times \mathbf{a}_3}{\mathbf{a}_1 \cdot \mathbf{a}_2 \times \mathbf{a}_3} \\ \mathbf{b}_2 &= 2\pi \frac{\mathbf{a}_3 \times \mathbf{a}_1}{\mathbf{a}_1 \cdot \mathbf{a}_2 \times \mathbf{a}_3} \\ \mathbf{b}_3 &= 2\pi \frac{\mathbf{a}_1 \times \mathbf{a}_2}{\mathbf{a}_1 \cdot \mathbf{a}_2 \times \mathbf{a}_3}. \end{aligned} \tag{1.12}$$

Due to the discrete translational symmetry of the lattice, a normal mode with wave vector $\mathbf{k}$ is identical to a mode whose wave vector has been shifted from $\mathbf{k}$ by an integer multiple of a reciprocal lattice vector.

This translational symmetry of the wave vectors means that all normal modes of a crystal

can be characterized by wave vectors which lie in a single unit cell of the reciprocal lattice. Generally, a region known as the first Brillouin zone is used. This zone is a Wigner-Seitz cell in reciprocal space, and can be constructed from the reciprocal lattice vectors. Thus, every crystal lattice will have an associated first Brillouin zone. For example, a body centered cubic (BCC) lattice has the first Brillouin shown in Figure 1.1.

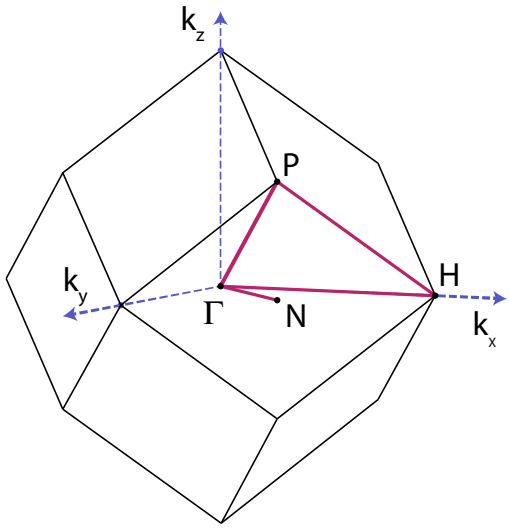

Figure 1.1. The first Brillouin zone of the BCC structure. The high symmetry directions run from Γ- H, H-P-Γ, and Γ-N.

The first Brillouin zone has additional symmetry that can simplify vibrational calculations. The region indicated in red within the zone in Figure 1.1 is known as the irreducible part of the Brillouin zone (IBZ). The IBZ is the smallest portion of the first Brillouin zone that can, through rotations and inversions, recreate the entire first Brillouin zone. The significance of the IBZ is that the frequencies of a mode whose wave vector lies outside the IBZ are identical to a mode whose wave vector is within the IBZ. Thus, in order to characterize all possible frequencies of a crystal, it is sufficient to probe only wave vectors which lie in the IBZ.

There are three more three dimensional lattices that are of interest. These are the face centered cubic (FCC) lattice, the hexagonal close packed (HCP) lattice, and the 9R lattice. The

corresponding first Brillouin zones are shown in Figure 1.2, Figure 1.3, and Figure 1.4.

Most of the analysis in this study will be on the two dimensional lattices used to describe crystal surfaces. We will be focusing on the (100), (110), and (111) surfaces of the BCC structure. Figures 1.5, 1.6, and 1.7 show the first Brillouin zones and IBZs of these surfaces.

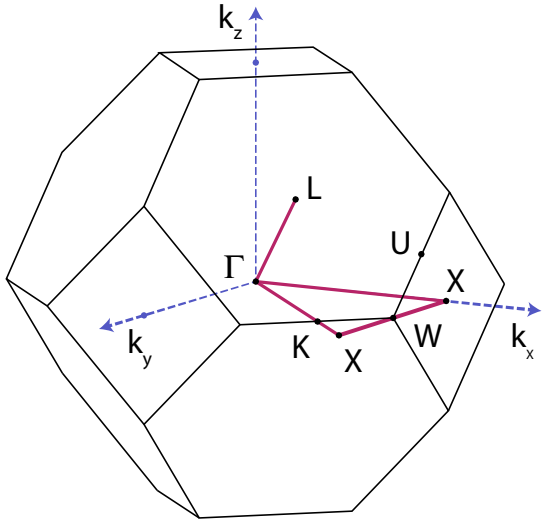

Figure 1.2. The first Brillouin zone of the FCC structure. The high symmetry directions run from Γ- X, X-W-X, X-Γ and Γ-L.

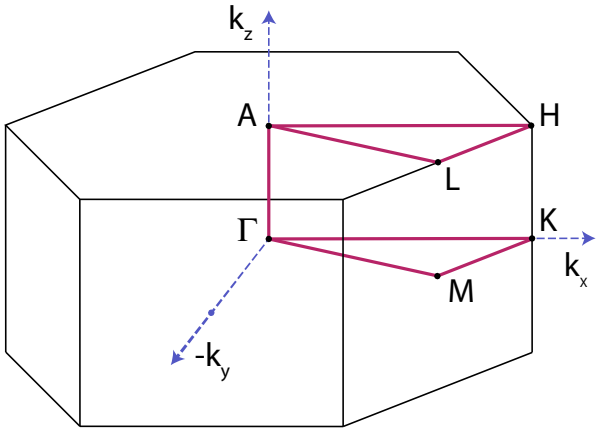

Figure 1.3. The first Brillouin zone of the HCP structure. The high symmetry directions run from Γ- K, K-M, M-Γ, Γ-A, A-H, H-L, and L-A.

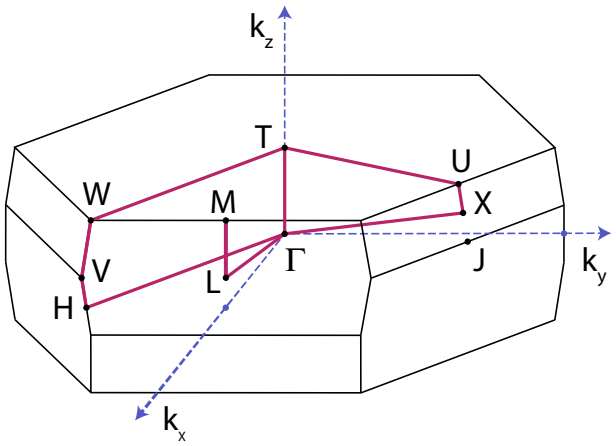

Figure 1.4. The first Brillouin zone of the 9R structure. The high symmetry directions run from M-L, L-Γ, Γ-T, T-U, U-X, X-Γ, Γ-H, H-V, V-W, and W-T.

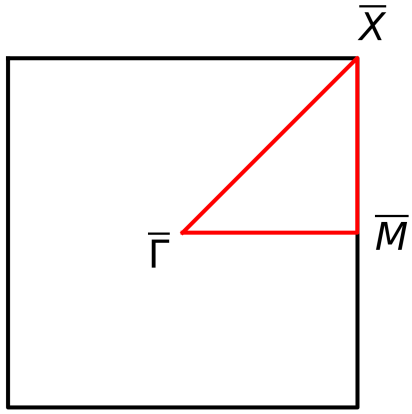

Figure 1.5. The first Brillouin zone of the 100 surface of the BCC structure. The high symmetry directions run from $\overline{\Gamma}$- $\overline{X}$, $\overline{X}$-$\overline{M}$, and $\overline{M}$-$\overline{\Gamma}$.

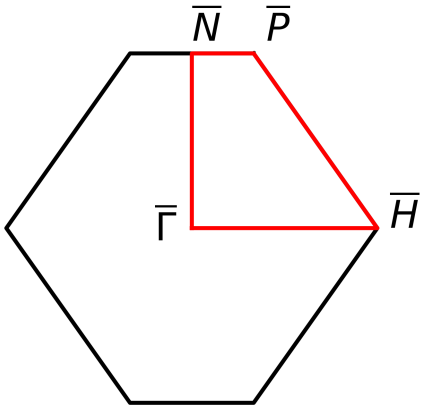

Figure 1.6. The first Brillouin zone of the 110 surface of the BCC structure. The high symmetry directions run from $\overline{\Gamma}$- $\overline{N}$, $\overline{N}$-$\overline{P}$, $\overline{P}$-$\overline{H}$, and $\overline{H}$-$\overline{\Gamma}$.

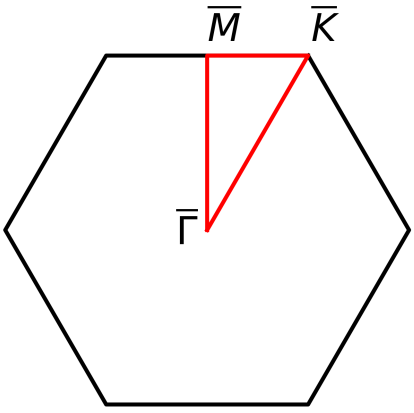

Figure 1.7. The first Brillouin zone of the 111 surface of the BCC structure. The high symmetry directions run from $\overline{\Gamma}$- $\overline{M}$, $\overline{M}$-$\overline{K}$, and $\overline{K}$-$\overline{\Gamma}$.

1.2.4. Force Constants

In order to calculate the dynamical matrix it is necessary to calculate the force constants $K_{m\alpha i}^{m\beta j}$. Because the EAM model of the potential energy of a crystal is a somewhat complicated function of position, taking two derivatives to find the force constants is somewhat nontrivial. Fortunately, Riffe *et al.* [19] have worked out the details. The results will be quoted here.

A few labeling conventions will be used to make the equations less bulky. The symbol $\hat{\mathbf{r}}_{n\alpha}^{m\beta}$ is a unit vector, so that $\hat{\mathbf{r}}_{n\alpha}^{m\beta} = \mathbf{r}_{n\alpha}^{m\beta}/r_{n\alpha}^{m\beta}$. Functions have been shortened so that

$$\phi_{n\alpha}^{m\beta} = \phi_{\alpha}^{\beta}(r_{n\alpha}^{m\beta}), \tag{1.13}$$

$$F_{n\alpha} = F_{\alpha}(\rho(\mathbf{r}_{n\alpha})), \tag{1.14}$$

and

$$f_{n\alpha}^{m\beta} = f_{\alpha}(r_{n\alpha}^{m\beta}). \tag{1.15}$$

It is useful to split the force constants into contributions from the pair potential ${}^{p}K_{m\alpha i}^{m\beta j}$ and contributions from the embedding energy ${}^{e}K_{m\alpha i}^{m\beta j}$. The pair potential piece is given by

$$\begin{aligned} {}^{p}K_{m\alpha i}^{m\beta j} = \sum_{m'\beta'} & \left[\frac{D\phi_{m'\beta'}^{m\beta}}{r_{m'\beta'}^{m\beta}} \left(\delta_{ij} - \hat{\mathbf{r}}_{m'\beta' i}^{m\beta} \hat{\mathbf{r}}_{m'\beta' j}^{m\beta} \right) + D^2\phi_{m'\beta'}^{m\beta} \hat{\mathbf{r}}_{m'\beta' i}^{m\beta} \hat{\mathbf{r}}_{m'\beta' j}^{m\beta} \right] \delta_{nm}\delta_{\alpha\beta} \\ & - \left[\frac{D\phi_{n\alpha}^{m\beta}}{r_{n\alpha}^{m\beta}} \left(\delta_{ij} - \hat{\mathbf{r}}_{n\alpha i}^{m\beta} \hat{\mathbf{r}}_{n\alpha j}^{m\beta} \right) + D^2\phi_{n\alpha}^{m\beta} \hat{\mathbf{r}}_{n\alpha i}^{m\beta} \hat{\mathbf{r}}_{n\alpha j}^{m\beta} \right] (1 - \delta_{nm}\delta_{\alpha\beta}) \,. \end{aligned} \tag{1.16}$$

Here we use a somewhat more compact notation for derivatives of a function with a single variable. For any function $f(x)$,

$$Df \equiv \frac{\mathrm{d}}{dx} f(x) \tag{1.17}$$

and

$$D^2 f \equiv \frac{\mathrm{d}^2}{dx^2} f(x). \tag{1.18}$$

We split the contribution from the embedding piece into three sections.

$${}^{e}K_{m\alpha i}^{m\beta j} = {}^{e1}K_{m\alpha i}^{m\beta j} + {}^{e2}K_{m\alpha i}^{m\beta j} + {}^{e3}K_{m\alpha i}^{m\beta j}, \tag{1.19}$$

where

$$
\begin{aligned}
{}^{e1}K^{m\beta j}_{m\alpha i} = &\sum_{m'\beta'} \left(DF_{m\beta} Df^{m\beta}_{m'\beta'} + DF_{m'\beta'} Df^{m'\beta'}_{m\beta} \right) \frac{\delta_{ij} - \hat{\mathbf{r}}^{m\beta}_{m'\beta' i} \hat{\mathbf{r}}^{m\beta}_{m'\beta' j}}{r^{m\beta}_{m'\beta'}} \delta_{nm}\delta_{\alpha\beta} \\
&- \left(DF_{m\beta} Df^{m\beta}_{n\alpha} + DF_{n\alpha} Df^{n\alpha}_{m\beta} \right) \frac{\delta_{ij} - \hat{\mathbf{r}}^{m\beta}_{n\alpha i} \hat{\mathbf{r}}^{m\beta}_{n\alpha j}}{r^{m\beta}_{n\alpha}} \left(1 - \delta_{nm}\delta_{\alpha\beta}\right),
\end{aligned}
\tag{1.20}
$$

$$
\begin{aligned}
{}^{e2}K^{m\beta j}_{m\alpha i} = &\sum_{m'\beta'} \left(DF_{m\beta} D^2 f^{m\beta}_{m'\beta'} + DF_{m'\beta'} D^2 f^{m'\beta'}_{m\beta} \right) \hat{\mathbf{r}}^{m\beta}_{m'\beta' i} \hat{\mathbf{r}}^{m\beta}_{m'\beta' j} \delta_{nm}\delta_{\alpha\beta} \\
&- \left(DF_{m\beta} D^2 f^{m\beta}_{n\alpha} + DF_{n\alpha} D^2 f^{n\alpha}_{m\beta} \right) \hat{\mathbf{r}}^{m\beta}_{n\alpha i} \hat{\mathbf{r}}^{m\beta}_{n\alpha j} \left(1 - \delta_{nm}\delta_{\alpha\beta}\right),
\end{aligned}
\tag{1.21}
$$

and

$$
\begin{aligned}
{}^{e3}K^{m\beta j}_{m\alpha i} = &\sum_{m'\beta'} \sum_{m''\beta''} D^2 F_{m\beta} Df^{m\beta}_{m''\beta''} Df^{m\beta}_{m'\beta'} \hat{\mathbf{r}}^{m\beta}_{m''\beta'' i} \hat{\mathbf{r}}^{m\beta}_{m'\beta' j} \delta_{nm}\delta_{\alpha\beta} \\
&- \sum_{m'\beta'} D^2 F_{m\beta} Df^{m\beta}_{n\alpha} Df^{m\beta}_{m'\beta'} \hat{\mathbf{r}}^{m\beta}_{n\alpha i} \hat{\mathbf{r}}^{m\beta}_{m'\beta' j} \left(1 - \delta_{nm}\delta_{\alpha\beta}\right) \\
&- \sum_{m'\beta'} D^2 F_{n\alpha} Df^{n\alpha}_{m'\beta'} Df^{n\alpha}_{m\beta} \hat{\mathbf{r}}^{n\alpha}_{m'\beta' i} \hat{\mathbf{r}}^{n\alpha}_{m\beta j} \left(1 - \delta_{nm}\delta_{\alpha\beta}\right) \\
&+ \sum_{m'\beta'} D^2 F_{m'\beta'} Df^{m'\beta'}_{n\alpha} Df^{m'\beta'}_{m\beta} \hat{\mathbf{r}}^{m'\beta'}_{n\alpha i} \hat{\mathbf{r}}^{m'\beta'}_{m\beta j}.
\end{aligned}
\tag{1.22}
$$

Because the force constants are being identified as the coefficients of a Taylor expansion, equations (1.16), (1.20), (1.21), and (1.22) are all evaluated at the equilibrium position of the lattice.

This fact leads to an interesting note about (1.20) and (1.21). Both of these expressions have an overall factor of the first derivative of the embedding energy $DF_{n\alpha}$. Therefore, if the model for the embedding energy has a derivative of zero at equilibrium, then (1.20) and (1.21) are also zero, making computation much simpler. Models which have this property are called normalized.

As it turns out, if a model is not normalized, a transformation may be performed to normalize it. The pair potential is transformed as

$$
\psi^{m\beta}_{n\alpha} = \phi^{m\beta}_{n\alpha} + DF_{m\beta} f^{m\beta}_{n\alpha} + DF_{n\alpha} f^{n\alpha}_{m\beta},
\tag{1.23}
$$

and the embedding energy transforms as

$$\bar{F}_{n\alpha} = F_{n\alpha} - DF_{n\alpha}\,\rho(\mathbf{r}_{n\alpha}). \tag{1.24}$$

With this transformed potential, it is clear that $D\bar{F}_{n\alpha} = 0$. It is also interesting to note that (1.23) now contains all pair like interactions. It is therefore possible to redefine the force constants so that

$$K^{m\beta j}_{m\alpha i} =^{ep} K^{m\beta j}_{m\alpha i} +^{e3} K^{m\beta j}_{m\alpha i}, \tag{1.25}$$

where

$$\begin{aligned} {}^{ep}K^{m\beta j}_{m\alpha i} = \sum_{m'\beta'} &\left[\frac{D\psi^{m\beta}_{m'\beta'}}{r^{m\beta}_{m'\beta'}}\left(\delta_{ij} - \hat{\mathbf{r}}^{m\beta}_{m'\beta' i}\hat{\mathbf{r}}^{m\beta}_{m'\beta' j}\right) + D^2\psi^{m\beta}_{m'\beta'}\hat{\mathbf{r}}^{m\beta}_{m'\beta' i}\hat{\mathbf{r}}^{m\beta}_{m'\beta' j}\right]\delta_{nm}\delta_{\alpha\beta} \\ &- \left[\frac{D\psi^{m\beta}_{n\alpha}}{r^{m\beta}_{n\alpha}}\left(\delta_{ij} - \hat{\mathbf{r}}^{m\beta}_{n\alpha i}\hat{\mathbf{r}}^{m\beta}_{n\alpha j}\right) + D^2\psi^{m\beta}_{n\alpha}\hat{\mathbf{r}}^{m\beta}_{n\alpha i}\hat{\mathbf{r}}^{m\beta}_{n\alpha j}\right](1 - \delta_{nm}\delta_{\alpha\beta})\,. \end{aligned} \tag{1.26}$$

For this reason, $\psi^{m\beta}_{n\alpha}$ is often referred to as the effective potential.

1.2.5. Born-von-Kármán Force Constants

A small note should be made about Born-von-Kármán (BvK) force constants. Due to lattice symmetry, there are only a handful of parameters which are needed to describe the force constants from an atom in a particular shell. The precise number of unique parameters depends on the lattice. For the BCC lattice, Riffe *et al.* have worked out the number of unique parameters for the first five shells [19].

These parameters can be directly fit to experimental phonon frequencies. The dispersion curves obtained from these BvK force constants can be thought of as the best possible fits that any model could obtain. Although this seems to suggest that the BvK approach is superior to modeling the potential energy of a lattice, there are disqualifying drawbacks to only using BvK force constants. Namely, since the BvK approach has no underlying potential energy, it is impossible to use the BvK force constants to model the more complex bimetallic systems that are the eventual goal of this study.

In chapter 3, we will compare our model results in bulk W and Mo to results obtained directly from BvK force constants. Doing so will give an idea of how well our model is performing in the bulk.

CHAPTER 2
METHODS OF USE

2.1. ALE

Alkali Lattice Explorer (ALE) is a program which began development in December of 2017. Its original purpose was to recreate the computational capabilities of a Matlab program developed by Richard Wilson, but with vastly improved performance and generality of use. It has since expanded into a large code-base comprising Fortran and Python code, and it can perform important calculations for bulk materials, clean surfaces, and surfaces with adsorbed layers of atoms.

ALE makes very few assumptions about the types of materials and structures analyzed. This gives it the advantage of being able to deal with many different types of systems. ALE can be easily adjusted to handle any type of unit cell or set of basis vectors, and allows the user to specify what EAM model to use. This allows for easy comparison of different models of a material, and allows one to arrange that material in any lattice imaginable. Although ALE has primarily been used to study alkali metals, there is no restriction to the type of material it examines, as long as it is supplied with the appropriate model.

2.2. How ALE Works

2.2.1. Atomic Interaction Data Type

ALE centers around the derived data type called `interaction`. The general idea is that this type holds all pertinent information about the interaction between two atoms.

In practice, we need to know the information about atoms in a single unit cell, which we assume has an atom located at the origin. ALE keeps a three dimensional list of interactions called `atomic_interactions`(α, β, m). The list is indexed as follows. The index α refers to which atom in the unit cell at the origin we are considering, m is the index of the unit cell which

holds the atom with which atom α is interacting, and β refers to the atom within unit cell m with which atom α is interacting.

Each element of this list contains the following information.

- The three-component vector between atom α in the unit cell at the origin and atom β in the m unit cell, expressed in cartesian coordinates, called `vecToAtom`.
- The distance between the two atoms, called `norm`.
- A 3×3 array called `force_constants(i,j)`, which describes the components of force on atom α when atom β is displaced in different directions. This array is indexed so that `force_constants(1,2)` is the x component of force on atom α when atom β is displaced in the y direction, with x, y, and z being indexed as 1, 2, and 3, respectively.

This paradigm allows for straight forward iteration over atoms in the lattice, which is used throughout the code. Importantly, since the force constants are computationally expensive to calculate, ALE will only calculate them once, when the program is first started. Those force constants are then stored in a seperate file called `force_constants.txt`, so that if the same material is being analyzed multiple times, there is no need to recalculate the force constants, unless there has been a change to the lattice vectors or potential functions.

Keeping a list of precalculated force constants is essential to ALE's performance. This is due to the complexity of the embedding piece of the force constants. Since each embedding force constant requires a sum over all atoms in the lattice, and each element of the dynamical matrix requires a sum over all atoms in the lattice, the complexity of calculating the dynamical matrix would be $O(n^2)$, where n is the number of atoms in the lattice. This would lead to prohibitively large run-times.

Though simplifications to the expression for ${}^{e}K_{n\alpha i}^{m\beta j}$ exist for certain structures, such as BCC and FCC lattices with inversion symmetry [19], the slab calculations must use the full equation from (1.22). Thus, by precalculating ${}^{e}K_{n\alpha i}^{m\beta j}$, we are able to reduce the complexity of the dynamical matrix calculation to $O(n)$. This is far more managable for modern computer hardware, and allows for a more efficient workflow.

2.2.2. The Dynamical Matrix

With a list of force constants stored in memory, it becomes straight forward to calculate the dynamical matrix. ALE simply creates a $3N \times 3N$ matrix, where N is the number of atoms per unit cell. The only trick is in indexing the elements of the matrix. Ideally, we'd like to directly apply (1.11). However, this equation uses four indices (α, i, β, and j) for each element of the matrix, when only two are required.

This set of labels makes it clear which atoms and Cartesian directions each element references; e.g. if we look at $\mathbb{D}^{3,y}_{1,x}$, we are looking at the effect on the x component of the motion of the first atom in the basis when the third atom in the basis is displaced in the y direction. However, to code this, we need to index each element by using only two integers, which refer to the element's location in the matrix.

To solve this probelm, it is helpful to see where a particular choice of α, β, i and j put us in the matrix. Consider a lattice with three atoms per unit cell. Then the dynamical matrix is 9×9. If we let $\alpha = 1$ and $\beta = 3$, then we are referring to the highlighted 3×3 submatrix shown below.

$$\mathbb{D}^{\beta j}_{\alpha i} = \begin{pmatrix} \mathbb{D}^{1,x}_{1,x} & \mathbb{D}^{1,y}_{1,x} & \mathbb{D}^{1,z}_{1,x} & \mathbb{D}^{2,x}_{1,x} & \mathbb{D}^{2,y}_{1,x} & \mathbb{D}^{2,z}_{1,x} & \mathbb{D}^{3,x}_{1,x} & \mathbb{D}^{3,y}_{1,x} & \mathbb{D}^{3,z}_{1,x} \\ \mathbb{D}^{1,x}_{1,y} & \mathbb{D}^{1,y}_{1,y} & \mathbb{D}^{1,z}_{1,y} & \mathbb{D}^{2,x}_{1,y} & \mathbb{D}^{2,y}_{1,y} & \mathbb{D}^{2,z}_{1,y} & \mathbb{D}^{3,x}_{1,y} & \mathbb{D}^{3,y}_{1,y} & \mathbb{D}^{3,z}_{1,y} \\ \mathbb{D}^{1,x}_{1,z} & \mathbb{D}^{1,y}_{1,z} & \mathbb{D}^{1,z}_{1,z} & \mathbb{D}^{2,x}_{1,z} & \mathbb{D}^{2,y}_{1,z} & \mathbb{D}^{2,z}_{1,z} & \mathbb{D}^{3,x}_{1,z} & \mathbb{D}^{3,y}_{1,z} & \mathbb{D}^{3,z}_{1,z} \\ \mathbb{D}^{1,x}_{2,x} & \mathbb{D}^{1,y}_{2,x} & \mathbb{D}^{1,z}_{2,x} & \mathbb{D}^{2,x}_{2,x} & \mathbb{D}^{2,y}_{2,x} & \mathbb{D}^{2,z}_{2,x} & \mathbb{D}^{3,x}_{2,x} & \mathbb{D}^{3,y}_{2,x} & \mathbb{D}^{3,z}_{2,x} \\ \mathbb{D}^{1,x}_{2,y} & \mathbb{D}^{1,y}_{2,y} & \mathbb{D}^{1,z}_{2,y} & \mathbb{D}^{2,x}_{2,y} & \mathbb{D}^{2,y}_{2,y} & \mathbb{D}^{2,z}_{2,y} & \mathbb{D}^{3,x}_{2,y} & \mathbb{D}^{3,y}_{2,y} & \mathbb{D}^{3,z}_{2,y} \\ \mathbb{D}^{1,x}_{2,z} & \mathbb{D}^{1,y}_{2,z} & \mathbb{D}^{1,z}_{2,z} & \mathbb{D}^{2,x}_{2,z} & \mathbb{D}^{2,y}_{2,z} & \mathbb{D}^{2,z}_{2,z} & \mathbb{D}^{3,x}_{2,z} & \mathbb{D}^{3,y}_{2,z} & \mathbb{D}^{3,z}_{2,z} \\ \mathbb{D}^{1,x}_{3,x} & \mathbb{D}^{1,y}_{3,x} & \mathbb{D}^{1,z}_{3,x} & \mathbb{D}^{2,x}_{3,x} & \mathbb{D}^{2,y}_{3,x} & \mathbb{D}^{2,z}_{3,x} & \mathbb{D}^{3,x}_{3,x} & \mathbb{D}^{3,y}_{3,x} & \mathbb{D}^{3,z}_{3,x} \\ \mathbb{D}^{1,x}_{3,y} & \mathbb{D}^{1,y}_{3,y} & \mathbb{D}^{1,z}_{3,y} & \mathbb{D}^{2,x}_{3,y} & \mathbb{D}^{2,y}_{3,y} & \mathbb{D}^{2,z}_{3,y} & \mathbb{D}^{3,x}_{3,y} & \mathbb{D}^{3,y}_{3,y} & \mathbb{D}^{3,z}_{3,y} \\ \mathbb{D}^{1,x}_{3,z} & \mathbb{D}^{1,y}_{3,z} & \mathbb{D}^{1,z}_{3,z} & \mathbb{D}^{2,x}_{3,z} & \mathbb{D}^{2,y}_{3,z} & \mathbb{D}^{2,z}_{3,z} & \mathbb{D}^{3,x}_{3,z} & \mathbb{D}^{3,y}_{3,z} & \mathbb{D}^{3,z}_{3,z} \end{pmatrix} \tag{2.1}$$

This submatrix tells us about all of the effects that atom 1 in the basis has on atom 3 in the basis. The indicies i and j pick out a particular element of this submatrix. For example, if $i = 1$ and $j = 2$, we would be looking at the x component of force exerted on atom 1 when atom 3

is displaced in the y direction. This would pick out the highlighted element shown below.

$$\mathbb{D}_{\alpha i}^{\beta j} = \begin{pmatrix} \mathbb{D}_{1,x}^{1,x} & \mathbb{D}_{1,x}^{1,y} & \mathbb{D}_{1,x}^{1,z} & \mathbb{D}_{1,x}^{2,x} & \mathbb{D}_{1,x}^{2,y} & \mathbb{D}_{1,x}^{2,z} & \mathbb{D}_{1,x}^{3,x} & \mathbb{D}_{1,x}^{3,y} & \mathbb{D}_{1,x}^{3,z} \\ \mathbb{D}_{1,y}^{1,x} & \mathbb{D}_{1,y}^{1,y} & \mathbb{D}_{1,y}^{1,z} & \mathbb{D}_{1,y}^{2,x} & \mathbb{D}_{1,y}^{2,y} & \mathbb{D}_{1,y}^{2,z} & \mathbb{D}_{1,y}^{3,x} & \mathbb{D}_{1,y}^{3,y} & \mathbb{D}_{1,y}^{3,z} \\ \mathbb{D}_{1,z}^{1,x} & \mathbb{D}_{1,z}^{1,y} & \mathbb{D}_{1,z}^{1,z} & \mathbb{D}_{1,z}^{2,x} & \mathbb{D}_{1,z}^{2,y} & \mathbb{D}_{1,z}^{2,z} & \mathbb{D}_{1,z}^{3,x} & \mathbb{D}_{1,z}^{3,y} & \mathbb{D}_{1,z}^{3,z} \\ \mathbb{D}_{2,x}^{1,x} & \mathbb{D}_{2,x}^{1,y} & \mathbb{D}_{2,x}^{1,z} & \mathbb{D}_{2,x}^{2,x} & \mathbb{D}_{2,x}^{2,y} & \mathbb{D}_{2,x}^{2,z} & \mathbb{D}_{2,x}^{3,x} & \mathbb{D}_{2,x}^{3,y} & \mathbb{D}_{2,x}^{3,z} \\ \mathbb{D}_{2,y}^{1,x} & \mathbb{D}_{2,y}^{1,y} & \mathbb{D}_{2,y}^{1,z} & \mathbb{D}_{2,y}^{2,x} & \mathbb{D}_{2,y}^{2,y} & \mathbb{D}_{2,y}^{2,z} & \mathbb{D}_{2,y}^{3,x} & \mathbb{D}_{2,y}^{3,y} & \mathbb{D}_{2,y}^{3,z} \\ \mathbb{D}_{2,z}^{1,x} & \mathbb{D}_{2,z}^{1,y} & \mathbb{D}_{2,z}^{1,z} & \mathbb{D}_{2,z}^{2,x} & \mathbb{D}_{2,z}^{2,y} & \mathbb{D}_{2,z}^{2,z} & \mathbb{D}_{2,z}^{3,x} & \mathbb{D}_{2,z}^{3,y} & \mathbb{D}_{2,z}^{3,z} \\ \mathbb{D}_{3,x}^{1,x} & \mathbb{D}_{3,x}^{1,y} & \mathbb{D}_{3,x}^{1,z} & \mathbb{D}_{3,x}^{2,x} & \mathbb{D}_{3,x}^{2,y} & \mathbb{D}_{3,x}^{2,z} & \mathbb{D}_{3,x}^{3,x} & \mathbb{D}_{3,x}^{3,y} & \mathbb{D}_{3,x}^{3,z} \\ \mathbb{D}_{3,y}^{1,x} & \mathbb{D}_{3,y}^{1,y} & \mathbb{D}_{3,y}^{1,z} & \mathbb{D}_{3,y}^{2,x} & \mathbb{D}_{3,y}^{2,y} & \mathbb{D}_{3,y}^{2,z} & \mathbb{D}_{3,y}^{3,x} & \mathbb{D}_{3,y}^{3,y} & \mathbb{D}_{3,y}^{3,z} \\ \mathbb{D}_{3,z}^{1,x} & \mathbb{D}_{3,z}^{1,y} & \mathbb{D}_{3,z}^{1,z} & \mathbb{D}_{3,z}^{2,x} & \mathbb{D}_{3,z}^{2,y} & \mathbb{D}_{3,z}^{2,z} & \mathbb{D}_{3,z}^{3,x} & \mathbb{D}_{3,z}^{3,y} & \mathbb{D}_{3,z}^{3,z} \end{pmatrix} \tag{2.2}$$

With this picture, one can see that the proper functions to translate between indexing the matrix using $\mathbb{D}_{\alpha i}^{\beta j}$ and using $\mathbb{D}_{k,l}$ are

$$k(\alpha, i) = i + 3(\alpha - 1) \tag{2.3}$$

and

$$l(\beta, j) = j + 3(\beta - 1). \tag{2.4}$$

Once the dynamical matrix has been calculated, ALE finds the eigenvalues and eigenvectors, and converts the eigenvalues to frequencies, using (1.11). The algorithm used to calculate the eigenvalues comes from the LAPACK library of linear algebra functions [20]. Specifically, the `zheev` subroutine is used. This routine is optimized to find the eigenvalues and eigenvectors of a hermitian complex-valued matrix.

Because the `zheev` routine has a somewhat complicated set of arguments to call, ALE uses a custom function called `eig(A,n)` which hard-codes all the required arguments for `zheev`. This custom function takes an $n \times n$ complex Hermitian matrix A, and returns an n-dimensional array containing the eigenvalues of A, sorted in ascending order.

2.2.3. Calculating Dispersion Curves

Dispersion curves show the relationship between wave vector and the associated frequencies. Using the dynamical matrix, ALE can calculate the frequencies associated with any wave vector. Typically, it is useful to examine how frequencies change as the wave vector increases along high symmetry directions. This is because experimentally observed vibrational frequencies are typically associated with wave vectors in the high symmetry directions, thus allowing the user to compare predicted frequency values with experimental values.

The high symmetry directions are dependent on the structure of the crystal. If we are examining surface vibrations, then the high symmetry directions will also depend on which surface is being examined. Typically, the high symmetry directions trace out the border of the IBZ, although sometimes additional directions are considered high symmetry.

In order to create dispersion data, ALE uses a subroutine called

`generate_dispersion_curve(slab,start_point,end_point,direction).`

This subroutine calculates frequencies in the direction of the wave vector pointing from

`start_point`

to

`end_point.`

1,000 points along this line are sampled. Once the calculation is complete, ALE stores the data in a file labeled by the

`direction`

argument in the directory of whatever material is being analyzed.

For surface dispersion curves, it is useful to look at the localization of modes in particular layers and directions. ALE accomplishes this by creating an additional data file for each layer and localization the user wishes to examine. These files contain the magnitude squared of the projection of the frequency's eigenvector onto the layer and direction on interest. For example, if ALE were calculating the projection of a mode with frequency ω and associated eigenvector

$\mathbf{v}$ onto the first layer shear vertical direction, then the quantity α stored in the data file for whatever wave vector was being analyzed would be

$$\alpha = \left(|\mathbf{v} \cdot \mathbf{u_1}|^2 + |\mathbf{v} \cdot \mathbf{u_2}|^2\right), \tag{2.5}$$

where

$$\mathbf{u_1} = \begin{pmatrix} 0 \\ 0 \\ 1 \\ 0 \\ \vdots \end{pmatrix}$$

and

$$\mathbf{u_2} = \begin{pmatrix} \vdots \\ 0 \\ 0 \\ 1 \end{pmatrix}$$

are the polarizations corresponding to being completely polarized in the shear vertical direction on the top and bottom layers of the slab, respectively.

Longitudinal and shear horizontal projections are obtained similarly. To calculate the projection of a mode onto the longitudinal (shear horizontal) direction in the first layer, the first three components of $\mathbf{u_1}$ are chosen to be a normalized three-component vector pointing parallel (perpendicular) to the wave vector $\mathbf{k}$. The same is done for the last three components of $\mathbf{u_2}$. Equation (2.5) is then used.

2.2.4. Plotting Dispersion Curves

Once the data have been created, ALE uses a collection of python scripts to create the actual plots. For bulk dispersion curves, the plotting routines are straightforward. A number of axes are created, corresponding to the number of high-symmetry directions that dispersion curves were calculated for. On these axes, the data are plotted. If the script is plotting dispersion curves for which experimental data are available, then these data points will be read in from

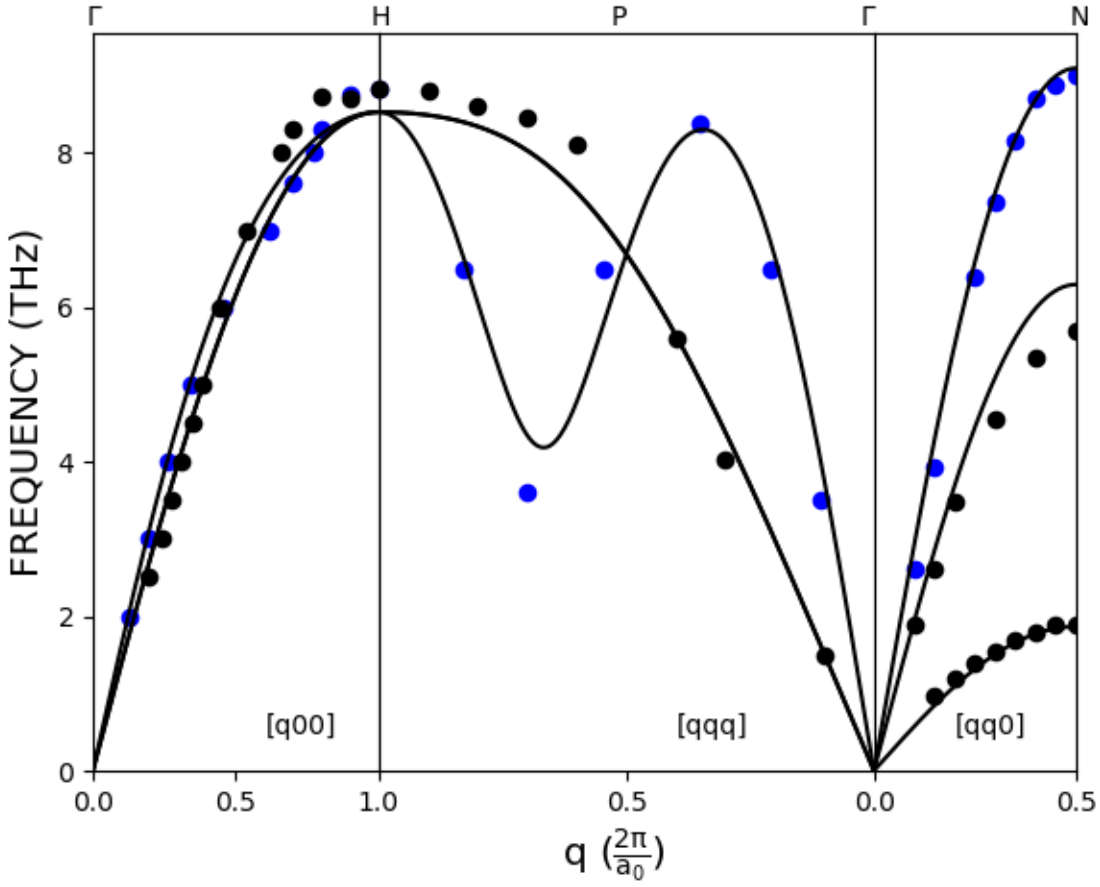

Figure 2.1. Li bulk dispersion curves. Blue (black) markers indicate experimental frequencies with longitudinal (transverse) polarizations [31].

a file and plotted as points at the appropriate wavevector For an example of a bulk dispersion curve plot, see Figure 2.1.

Plotting surface dispersion curves is much more complicated. In order to handle the large amount of data that needs to be plotted, ALE splits the procedure into two seperate scripts. The main script is called `plot_layer_dispersion.py`. This script creates a single dispersion curve image for a particular layer and polarization direction. The curves are color coded to reflect each mode's projection onto that layer and polarization direction (the α in (2.5)). Figure 2.2 shows the colors used.

The second script is called `plot_surf_dispersion.py`. This script acts as a wrapper for the plotting script. It simply calls

`plot_layer_dispersion.py`

with a variety of arguments to generate dispersion curve plots for the first 4 layers of a material, with polarizations localized in the shear vertical, shear horizontal, and longitudinal directions. Figure 2.3 shows an example of a set of dispersion curves for the (110) surface of Na.

Figure 2.2. Colorbar used for all surface dispersion curve plots. Colors indicate α for a mode.

2.2.5. Calculating the Density of States

ALE calculates the Density of States by sampling wave vectors within the IBZ of the structure being analyzed. Due to the symmetry of each structure, every point outside the IBZ has a mode equivalent to a point inside the IBZ. Therefore, in order to find all possible modes of vibration, it is sufficient to only look at points in the IBZ.

A helper program called Irreducible Point Affixer (IPA) is used to create a list of points in the irreducible Brillouin zone, as well as those points' effective weights. The effective weight of a point is a measure of how much of the volume of that point lies within the IBZ. For a concrete example, consider the IBZ shown in Figure 1.5. Any point on the interior of the zone has its entire volume in the zone. Since the IBZ is $\frac{1}{8}$ of the entire Brillouin zone, we will assign a weight of 8 to that point. Now consider applying rotations and reflections to the IBZ, such that all of space is filled with different IBZ shapes. In this picture, the point $\overline{\Gamma}$ is shared between 8 different zones. Thus only $\frac{1}{8}$ of that point is in the original IBZ. We would therefore assign $\overline{\Gamma}$ a weight that is $\frac{1}{8}$ the weight of a point in the interior, or a weight of 1. By this same process,

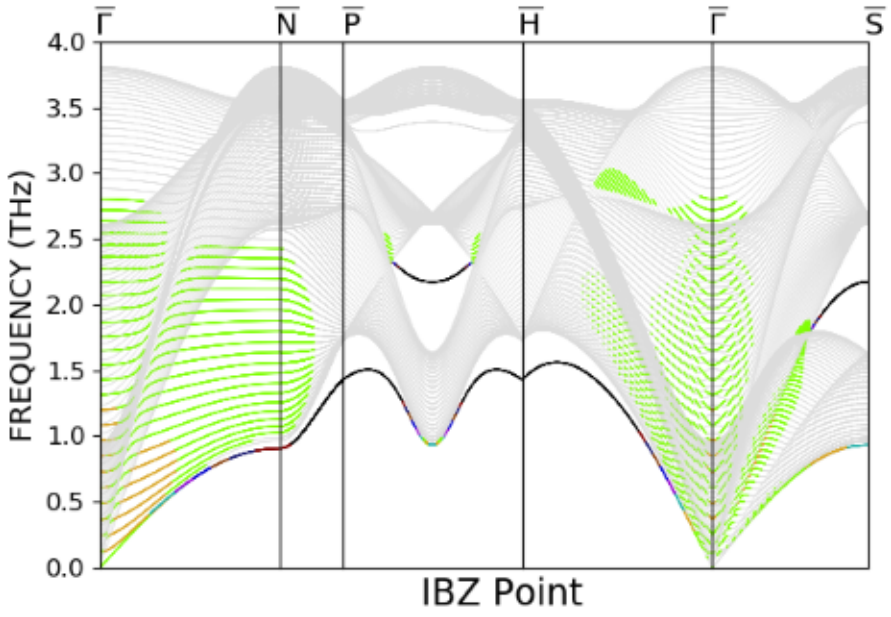

Figure 2.3. Dispersion curves for the (110) surface of Na. Colors indicate localization of modes in the first layer and z direction.

it can be shown that $\overline{X}$ also has a weight of 1, $\overline{M}$ has a weight of 2, and any other point along the zone boundaries has a weight of 4.

Once the list is created, it is a simple matter of calculating a dynamical matrix and finding the associated frequencies for each point in the list. Since each of these dynamical matrices are independent, it is natural to do this calculation using parallel processing. A library called OpenMP [21] is used to parallelize the loop in which the frequencies are found.

Once all frequency calculations are complete, ALE creates a histogram of the frequencies. The histogram is created by iterating through each frequency and adding its weight to the appropriate bin.

To remove some artifacts of the creation of the histogram, a few processes are applied. First, because the raw histogram often has high frequency noise, a low pass filter is applied. The filter used is known as a Gaussian blur, and works as follows. Let $g(\omega)$ be the raw histogram.

The transformed histogram $g'(\omega)$ is the discrete convolution of $g(\omega)$ with a Gaussian, such that

$$g'(\omega) = \sum_{\omega'=0}^{\omega_{max}} g(\omega) e^{-\frac{(\omega-\omega')^2}{2\sigma^2}}, \tag{2.6}$$

where σ is chosen to give the most realistic density of states. Through trial and error, we have found that using 1800 bins with a σ of 2 Hz gives acceptable results.

Finally, the density of states is normalized to have an area under the curve of three. This is because the density represents the available modes of a single atom, and each atom contributes three modes to the the system.

For surface calculations, it is useful to look at the layer resolved x, y, and z densities of states. This is done in much the same way as the layer and direction resolved dispersion curves. However, since the IBZ contains wave vectors pointing in many different directions, it is no longer useful to calculate the localization of modes in shear vertical, shear horizontal, and longitudinal directions. Instead, the weight of each mode is modified by the localization of that mode into the x, y, or z Cartesian directions. For example, in order to calculate the first layer, x direction density states of a slab of material, a frequency with eigenvector $\mathbf{v}$ would be scaled by a weight α given by

$$\alpha = \left(|\mathbf{v} \cdot \mathbf{u_1}|^2 + |\mathbf{v} \cdot \mathbf{u_2}|^2 \right), \tag{2.7}$$

where

$$\mathbf{u_1} = \begin{pmatrix} 1 \\ 0 \\ 0 \\ \vdots \end{pmatrix}$$

and

$$\mathbf{u_2} = \begin{pmatrix} \vdots \\ 1 \\ 0 \\ 0 \end{pmatrix}$$

are the polarizations corresponding to being completely polarized in the x direction on the top and bottom layers of the slab, respectively.

The output of all this machinery is a text file containing two columns of data. The first column contains frequencies in units of Hertz. The second column contains the number of available modes of the corresponding frequency, in units of modes per atom per Hertz. This file is used by a python script called `plot_DOS.py` to create a plot of the density of states.

2.2.6. Calculating Debye Temperatures

Debye temperatures are closely related to moments of the density of states. Specifically, if one has the density of states $g(\omega)$ of a system, then the Debye temperatures $\Theta_D(n)$ are given by

$$\Theta_D(n) = \frac{\hbar}{k_B}\left(\frac{n+3}{3}\frac{\int \omega^n g(\omega)\mathrm{d}\omega}{\int g(\omega)\mathrm{d}\omega}\right)^{\frac{1}{n}}, \quad (n > -3, n \neq 0). \tag{2.8}$$

Special care must be taken for the $n = 0$ Debye tempurature, since (2.8) is undefined in this case. This is remedied by taking the limit as n approaches zero, which yields

$$\Theta_D(0) = \frac{\hbar}{k_B}\left(\frac{1}{3} + \frac{\int \ln(\omega) g(\omega)\mathrm{d}\omega}{\int g(\omega)\mathrm{d}\omega}\right). \tag{2.9}$$

Since we have the density of states function $g(\omega)$, ALE could simply implement (2.8) and (2.9) directly. However, because $g(\omega)$ has been modified to remove artifacts from the creation of the histogram, it is actually more accurate to use the original list of frequencies that was used to create $g(\omega)$ in the first place. This is done by applying a standard trick to convert an integral over $g(\omega)$ to a sum over mdoes. If ω_i is a vector containing all available frequencies and $f(\omega)$ is an arbitrary function of ω, then the following relation holds;

$$\int f(\omega) g(\omega)\mathrm{d}\omega = \sum_i f(\omega_i). \tag{2.10}$$

This means that we can rewrite (2.8) and (2.9) as

$$\Theta_D(n) = \frac{\hbar}{k_B}\left(\frac{n+3}{3}\frac{\sum_i \omega_i^n g(\omega)}{\sum_i 1}\right)^{\frac{1}{n}}, \quad (n > -3, n \neq 0). \tag{2.11}$$

and

$$\Theta_D(0) = \frac{\hbar}{k_B}\left(\frac{1}{3} + \frac{\sum_i \ln(\omega_i)}{\sum_i 1}\right). \tag{2.12}$$

2.2.7. Relaxation

Allowing a slab to relax to equilibrium is essential to get accurate vibrational results. This is obvious from (1.5). All of the mathematics developed so far work under the assumption that the lattice is displaced from near equilibrium.

The fundamental idea behind ALE's relaxation algorithm is simple. Distances between layers are adjusted until an energy minimum has been found. Because ALE allows for multiple layers to be relaxed, it requires a multi-variable minimization algorithm. ALE uses a local, derivative free constrained optimization by linear approximations (LN COBYLA) from the NLopt library of non-linear optimization routines [22].

The NLopt routine requires a function to minimize, and set of inputs to that function to adjust in order to find the minimum. The function ALE minimizes is called

`get_slab_energy(energy, n, relaxation, grad, need_grad, slab).`

The arguments of this function are important, as NLopt expects them to be in this particular order. Each argument fulfills the following purpose;

- `energy` will hold the return value of the function.
- `n` is an integer representing the number of parameters upon which the value of the function depends. In this case, `n` will be the number of layers relaxed
- `relaxation` is a vector holding the distance, in units of angstroms, that each layer moves in the z direction from the unrelaxed position. This vector is the set of parameters that NLopt adjusts to minimize the function. The `relaxation` vector has `n` entries, one for

each layer to be relaxed. Because the top and bottom of the slab must relax symmetrically, the vector only needs to hold the distance moved for the bottom layer. The top layer is then moved in the opposite direction. An example should make this clear. Let `relaxation(1)` be 0.1. Then the first layer on the bottom of the slab will be moved up 0.1 angstroms, and the first layer on the top of the slab will be moved down 0.1 angstroms.

- The arguments `grad` and `need_grad` nominally hold the gradient of the function. NLopt requires these arguments to be in the function declaration, but because a derivative free algorithm is being used, no gradient is required. Thus, in ALE, dummy variables are passed for these arguments.

- `slab` is the variable holding all of the information of the slab being studied, consistent with its use througout all of the code.

After ALE has used NLopt to find the `relaxation` vector which minimizes the energy, it stores the result in a file called `relaxation.dat`. This file will be used the next time ALE is run and the user wishes to study a relaxed slab, so that the relaxation calculation will not need to be repeated.

2.3. Using ALE

2.3.1. Calculation

ALE is a command line utility. It is run through the Linux terminal. The ALE executable sits in the main directory, with all necessary files and folders as sub-directories. In order to run the program, the user simply opens a terminal in the main directory and uses the following command.

```
./ALE
```

ALE is run in 2 stages. First, the user is asked a series of questions to specify the system to be analyzed. This will set up the working directory of the program, and create the list of `atomic_interaction` data.

There are a few things to be aware of. If there is a `force_constants.txt` file in the directory of the system being analyzed, ALE will simply use that file and not perform the calculation of the force constants. If the user wishes to recalculate the force constants (for example, if changes were made to the model), then the old `force_constants.txt` needs to be deleted. If the user is analyzing a slab that has a previously created `force_constants.txt` file, it is essential that the same number of layers are used as were used to create the original file.

When analyzing a slab, ALE will ask the user whether or not the slab should be relaxed. If the slab is to be relaxed and there is a file called `relaxation.dat`, the program will use the data stored in that file to perform the relaxation. If the user wishes to use a different set of data to relax (for example, if the user wishes to relax a different number of layers), then the `relaxation.dat` file must be deleted.

The second stage is to specify the calculation that the user would like to perform. A list of options is presented, and the user makes the choice by entering the number corresponding to the desired calculation.

Most options are self explanatory, although a few deserve special note. The

`Find Model Parameters`

option is used to output lattice constant which minimizes the total energy of the lattice. This option will also print out the charge density at the location of whichever atom is at the center of the basis. This is useful as a sanity check when analyzing slabs of material, since the center of the basis will generally have the same charge density as the material in bulk.

The `Debug` option serves as a way to check anything the user wishes. The user can adjust this section of the code in any way they like. For example, if you were implementing a new lattice structure and wanted to ensure that the correct lattice was being set up in the code, you could place the following code snippet in the `Debug` section of `ALE.f90`.

```
do i=1,10
    print *, slab%atomic_interactions(1,1,i)%vecToAtom
end do
```

This would print out vectors that point from the unit cell at the origin to the 10 nearest unit cells.

2.3.2. Plotting

Plotting in ALE, like performing calculations, is done through the terminal. All plotting is done through Python scripts, contained in the `Plots` sub-directory. These scripts are set up to be fairly generic, so that a single script can handle multiple types of plots.

For example, all plots of surface dispersion curves use the same script called

`plot_surf_dispersion.py.`

In order to specify the particular type of plot to make, the scripts take arguments from the command line. For this example, if one wanted to create dispersion curves for the 110 surface of tungsten with a half monolayer of lithium, after calculating the data, one would run the program with the material name, surface, and coverage in that order as arguments as follows.

```
python plot_surf_dispersion.py Li-W 110 half
```

Other commonly used plotting scripts include `plot_bulk_dispersion_curves.py`, which creates a plot of dispersion curves for the material passed as an argument, and `plot_DOS.py`, which will create a plot of the density of states for the material passed as an argument.

2.4. Changing ALE

ALE uses a makefile to compile. In short, the makefile is a file containing all of the instructions necessary to compile a program. It is used by the `make` program which is included in most linux distributions. The makefile used by ALE has all of the module dependencies built into it, so if the user wishes to add or remove modules, the makefile will need to be updated. Using makefiles give the advantage of only recompiling modules which have been changed, saving compilation time.

If the user makes any changes to the source code, ALE will need to be recompiled. This is done by simply running the `make` program in the directory of the makefile. ALE's makefile is stored in the `Source` subdirectory.

CHAPTER 3
MODEL BUILDING

The purpose of this chapter is to create models which describe interactions between atoms of the same element. This advances our goal of modeling the alkali-metal/transition-metal interface because, as we will see in Chapter 4, the pair-potential interaction between two atoms of different elements can be built from the individual pair-potentials.

The predicted vibrational properties of a lattice will depend on the precise form of the embedding energy $F(\rho)$, the electronic charge density contribution $f(r)$, and the pair-potential interaction $\phi(r)$ between atoms in the lattice. Each of these functions are constructed from experimental inputs.

3.1. Embedding Models

3.1.1. Embedding Energy

We will use an embedding energy model created by Johnson and Oh in 1988 [23]. This model has been successful in describing the alkali metals [24] and tungsten [25], and it takes the form

$$F(\rho) = -\left(E_{coh} - E_{1\nu}^{UF}\right)\left[1 - \lambda \ln(\frac{\rho}{\rho_e})\right]\left(\frac{\rho}{\rho_e}\right)^{\lambda}. \tag{3.1}$$

Here E_{coh} is the cohesive energy of the material, $E_{1\nu}^{UF}$ is the energy required to remove a single atom from the crystal, ρ_e is the equilibrium electron density of an atomic location in the material, and λ is a free parameter which is adjusted to obtain the best fit to experimental vibrational data.

3.1.2. Electron Charge Density Contributions

The model we will use for the electron density contribution function $f(r)$ takes inspiration from Hartree Fock calculations of the wave function of electrons surrounding atomic nuclei [26].

These calculations suggest that, outside of the atom, electron density falls off exponentially. Accordingly, our function takes the form

$$f(r) = f_e e^{-\beta(\frac{r}{r_1}-1)}. \tag{3.2}$$

Here, r_1 refers to the nearest neighbor distance of the bulk material. For each material we model, we choose β to match the decay rate from the Hartree Fock calculations for that material.

Since $f(r)$ only appears in ratios with itself, the term f_e will disappear when performing calculations of a system with a single type of material. When analyzing a bimetallic system, such as Li on W, only ratios of the electron density contribution functions will appear. Thus, the ratio $f_{e,Li}/f_{e,W}$ is chosen to reflect the relative electron contributions from Li and W, once again according to Hartree Fock calculations.

3.2. Alkali Potentials

The inter-atomic potential $\phi(r)$ is the most influential ingredient to the predicted vibrational properties of a metal. As such, it will receive the most thorough treatment of the three defining functions.

A good inter-atomic potential needs to have a few key features. We know that atoms in a lattice tend to be a few angstroms away from each other, so a physically reasonable model of the inter-atomic interaction potential should have a well around $r = r_1$, where r_1 is the nearest neighbor distance of the lattice. In order to enforce that atoms be no closer than the nearest neighbor distance, a good model of the potential should also have a steep wall as r goes to zero. Finally, we know that atoms only significantly interact with their close neighbors, so $\phi(r)$ should flatten out to zero at distances a few times greater than r_1. We will examine two potential models for the alkali metals; a long-range five-shell model and a short-range two-shell model.

3.2.1. Alkali Model Inputs

There are a number of physical inputs which go in to the vibrational calculations. Quantities such as G and C', which are related to the linear elastic constants C_{ij} through

$$G = \frac{1}{5}\left(C_{11} - C_{12} + 3C_{44}\right) \tag{3.3}$$

$$C' = \frac{1}{2}\left(C_{11} - C_{12}\right) \tag{3.4}$$

are used as constraints on the fits to the five-shell models, as these can be calculated from the slope of the predicted dispersion curves of a model. The parameters E_{coh} and $E_{1\nu}^{UF}$ are also used as constraints, in addition to appearing in (3.1). Table 3.1 lists all of the physical inputs which go in to the alkali models we will discuss.

Table 3.1. Physical inputs for the alkali metals.

	Li	Na	K	Rb	Cs	Source
M (amu)	6.94	23.0	39.1	85.5	132.9	[27]
E_{coh} (eV)	1.63	1.11	0.93	0.85	0.80	[27]
$E_{1\nu}^{UF}$ (eV)	0.40	0.36	0.35	0.30	0.28	[27]
a_0 (ang)	3.48	4.24	5.24	5.59	6.05	[27]
G (Mbar)	0.069	0.038	0.019	0.014	0.010	[27]
C' (Mbar)	0.011	0.008	0.004	0.003	0.002	[27]
β	6.17	7.31	8.02	8.09	8.15	[26]
f_e (arb. units)	0.533	0.204	0.111	0.088	0.076	[26]

3.2.2. The Wang-Boercker Potential

Our first approach is the Wang Boercker (WB) potential, which was developed to describe BCC transition metals [28]. We will use a slightly modified version that takes the form

$$\phi(r) = \sum_{n=0}^{7} K_n \left(\frac{r}{r_1} - 1\right)^n e^{-n\alpha\left(\frac{r}{r_1}-1\right)^2}. \tag{3.5}$$

Here, K_n and α are free parameters that we fit to experimental phonon frequencies. The only difference between (3.5) and the original formulation is that we have added an extra K_n, so that the sum goes to $n = 7$ instead of $n = 6$. The parameters for all WB models of the alkalis are shown in Table 3.2.

Table 3.2. Parameters for the WB model of the alkali metals and W. K_n is reported units of eV. The nearest neighbor distance r_1 is expressed in angstroms. The parameter α is unitless.

	Li	Na	K	Rb	Cs
K_0	-0.0604	-0.0532	-0.0511	-0.0491	-0.0355
K_1	-0.1222	-0.0813	-0.1029	-0.1179	-0.1414
K_2	2.0047	1.5904	1.6053	1.6010	1.4498
K_3	-6.5477	-3.9838	-4.6151	-4.2471	-5.7870
K_4	12.4561	3.1373	6.9063	5.1463	17.6172
K_5	-16.0839	0.9927	-6.9093	-3.1482	-34.2555
K_6	12.3512	-2.5894	4.5956	0.9029	34.3281
K_7	-4.0182	0.9831	-1.4398	-0.0873	-13.3849
α	0.170	0.22	0.2	0.04	0.370
r_1	3.016	3.668	4.534	4.841	5.242

The WB potential has been used extensively in EAM modeling [29], and has been very successful. However, since it is a five-shell potential, it could be considered somewhat complicated. Our eventual goal is to model bimetallic interactions, and since little is known about the specifics of the interaction between the alkalis and tungsten and molybdenum, we should consider using a model that assumes less than the WB potential.

3.2.3. The Modified Finnis Sinclair Potential

The second approach to modeling alkali metals will be a modified Finnis Sinclair (MFS) model [30]. This model only extends out to the second shell, and is thus much simpler than the WB model. It takes the form

$$\phi(r) = \left(\frac{r}{r_c} - 1\right)^3 \sum_{n=0}^{3} K_n \left(\frac{r}{r_1} - 1\right)^n. \tag{3.6}$$

As with (3.5), K_n are parameters which are fit to experimental frequencies. The MFS model has only four K_n parameters, compared to the eight K_n parameters of the WB model, making the MFS even simpler. This model has the advantage of having a cutoff distance r_c built in, so that the function and its first two derivatives smoothly go to zero at r_c. We choose r_c to be somewhere between the second and third shell, and choose the exact location so that the first derivative of $\phi(r)$ is zero at r_c. Table 3.3 shows the MFS parameters for the alkalis.

Table 3.3. Parameters for the MFS model of the alkali metals. K_n is reported units of eV. The cutoff distance r_c is expressed in angstroms.

Metal	K_0	K_1	K_2	K_3	r_c
Li	1.0532	6.8813	−7.9559	57.8868	4.9127
Na	0.9432	6.1662	−5.0660	44.9158	5.9731
K	0.9181	5.9587	−5.6169	48.4210	7.3817
Rb	0.7932	5.4395	−6.2800	30.1120	7.8780
Cs	0.7382	4.9395	−5.4595	33.6514	8.5338

3.2.4. Alkali Vibrational Comparison

As discussed in Chapter 1, we can calculate dispersion curves directly from BvK force constants. Dispersion curves calculated in this manner show the closest possible fit to experimental data when working under the harmonic approximation. Because of this optimization, we can use the dispersion curves predicted by BvK force constants as a standard against which we measure the effectiveness of our two models. We can also use the BvK force constants to calculate densities of states and moment Debye temperatures. Figures 3.1, 3.2, 3.3, 3.4, and 3.5 show the pair-potentials, dispersion curves, densities of states, and moment Debye temperatures for Li, Na, K, Rb, and Cs, respectively.

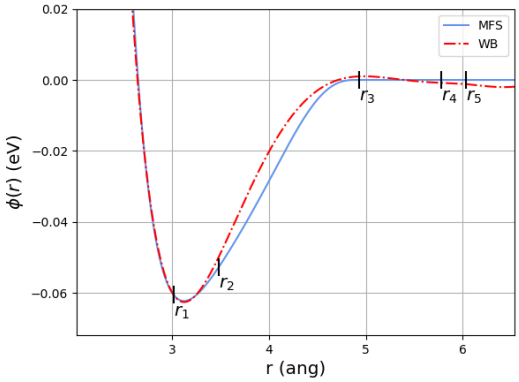

(a) The MFS and WB potentials for Li.

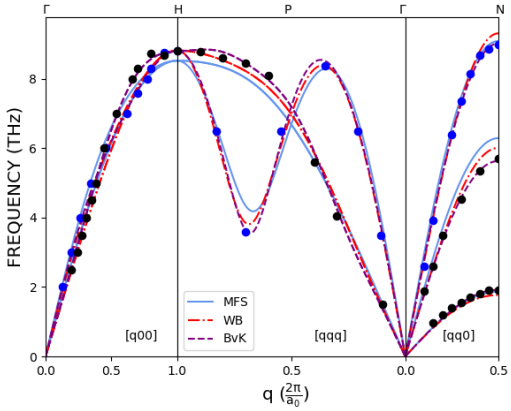

(b) Disperion curves for bulk Li. Blue (black) markers indicate experimental frequencies with longitudinal (transverse) polarizations [31].

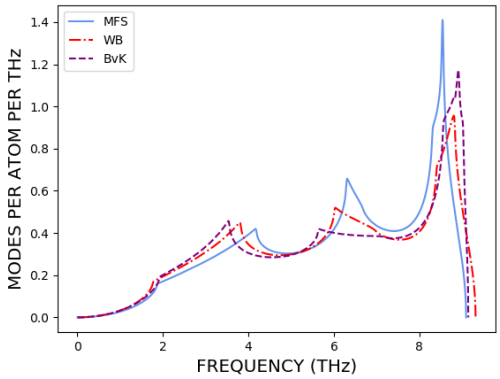

(c) Density of States for bulk Li.

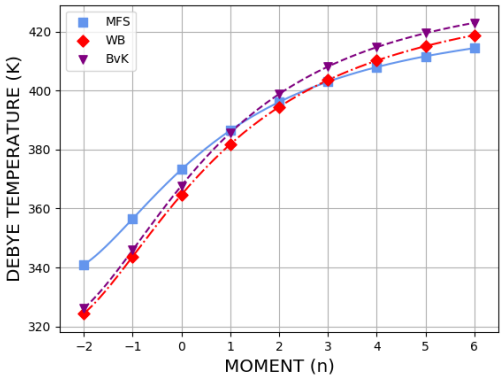

(d) Moment Debye temperatures for bulk Li.

Figure 3.1. Bulk vibrational results for Li using the MFS and WB potentials.

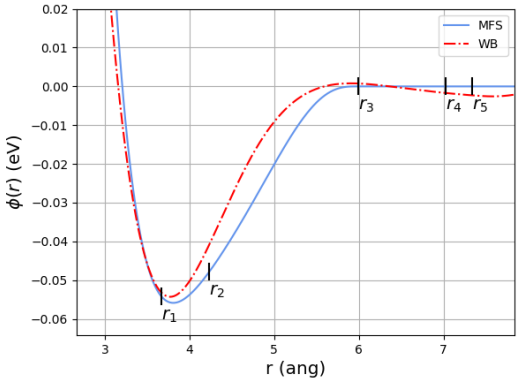

(a) The MFS and WB potentials for Na.

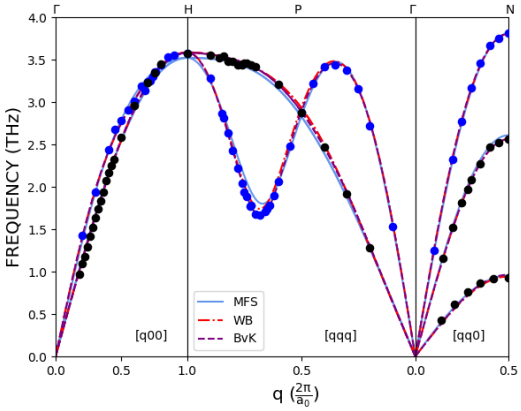

(b) Disperion curves for bulk Na. Blue (black) markers indicate experimental frequencies with longitudinal (transverse) polarizations [32].

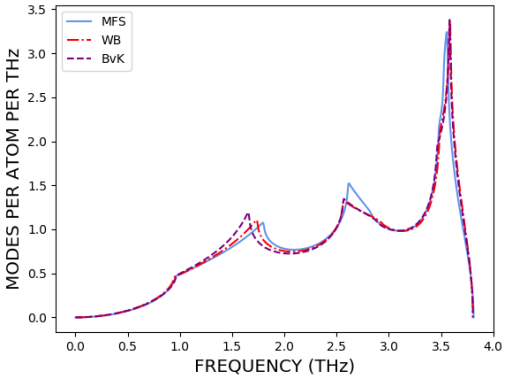

(c) Density of States for bulk Na.

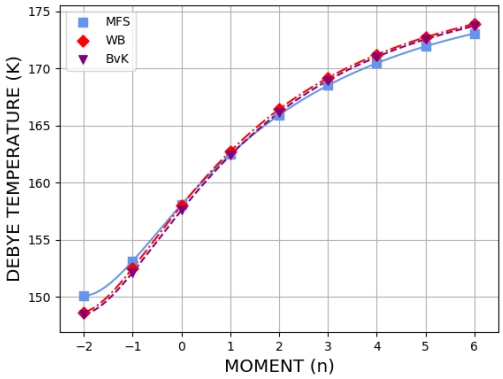

(d) Moment Debye temperatures for bulk Na.

Figure 3.2. Bulk vibrational results for Na using the MFS and WB potentials.

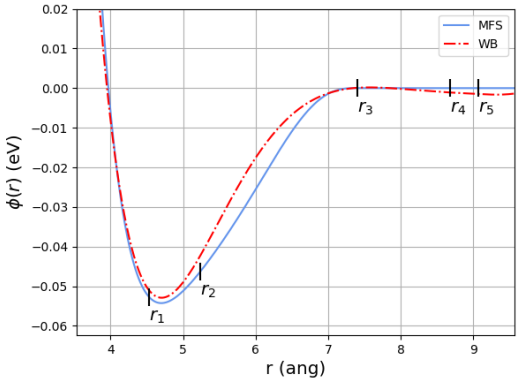

(a) The MFS and WB potentials for K.

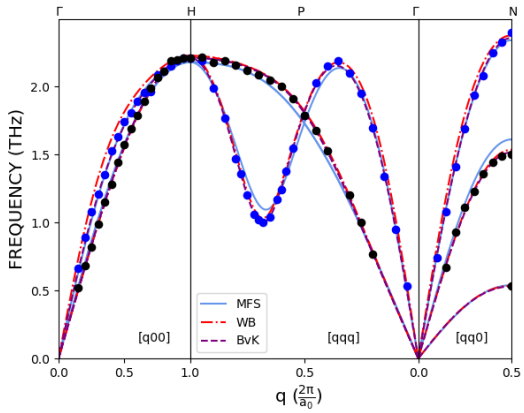

(b) Disperion curves for bulk K. Blue (black) markers indicate experimental frequencies with longitudinal (transverse) polarizations [33].

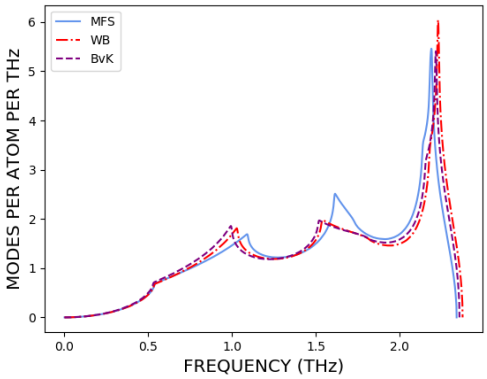

(c) Density of States for bulk K.

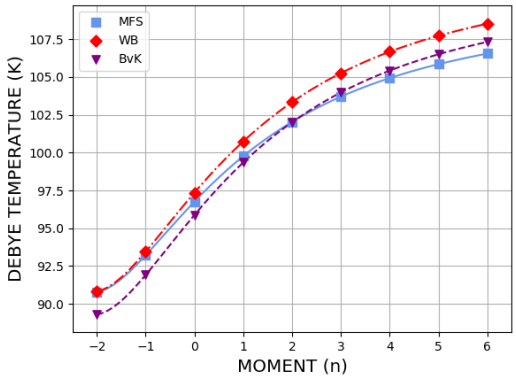

(d) Moment Debye temperatures for bulk K.

Figure 3.3. Bulk vibrational results for K using the MFS and WB potentials.

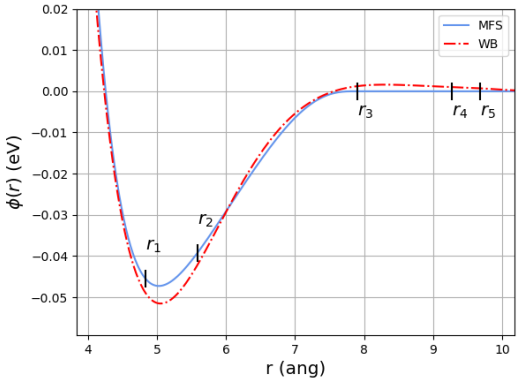

(a) The MFS and WB potentials for Rb.

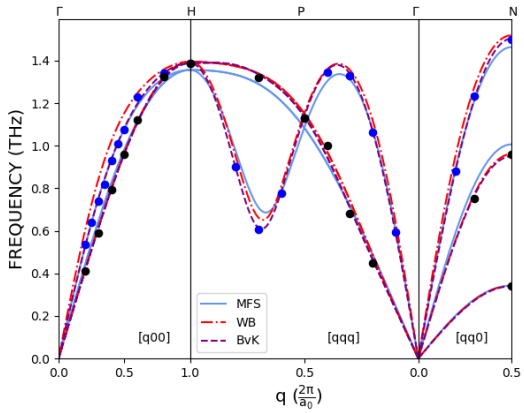

(b) Disperion curves for bulk Rb. Blue (black) markers indicate experimental frequencies with longitudinal (transverse) polarizations [34].

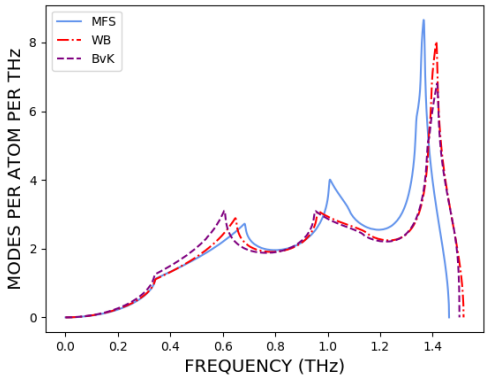

(c) Density of States for bulk Rb.

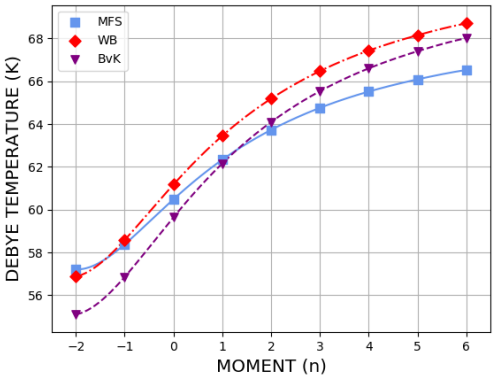

(d) Moment Debye temperatures for bulk Rb.

Figure 3.4. Bulk vibrational results for Rb using the MFS and WB potentials.

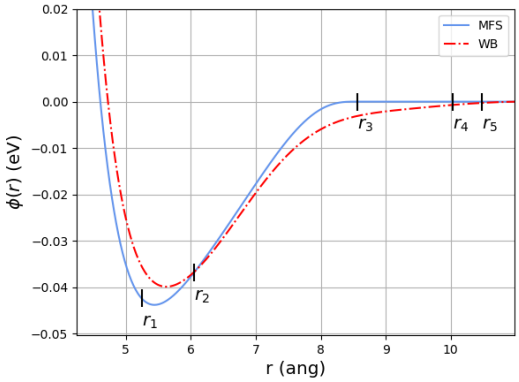

(a) The MFS and WB potentials for Cs.

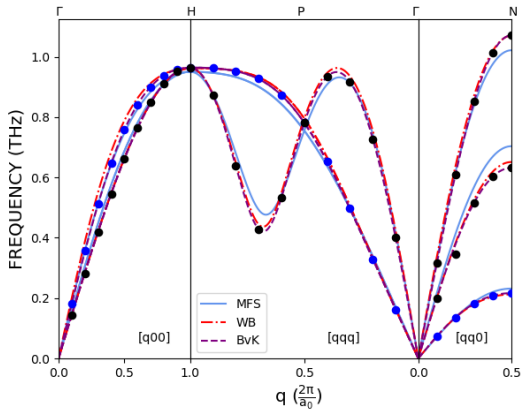

(b) Disperion curves for bulk Cs. Blue (black) markers indicate experimental frequencies with longitudinal (transverse) polarizations [35].

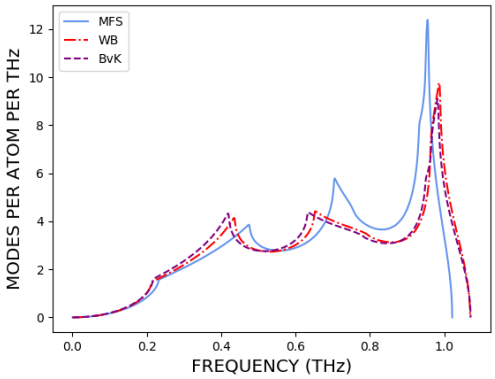

(c) Density of States for bulk Cs.

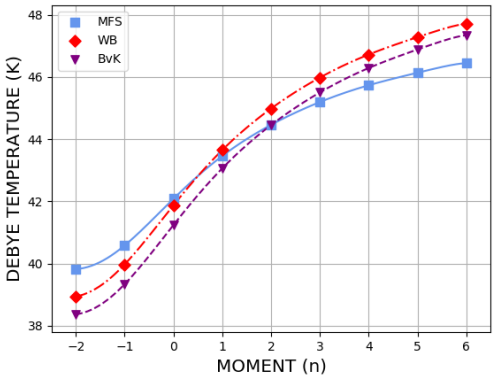

(d) Moment Debye temperatures for bulk Cs.

Figure 3.5. Bulk vibrational results for Cs using the MFS and WB potentials.

Examining these curves, we see that the WB potentials consistently give results much closer to the BvK frequencies. This makes sense, given that the WB model uses eight free parameters which are fit to experimental frequencies, compared to the four free parameters of the MFS model. We also see that the MFS model tends to slightly underestimate the higher frequencies for all alkali's, while overestimating the mid-range frequencies.

3.2.5. Alkali Surface Comparison

As discussed in Chapter 2, surface relaxations can be easily calculated from a given potential by adjusting the distance between layers to minimize the total potential energy of the slab. A

model which predicts good relaxation values is likely to have its potential well in the correct position, since the position and shape of the well are what determine the relaxation.

Though there have not been any experimental investigations into the relaxations of Na and Li, there have been a number of high quality theoretical calculations done. Some of these calculations were done using EAM models similar to what we are using, and some use the more sophisticated density functional theory (DFT). Comparing our model to these theoretical calculations will show that our results are in line with similar investigations. Table 3.4 summarizes these results.

Our results are in good qualitative agreement with both experimental and other theoretical results. Most models give a contraction of the first layer of the 110 surface of Li and Na, in the same range of our results. On the (110) surface, our models show a contraction of the first layer, which matches most of the EAM calcualtions in our table. Our model suggests that the second layer expands very slightly, while most other models predict a slight contraction. However, since the second layer changes are so small, this difference is negligible.

3.3. Transition Metal Potentials

Using an EAM model to describe W and Mo presents a unique challenge. Compared to the alkalis, W and Mo have a complicated electronic structure. Their valence electrons are in d-type orbitals, whose wavefunctions are not spherically symmetric. The alkalis, on the other hand, have spherically symmetric s-type valence electrons. This means that the bonding seen in W and Mo must have some angular dependence. However, the EAM model assumes a potential which depends only on radial distance, and thus cannot realize all of the features of the transition metals.

Because of this complexity, EAM models tend to do less well when describing transition metals. There are models similar to the EAM, like the Modified EAM (MEAM), which do include explicit angular dependence. However, these more complicated models tend to not do much better than a simpler EAM model when used to calculate vibrational data [42]. For this study, we will use a simple two-shell EAM model to describe W and Mo.

Table 3.4. Surface relaxations of the (100) and (110) surfaces of Li and Na. Negative (positive) values signify inward (outward) relaxation. Values are the percentage of the interlayer spacing for a given surface. Δ_{ij} represents the change in distance (compared to the bulk) between layers i and j. Our results from the WB and MFS models are shown with WB and MFS as the technique.

Surface	Δ_{12} (%)	Δ_{23} (%)	Technique	Reference
Li(110)	-0.5		DFT	(Bohnen 1984) [36]
	-2.1	-0.08	EAM	(Guellil 1992) [25]
	1.3	0.0	EAM	(Sklyadneva 1996) [37]
	-1.9	-0.06	EAM	(Wilson 2012) [29]
	-1.34	-0.1	WB	
	-1.18	0.12	MFS	
Li(100)	-3.0		DFT	(Bohnen 1984) [36]
	6.8	-0.6	DFT	(Kokko 1995) [38]
	-2.6	-0.88	EAM	(Guellil 1992) [25]
	5.3	0	EAM	(Sklyadneva 1996) [37]
	-3.2	-0.8	EAM	(Wilson 2012) [29]
	0.89	-1.35	WB	
	0.35	-0.6	MFS	
Na(110)	0		DFT	(Bohnen 1982) [36]
	0		DFT	(Bohnen 1984) [36]
	-1.6 ± 0.5	0.0 ± 0.5	DFT	(Rodach 1989) [39]
	-1.5	-0.07	EAM	(Guellil 1992) [25]
	2.4	0.1	EAM	(Sklyadneva 1996) [37]
	-1.6	-0.0	EAM	(Wilson 2012) [29]
	-2.53	0.04	WB	
	-1.17	0.18	MFS	
Na(100)	-2.0		DFT	(Bohnen 1982) [40]
	-0.7		DFT	(Bohnen 1984) [36]
	0		DFT	(Quong 1991) [41]
	-0.34	-0.91	EAM	(Guellil 1992) [25]
	8.6	0.7	EAM	(Sklyadneva 1996) [37]
	-0.36	-1.1	EAM	(Wilson 2012) [29]
	-2.37	-1.9	WB	
	1.29	-0.56	MFS	

3.3.1. Transition Metal Model Inputs

As we will see, the models for W and Mo depend on fewer parameters than the WB model. Because of this, we cannot use as many constraints as we did when fitting the K_n values in

the WB model. Therefore, we drop the constraints G and C', and no longer think of them as inputs for the transition metal models. There are, of course, still other physical inputs we will use for the calculations, which we detail in Table 3.5.

Table 3.5. Physical inputs for W and Mo models.

	W	Mo	Source
M (amu)	183.84	95.95	[27]
E_{coh} (eV)	8.9	6.82	[27]
$E_{1\nu}^{UF}$ (eV)	3.95	3.2	[27]
a_0 (ang)	3.165	3.147	[27]
β	6.39	5.78	[26]
f_e (arb. units)	1.0	1.284	[26]

3.3.2. The Zhou Wadley Johnson Potential

The first transition metal model is a potential first proposed by Zhou *et al.* [43], which will be called the ZWJ potential. It takes the form

$$\phi(r) = \frac{K_0 e^{-\alpha\left(\frac{r}{r_1}-1\right)}}{1+\left(\frac{r}{r_1}-\kappa\right)^{20}} - \frac{K_1 e^{-\delta\left(\frac{r}{r_1}-1\right)}}{1+\left(\frac{r}{r_1}-2\kappa\right)^{20}}. \tag{3.7}$$

This potential is fairly simple. It has four parameters, K_0, K_1, α, and δ, which are fit to vibrational data. The parameter κ is taken directly from the paper by Zhou *et al.*. Table 3.6 shows the ZWJ parameters for W and Mo.

Table 3.6. Parameters for the ZWJ model of W and Mo. K_n is reported units of eV. The parameters α, δ, and κ are unitless.

Metal	K_0	K_1	α	δ	κ
W	0.8495	1.3862	8.9393	4.5470	0.1392
Mo	0.6292	1.0577	8.1739	3.9876	0.1376

3.3.3. The Johnson and Oh Potential

The second potential we examine for W and Mo is a model created by Johnson and Oh [44], which we will call the JO model. This is yet another two-shell model which takes the form

$$\phi(r) = \sum_{n=0}^{3} K_n \left(\frac{r}{r_1} - 1 \right)^n . \tag{3.8}$$

As with the previous models, the parameters K_n are chosen to fit vibrational data. Table 3.7 show the JO parameters for W and Mo.

Table 3.7. Parameters for the JO model of the W and Mo. K_n is reported units of eV. The nearest neighbor distance r_1 is in units of angstroms.

Metal	K_0	K_1	K_2	K_3	r_1
W	-0.5838	-2.2010	17.7476	-10.4279	2.741
Mo	-0.4647	-1.6132	11.0237	0.8937	2.725

It is important to note that in all of the interatomic potentials we will be using, the potential is set to zero after a certain distance. For example, the WB potential is a five-shell model, which means it allows for interactions between atoms up to a distance of r_5, which is the fifth nearest neighbor distance. For any $r > r_5$, $\phi(r) = 0$. A hard cutoff in the potential might seem to violate the requirement of being physically reasonable, but since the potential is only evaluated at discrete locations in the analysis, such hard corners do not usually have any effect on the calculations.

For relaxation, however, a hard cutoff can introduce difficulties. When calculating the relaxation of a slab, atomic layers are smoothly adjusted, so there is the possibility of a one layer sliding into or out of the cutoff range of another layer. In this regime, rather than cutting off the potential, a simple polynomial is used to smoothly bring the potential to zero. For example, if we were using a five-shell model, a starting position r_s would be chosen so that $r_s > r_5$, and a cutoff position r_c would be chosen, such that $r_s < r_c < r_6$. Then in the region $r_s < r < r_c$,

the potential would take the form

$$\phi(r) = \sum_{n=0}^{5} a_n r^n. \tag{3.9}$$

When $r > r_c$, we set $\phi(r) = 0$. We choose the coefficients a_n to make the potential and its first and second derivatives continuous at r_s and r_c

3.3.4. Transition Metal Vibrational Comparison

Like the alkali vibrational comparison, we will compare each transition metal model's dispersion curves, density of states, and moment Debye temperatures to results calculated from BvK force constants. These are shown for W and Mo in Figures 3.6 and 3.7, respectively. To show that a simple two-shell model is sufficient to describe the transition metals, we also calculate results derived from the WB model for W. As shown in Figure 3.6, the five-shell model performs only marginally better than the two-shell models.

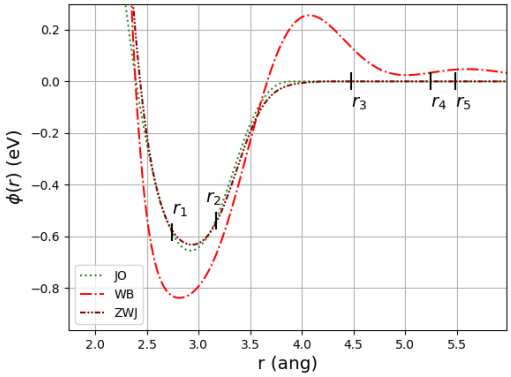

(a) The JO, ZWJ, and WB potentials for W.

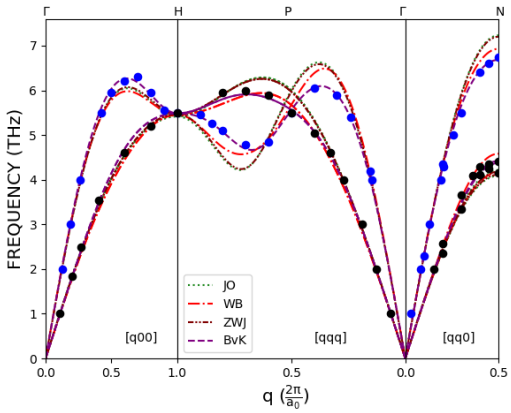

(b) Disperion curves for bulk W. Blue (black) markers indicate experimental frequencies with longitudinal (transverse) polarizations [45].

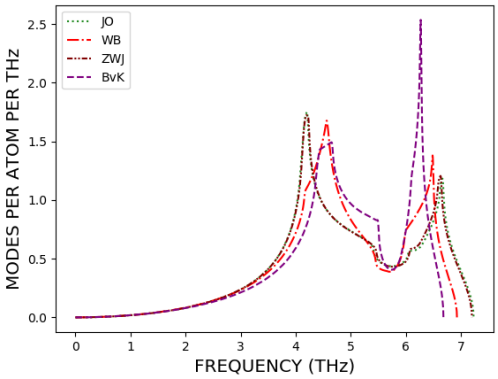

(c) Density of States for bulk W.

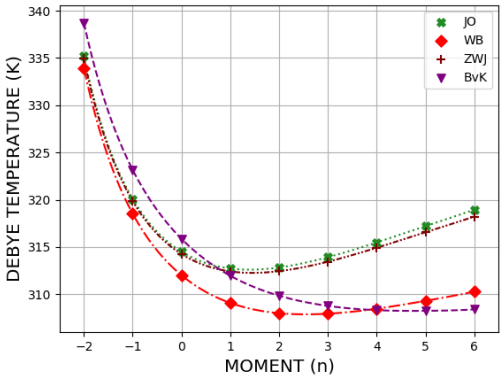

(d) Moment Debye temperatures for bulk W.

Figure 3.6. Bulk vibrational results for W using the JO, ZWJ, and WB potentials.

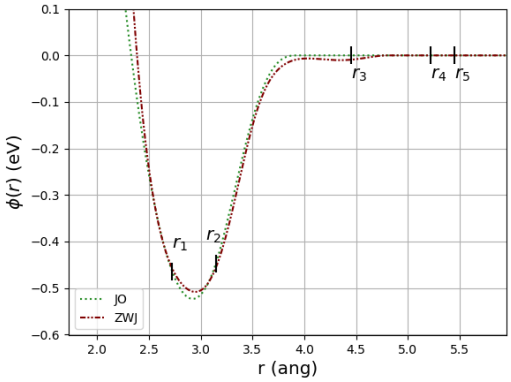

(a) The JO and ZWJ potentials for Mo.

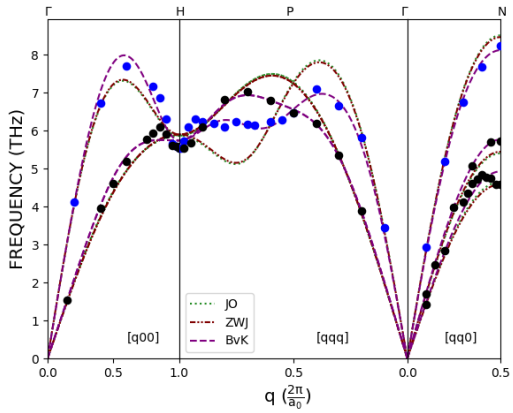

(b) Disperion curves for bulk Mo. Blue (black) markers indicate experimental frequencies with longitudinal (transverse) polarizations [46].

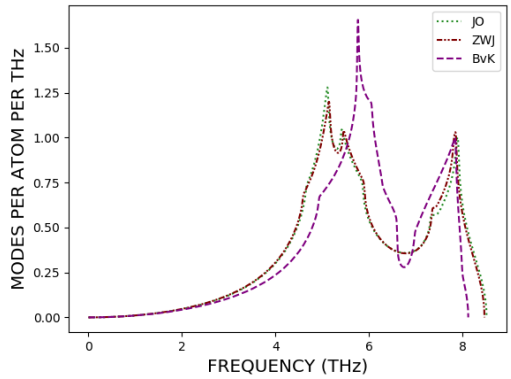

(c) Density of States for bulk Mo.

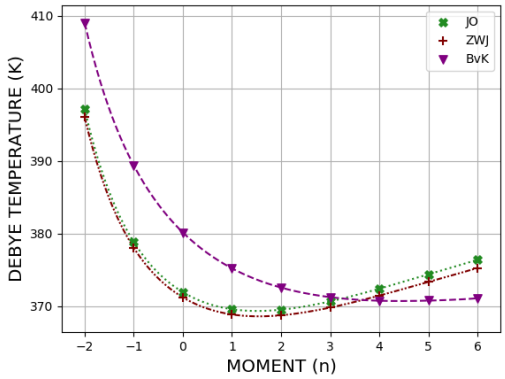

(d) Moment Debye temperatures for bulk Mo.

Figure 3.7. Bulk vibrational results for Mo using the JO and ZWJ potentials.

There is good reason to choose a simple but less accurate two-shell model over a complicated but more accurate five-shell model for W and Mo. Because the WB model uses more free parameters than the JO and ZWJ, it has more structure in the potential. This is evident in Figure 3.6a.

However, this structure is very likely an artifact of our spherically symmetric model being fit to vibrational data from the BCC structure of bulk W. As a rule of thumb, it is wise to assume as little as is needed to describe a system. Thus, using a simpler two-shell model that still does a good job of describing vibrations is preferable to the seemingly more accurate five-shell model.

This simplicity preference is especially important when we model the bimetallic interaction. Even less is know about the interaction between alkali and transition metals, so using the simplest building blocks possible keeps with the spirit of making as few assumptions as needed.

3.3.5. Transition Metal Surface Comparison

The 100, 110, and 111 surfaces of W and Mo have received many theoretical and experimental investigations. This allows us to compare our model to real world data, as opposed to the purely theoretical comparison we did for Li and Na. Tables 3.8 and 3.9 compare experimental and theoretical relaxations to our models predicted relaxations for the 110 and 100 surfaces of W and Mo, respectively.

Table 3.8. Surface relaxations of the (100) and (110) surface of W. Negative (positive) values signify inward (outward) relaxation. Values are the percentage of the interlayer spacing for a given surface. Δ_{ij} represents the change in distance (compared to the bulk) between layers i and j. Our results from the JO and ZWJ models are shown with JO and ZWJ as the technique.

Surface	Δ_{12} (%)	Δ_{23} (%)	Δ_{34} (%)	Technique	Ref.
110	0.0 ± 0.3			LEED	(Buchholz 1975) [47]
	0			LEED	(Van Hove 1976) [48]
	$0. \pm 2$			HEIS	(Smith 1987) [49]
	-3.1 ± 0.6	0.0 ± 0.9		LEED	(Arnold 1997) [50]
	-3.0 ± 1.3	0.2 ± 1.3	0.0 ± 1.0	LEED	(Teeter 1999) [51]
	-2.7 ± 0.5	0.0 ± 0.3		XRD	(Meyerheim 2001) [52]
	-0.64	-0.05		JO	
	-0.57	0.01		ZWJ	
100	-6.3 ± 6.3			LEED	(Van Hove 1976) [48]
	-11.4 ± 1.9			LEED	(Lee 1977) [53]
	-4.4 ± 3.2			LEED	(Debe 1977) [54]
	-5.5 ± 1.5			LEED	(Kirschner 1979) [55]
	-7.0 ± 1.5			SPLEED	(Feder 1981) [56]
	-3.8 ± 10.1			XRD	(Altman 1988) [57]
	4.36	-1.51		JO	
	3.12	-1.18		ZWJ	

Although there is considerable variation in the available data, our results follow the same trends as both theoretical and experimental results.

There have been some experimental measurements done on the vibrational frequencies of the (110) surface of W and Mo. Balden *et al.* [69] and Kröger *et al.* [70] have used electron energy loss (EELS) techniques to measure the phonons localized in the first few layers of W and Mo, respectively. In Figs. 3.8, 3.9, 3.10, and 3.11, we compare their results with the JO model and the ZWJ model predictions for W and Mo.

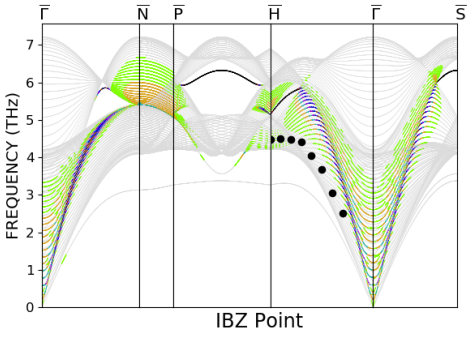

(a) Dispersion curves localized in the first layer longitudinal direction of the 110 surface of W, using the JO model. Black dots represent experimental frequencies.

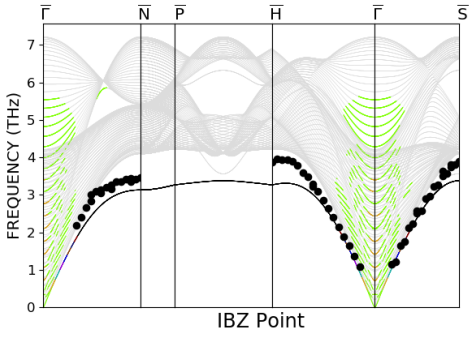

(b) Dispersion curves localized in the first layer shear vertical direction of the 110 surface of W, using the JO model. Black dots represent experimental frequencies.

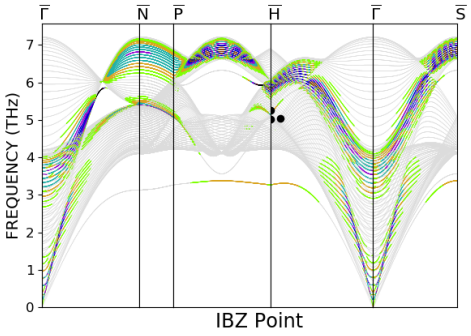

(c) Dispersion curves localized in the second layer longitudinal direction of the 110 surface of W, using the JO model. Black dots represent experimental frequencies.

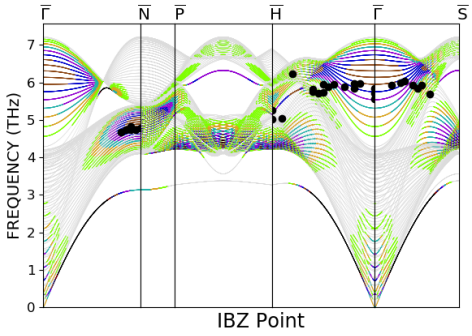

(d) Dispersion curves localized in the second layer shear vertical direction of the 110 surface of W, using the JO model. Black dots represent experimental frequencies.

Figure 3.8. W 110 surface dispersion curves using the JO model.

Table 3.9. Surface relaxations of the (100), (110), and (111) surface of Mo. Negative (positive) values signify inward (outward) relaxation. Values are the percentage of the interlayer spacing for a given surface. Δ_{ij} represents the change in distance (compared to the bulk) between layers i and j. Our results from the JO and ZWJ models are shown with JO and ZWJ as the technique.

Surface	Δ_{12}	Δ_{23}	Δ_{34}	Δ_{45}	Δ_{56}	Δ_{67}	Technique	Ref.
110	-1.6 ± 2.5						LEED	[58]
	-3.9						DFT	[59]
	-3.1	1.9	-0.7	0.4			TB	[60]
	-5.2	1.8					PP	[61]
	-3.3	1.2					LOM	[62]
	-3.3	0.6					MEAM	[63]
	-1.5						EAM	[64]
	-0.8	0.0					EAM	[62]
	-1.7	-0.1	-0.1	-0.1			JO	
	-1.4	0.0	-0.0	-0.0			ZWJ	
100	-11.5						LEED	[65]
	-9.0						DFT	[59]
	-8.5	7.5	-3.8	3.2			TB	[60]
	-10.2	1.3					PP	[61]
	-6.6	2.7	-1.0				LOM	[62]
	-3.3	0.3					MEAM	[63]
	-2.8	-0.2	0.1				EAM	[64]
	1.3	-1.5	0.5				EAM	[62]
	0.1	-1.1	0.3	-0.3			JO	
	0.1	-0.9	0.3	-0.1			ZWJ	
111	$-18. \pm 2$	$4. \pm 4$					LEIS	[66]
	-18.8 ± 1.6	-18.9	6.4	2.2	2.1	0.9	LEED	[67]
	-18.7	-20.3	13.7	-3.0	1.6		DFT	[68]
	-20.5	12.4	-8.0	-1.8			TB	[60]
	-18.3	-7.8	4.1	-1.5	-0.7		LOM	[62]
	-14.0	-16.4	5.5	3.5	-4.3		MEAM	[63]
	-3.2	-13.6	7.6	-1.5	1.4		EAM	[62]
	-4.4	-13.1	5.7	-1.3	-0.9	0.5	JO	
	-4.3	-10.5	5.2	-1.3	-0.6	0.6	ZWJ	

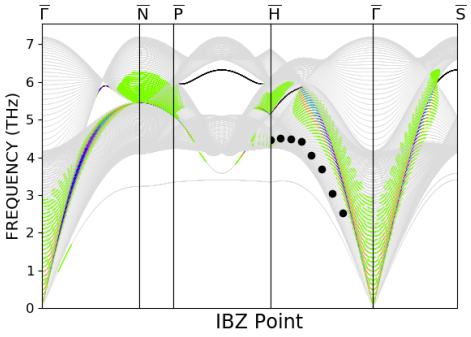

(a) Dispersion curves localized in the first layer longitudinal direction of the 110 surface of W, using the ZWJ model. Black dots represent experimental frequencies.

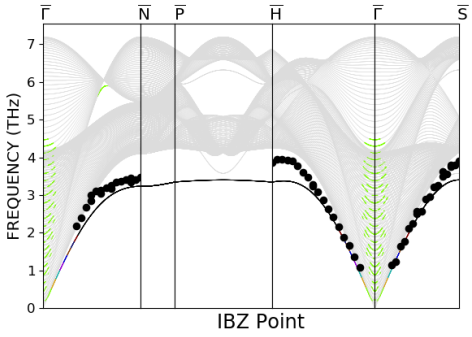

(b) Dispersion curves localized in the first layer shear vertical direction of the 110 surface of W, using the ZWJ model. Black dots represent experimental frequencies.

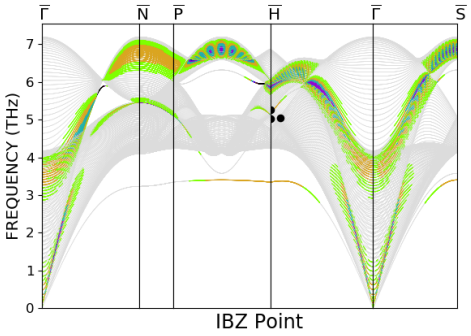

(c) Dispersion curves localized in the second layer longitudinal direction of the 110 surface of W, using the ZWJ model. Black dots represent experimental frequencies.

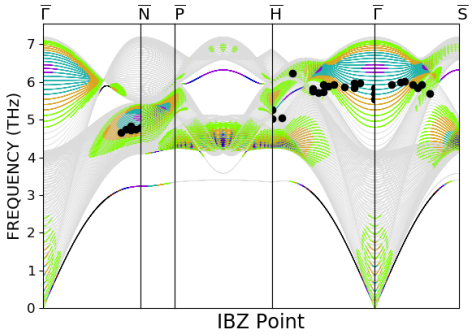

(d) Dispersion curves localized in the second layer shear vertical direction of the 110 surface of W, using the ZWJ model. Black dots represent experimental frequencies.

Figure 3.9. W 110 surface dispersion curves using the ZWJ model.

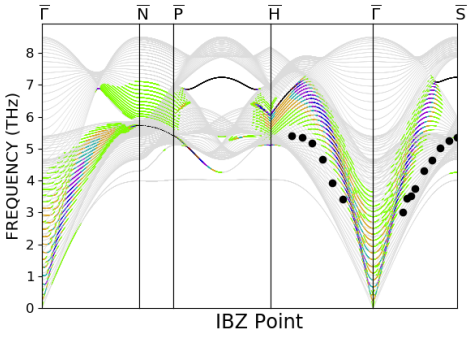

(a) Dispersion curves localized in the first layer longitudinal direction of the 110 surface of Mo, using the JO model. Black dots represent experimental frequencies.

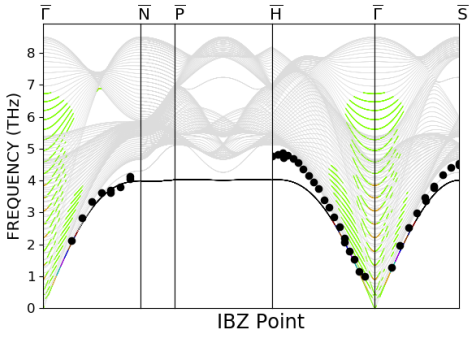

(b) Dispersion curves localized in the first layer shear vertical direction of the 110 surface of Mo, using the JO model. Black dots represent experimental frequencies.

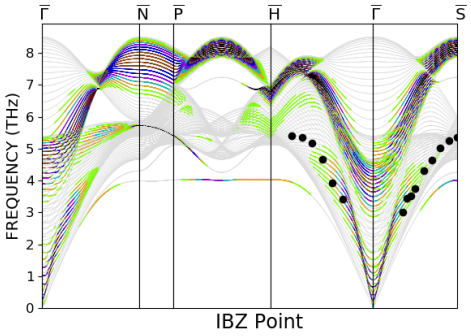

(c) Dispersion curves localized in the second layer longitudinal direction of the 110 surface of Mo, using the JO model. Black dots represent experimental frequencies.

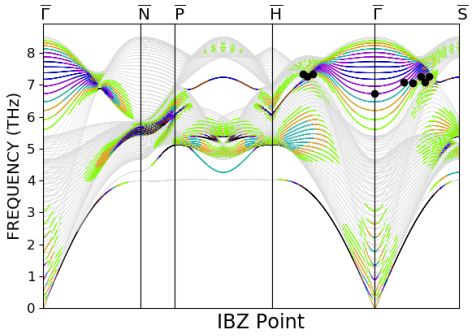

(d) Dispersion curves localized in the second layer shear vertical direction of the 110 surface of Mo, using the JO model. Black dots represent experimental frequencies.

Figure 3.10. Mo 110 surface dispersion curves using the JO model.

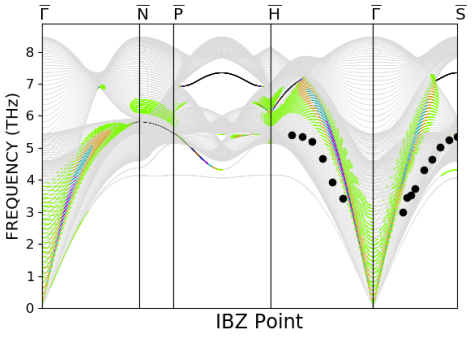

(a) Dispersion curves localized in the first layer longitudinal direction of the 110 surface of Mo, using the ZWJ model. Black dots represent experimental frequencies.

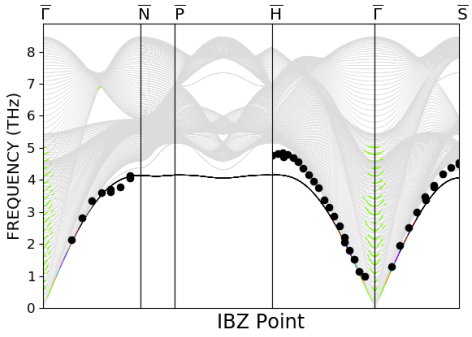

(b) Dispersion curves localized in the first layer shear vertical direction of the 110 surface of Mo, using the ZWJ model. Black dots represent experimental frequencies.

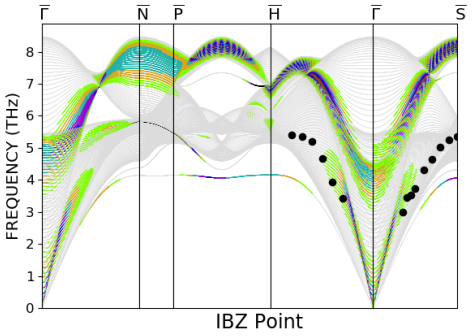

(c) Dispersion curves localized in the second layer longitudinal direction of the 110 surface of Mo, using the ZWJ model. Black dots represent experimental frequencies.

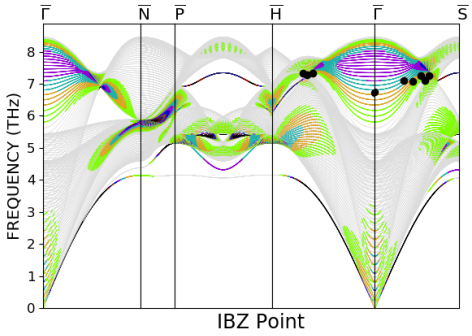

(d) Dispersion curves localized in the second layer shear vertical direction of the 110 surface of Mo, using the ZWJ model. Black dots represent experimental frequencies.

Figure 3.11. Mo 110 surface dispersion curves using the ZWJ model.

Examining these results, it is clear that properly modeling surfaces is a bigger challenge than modeling bulk material. The Rayleigh modes, which are waves that travel along the surface of the slab, can be seen in the longitudinal projections in Figures 3.8a, 3.9a, 3.10a, and 3.11a. Both models underestimate the frequencies of the Rayleigh mode in W and Mo, though the ZWJ model does a slightly better job of this in W. The resonance modes in the shear vertical direction of the second layer line up fairly well with experiment,

3.4. Conclusions

At the beginning of this chapter, we said that our goal was to choose models for the alkali and transition metals that we will use to build the heterogeneous potential. Our choice will be made to balance the accuracy of the model with the model's simplicity. As we have discussed, it is preferable that our models make as few assumptions as possible, while still giving accurate prediction.

While we might reasonably model the interaction between alkali metals with a five-shell spherically symmetric potential, using a long range model for W should be avoided. As we saw in Figure 3.6a, the WB model for W has too much structure in the potential to have confidence in applying it to our heterogeneous systems. For this reason, we choose a two-shell model over a five-shell model for the transition metals.

The ZWJ and JO models gave nearly identical results in the bulk for W and Mo, but the surface vibrations were slightly closer to experiment using the ZWJ model. Therefore, we will use the ZWJ model for W and Mo to build the heterogeneous potential.

For the alkali metals and W, we saw that five-shell WB model outperformed the MFS model for the alkalis, and the JO and ZWJ for W. However, the WB model has nine free parameters we fit to experiment, as opposed to the four free parameters in the MFS model. The WB potential is also a relatively long-range model, with interactions reaching out to the fifth shell. Since we are using a two-shell model for W and Mo, it is prudent to do the same with the alkalis. Therefore, we will use the MFS potential, which still matches experiment quite well, to build heterogeneous potential.

CHAPTER 4
HETEROGENEOUS POTENTIAL

The aim of this chapter is to develop a model of the interaction between a layer of alkali metals and a W or Mo substrate. There have been several approaches to heterogeneous modeling in the literature, such as Fu *et al.* using a Morse potential to describe the interaction between copper and nickel [71], and Johnson's formulation of a heterogeneous potential [72]. We attempt to describe the heterogeneous potential using the Johnson prescription and a ZWJ potential described in (3.7) in Chapter Three. We also present a new method to construct the heterogenous potential, based on linear combinations of the two homogeneous potentials of the system we wish to study.

The decision of which heterogeneous model to use will be based on how well each model reproduces experimental observations, as well as how it compares to other theoretical calculations that have been done. We examine experimentally determined heights of alkali layers, alkali layer binding energies, and alkali vibrational frequencies.

4.1. Proposed Models

4.1.1. The Johnson Prescription

Our first approach to modeling the heterogeneous potential is the prescription given by Johnson [72], which we refer to as JP. This approach was developed in 1989 to extend EAM models for monatomic FCC metals to alloys. It has since been widely used to study Ag-Ti systems [73], Al-Ni nanowires [74], and to describe Ni-Ti alloys [75].

The Johnson prescription builds the heterogeneous potential $\phi_{A-B}(r)$ for two metals, which we call A and B, out of the individual potentials $\phi_A(r)$ and $\phi_B(r)$. The heterogeneous potential takes the form

$$\phi_{A-B}(r) = \frac{1}{2}\left[\frac{f_B(r)}{f_A(r)}\phi_A(r) + \frac{f_A(r)}{f_B(r)}\phi_B(r)\right]. \tag{4.1}$$

This approach has the aesthetic advantage of leaving the potential unchanged under transformations of the electron density function $f_\alpha(r)$. This feature is also present in the embedding energy function $F_\alpha(\rho)$.

4.1.2. Linear Combinations

Building off of the Johnson prescription, we attempt to describe the heterogeneous potential as a general linear combination of the monatomic potentials. We call this approach LC, and use the form

$$\phi_{A-B}(r) = \alpha_A \phi_A(r) + \alpha_B \phi_B(r), \tag{4.2}$$

where α_A and α_B are some constant parameters for materials A and B. This allows us to tune the parameters α_A and α_B to possibly achieve a better fit to experimental data.

4.1.3. The ZWJ Potential

Our final approach is to adjust the ZWJ potential discussed in Chapter 3 to model a heterogeneous, rather than homogeneous, interaction. This approach differs from the linear combination and Johnson prescription approaches by not depending on the individual potentials of the materials we wish to model. Instead, we say that the interaction between two materials A and B, ϕ_{A-B},is given by

$$\phi_{A-B}(r) = \frac{K_0 e^{-\alpha\left(\frac{r}{r_1}-1\right)}}{1+\left(\frac{r}{r_1}-\kappa\right)^{20}} - \frac{K_1 e^{-\delta\left(\frac{r}{r_1}-1\right)}}{1+\left(\frac{r}{r_1}-2\kappa\right)^{20}}. \tag{4.3}$$

In this potential, we can see which parameters control which features. The coefficients K_0 and K_1 will control the depth of the potential well, The unitless parameters α and δ control the curvature, and therefore the calculated force constants. The parameter r_1 will control the position of the potential well, and will therefore largely determine the relaxed height of the alkali layer. Finally, κ will determine how quickly the potential will go to zero.

In order to use (4.3), we need to specify each of the six parameters just discussed. When we used the ZWJ model for W and Mo, many of these parameters were determined by physical constraints. For example, the parameter r_1 was fixed to be the nearest neighbor distance in the

bulk, and κ was taken directly from the original paper by Zhou *et. al* [43]. Our approach is to allow all six parameters to be free, and fit them to experimental and other theoretical results. The procedure for doing this is outlined in the following section.

4.2. Mo-Li Model Comparison

4.2.1. Parameter Fitting

The parameters used for the linear combination model and the ZWJ potential model are determined by least square fitting. We consider the outputs of the model to be the the frequencies of the three modes of the alkali layer, which we will call ν_1, ν_2 and ν_3. These modes are obtained by holding the substrate layers fixed, and only allowing the alkali layer to be dynamic. We also assume that the wave vector is at Γ. This reduces the dynamical matrix to a size of 3×3, and is consistent with the method used by the density functional calculations. The remaining two target values are the height of the alkali layer h, and the binding energy of the alkali layer E.

These outputs can be thought of as functions of the parameters of the model. Thus, if we wish to fit the model to some target outputs $\bar{\nu}_i$, $\bar{h}$, and $\bar{E}$, we must minimize the least-squares function S, where

$$S = \frac{\sum_{i=1}^{3} w_i \left(\frac{\nu_i}{\bar{\nu}_i} - 1\right)^2 + w_4 \left(\frac{h}{\bar{h}} - 1\right)^2 + w_5 \left(\frac{E}{\bar{E}} - 1\right)^2}{\sum_{i=1}^{5} w_i}. \tag{4.4}$$

We use the ratio of the model output to the target output because our five targets have different units, and this method lets us calculate a unitless goodness of fit. We give ourselves the choice of weights w_i, which allow us to adjust the fit to do better job matching frequencies, the binding energy, or the alkali height.

For the target values of the Li-Mo interaction, we use results for a coverage of $\theta = 0.25$ on the (110) surface from Zhou *et al.* [76]. Equation 4.4 is minimized using NLopt's COBYLA routine [22]. This is the same routine used to perform surface relaxation. Table 4.1 details the model and target outputs.

Our choice of weights reflects our end goal. We are most interested in describing vibrational properties, and so we give special attention to accurate frequency measurements. A choice of $w_i = 1$ treats all target values equally, but because there are three frequencies in the set of target values, we can think of this choice as emphasizing a good fit to frequencies.

4.2.2. Mo-Li Results

To determine how well each model does, we compare their predicted alkali frequencies, alkali layer heights, and alkali binding energies for a quarter monolayer of Li on the 110 surface of W and Mo to experimental results, as well as density functional calculations that have been performed. We choose these outputs to compare because there has been significant work done on Li/Mo 110 surfaces. Thus, we have many quality data points to which we can compare our models. Tables 4.1 and 4.2 show the results for Li/Mo (110) with a coverage of $\theta = 0.25$ and $\theta = 1$, respectively.

Table 4.1. Quarter monolayer of Li on the 110 surface of Mo experimental and theoretical values for the height of the alkali layer in angstroms, the binding energy (BE) of the alkali layer in eV, and the vibrational frequencies of the alkali layer in THz. The least square error uses result from Zhou *et. al* as target parameters.

Height	BE	ν_1	ν_2	ν_3	Technique	Reference	Error
		10.2	5.4		HREELS	(Kröger 2000) [77]	
2.33	2.30	10.2	5.8	4.1	DFT	(Zhou 2009) [76]	
2.08	2.06				MEAM	(Vella 2017) [78]	
2.27	2.14	11.48	6.35	6.25	JP		0.0616
2.31	2.04	10.93	5.8	4.08	LC		0.0039
2.47	2.36	10.12	5.82	4.12	ZWJ		0.0003

These results show a few salient features. First, the linear combinination and ZWJ potentials far outperform the Johnson prescription. This is not surprising; the Johnson prescription introduces no new parameters. The linear combination approach introduces two free parameters, and the ZWJ potential introduces six. It stands to reason that a model with more degrees of freedom can better fit target data than one with fewer degrees af freedom. Since both the

Table 4.2. Full monolayer of Li on the 110 surface of Mo experimental and theoretical values for the height of the alkali layer in angstroms, the binding energy (BE) of the alkali layer in eV, and the vibrational frequencies of the alkali layer in THz. The least square error uses result from Zhou *et. al* as target parameters.

Height	BE	ν_1	ν_2	ν_3	Technique	Reference	Error
		9.2			HREELS	(Kröger 2000) [77]	
2.13	2.30	9.9			Li-Mo clusters	(Müller 2002) [79]	
2.21	2.18	9.2	6.8	3.7	DFT	(Zhou 2009) [76]	
2.21	2.09				MEAM	(Vella 2017) [78]	
2.3	2.22	11.1	6.17	5.94	JP		0.0842
2.36	2.14	10.27	5.34	3.72	LC		0.0136
2.53	2.48	9.75	6.66	3.28	ZWJ		0.0114

linear combination and ZWJ potentials performed well on the full monolayer, to which they were not fit, it seems as though these approaches are viable.

The fitted parameters for the linear combination and ZWJ models are shown in Tables 4.3 and 4.4, respectively. Figure 4.1 shows all three model potentials for Mo-Li interaction, as well as the individual Mo and Li potentials.

Table 4.3. The parameters for the linear combination interaction of Mo and Li.

α_{Li}	α_{Mo}
1.654	0.198

4.3. Target Parameters

Our end goal is to model all of the alkali metals on W and Mo, not just Li on Mo. However, there have been very few theoretical or experimental investigations into Na, K, Rb, or Cs on W and Mo. We have developed a method to come up with target parameters for the remaining

Table 4.4. The parameters for the ZWJ interaction of Mo and Li.

r_1 (ang)	K_0 (eV)	$K_1(eV)$	α	δ	κ
2.808	1.444	1.659	8.137	6.561	0.216

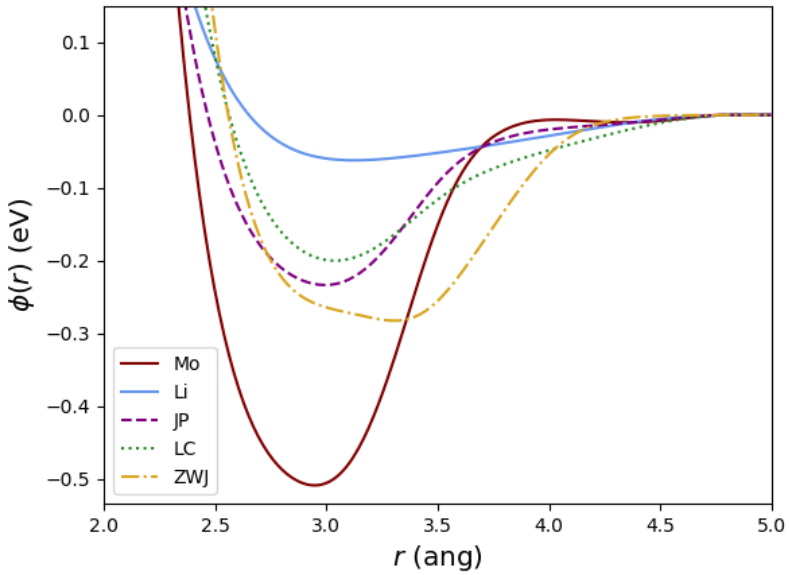

Figure 4.1. The Johnson prescription potential, the linear combination potential, and the ZWJ potential for the interaction of Li and Mo using the frequency set of weights. The potentials of Li and Mo are also shown in blue and red, respectively.

alkali-metal/transition metal systems, which we outline below.

It is important to note that the following method is very much heuristic. We do not expect the target parameters we come up with to be perfectly accurate. Rather, we use this method to come up with values that we feel are reasonably close to what an experimental investigation might yield, solely for the purpose of building our models.

4.3.1. Target Binding Energies

Kawano [80] determined the binding energies of low coverages of Li, Na, K, and Cs on W(110), and the results are shown in Table 4.5.

Table 4.5. Binding energies of alkali metals on W(110), as measured by Kawano.

Alkali Metal	Binding Energy (eV)
Li	2.56 ± 0.10
Na	2.54 ± 0.05
K	2.86 ± 0.05
Cs	3.00 ± 0.05

Since we do not expect binding energies to vary greatly for different low coverages, these results give us clear target parameters for the binding energy of a quarter monolayer of the alkali metals on W(110), with the exception of Rb. Following the pattern in Table 4.5, we expect that the binding energy of Rb on W(110) to be somewhere between 2.86 and 3.0 eV. Therefore, we use a target binding energy of 2.93 eV for a quarter monolayer of Rb on W(110).

However, we still need target binding energies for the alkali metals on Mo(110). These will be obtained by a simple scaling argument. We expect the ratio of binding energies of an alkali on W and the same alkali on Mo to be about constant for all alkali metals. That is, for any two alkali metals A and B, we expect that the binding energy E of A satisfies

$$\frac{E_{A,Mo(110)}}{E_{A,W(110)}} = \frac{E_{B,Mo110)}}{E_{B,W(110)}}. \tag{4.5}$$

Using the results of Kawano [80] for the binding energy of Li on W(110), and the results of Zhou *et. al* [76] for the quarter monolayer coverage binding energy of Li on Mo(110), we estimate that the scaling factor to convert between W(110) binding energies and Mo(110) binding energies is

$$\frac{E_{Li,Mo(110)}}{E_{Li,W(110)}} = 0.85 \tag{4.6}$$

4.3.2. Target Frequencies

We can get an idea of how the vibrational frequencies of an alkali layer change as we change the alkali metal by examining the dynamical matrix. Referring back to (1.10), we note that for a given model, and calling the alkali metal A, the calculated frequencies ω_i^A for the alkali layer will be proportional to the inverse square root of the mass M_A of the alkali atom. Expressed more clearly, we say that

$$\omega_i^A = \frac{\alpha_i^A}{\sqrt{M_A}}. \tag{4.7}$$

where α_i is some constant.

This implies that, so long as the models for the different alkali metals do not vary greatly, and we know the frequencies for alkali A, we can estimate the frequencies for a different alkali B via

$$\omega_i^B = \sqrt{\frac{M_A}{M_B}}. \tag{4.8}$$

This method is supported by a measurement from Lopinski *et. al* [81], who measured the highest frequency of a half monolayer of Li and Na on Mo(100), and found that Li has a frequency of 9.2 THZ, and Na has a frequency of 4.6 THz. The mass of Li is 7 amu, while the mass of Na is 23 amu. This means that (4.8) estimates a frequency of 5.08 THz for the Na frequency, which differs by only ten percent from the experimental value.

Because we don't expect the frequencies to differ significantly between an alkali on W and that same alkali on Mo, we will use the same target frequencies for Li on Mo as we do for Li on W. So, using the results from Zhou *et. al* [76] as our base case, we can estimate target frequencies for all ten alkali-metal/transition-metal models we wish to construct.

4.3.3. Target Heights

We obtain our target heights through a simple geometrical argument. Often, it is useful to think of the atoms in a lattice as a collection of hard spheres, all in contact. In this view of things, the spheres would have a radius that is one half the nearest neighbor distance in the bulk material. This view allows us to imagine an alkali atom sitting on top of the (110) surface of a bcc substrate at the long-bridge site, as shown in Figure 4.2.

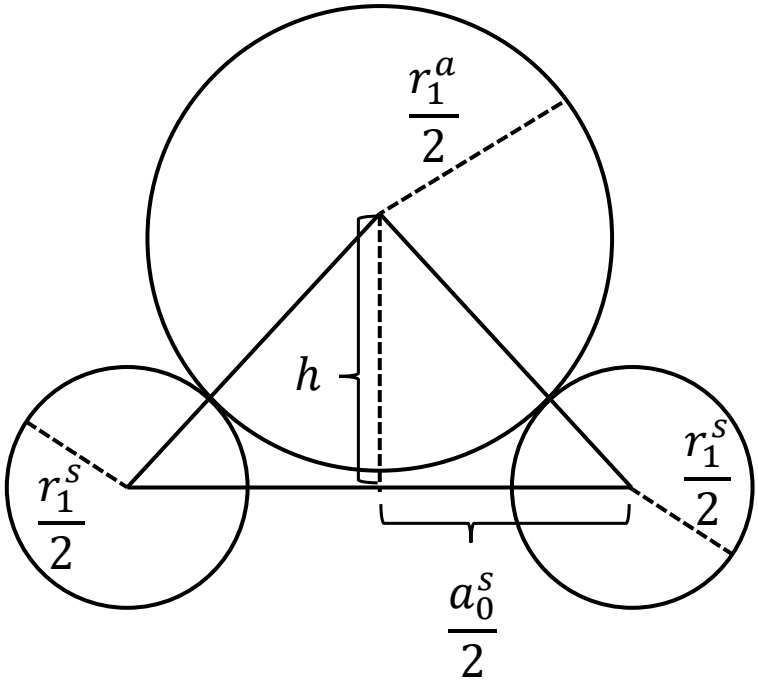

Figure 4.2. A geometric view of an alkali atom sitting on a transition metal substrate. The parameters r_1^s and r_1^a refer to the nearest neighbor distance in the substrate and alkali bulk, respectively. The term a_0^s refers to the lattice constant of the substrate.

From this figure, we can estimate the height h of a layer of alkali atoms with nearest neighbor distance r_1^a on the (110) surface of a bcc substrate with nearest neighbor distance r_1^s and lattice constant a_0^s. This is done by simply applying the Pythagorean theorem, so that

$$h = \frac{1}{2}\sqrt{(r_1^s + r_1^a)^2 - (a_0^s)^2}. \tag{4.9}$$

Applying (4.9) to Li on Mo(110), we get a predicted height of 2.4 angstroms, which differs from the calculation from Zhou *et. al* [76] by only three percent. Therefore, we are confident that (4.9) gives good heuristic results.

4.3.4. Target Summary

Applying these heuristic methods, we have come up with target parameters for all ten alkali-metal/transition-metal models we want to study. The results are organized in Table 4.6.

Table 4.6. Target parameters for Li, Na, K, Rb, and Cs on W and Mo. These results are used to build models using the ZWJ and linear combination potentials. The DFT results from Zhou *et. al* [76] have been used for the height of Li on Mo(110) and, rather than the estimated heights.

System	ν_1 (THz)	ν_2 (THz)	ν_3 (THz)	h (ang)	E (eV)
W-Li	4.1	5.8	10.2	2.402	2.56
W-Na	2.262	3.2	5.627	2.787	2.54
W-K	1.73	2.45	4.32	3.275	2.86
W-Rb	1.173	1.66	2.919	3.444	2.93
W-Cs	0.941	1.33	2.341	3.664	3.0
Mo-Li	4.1	5.8	10.2	2.33	2.3
Mo-Na	2.262	3.2	5.627	2.782	2.282
Mo-K	1.73	2.45	4.32	3.27	2.57
Mo-Rb	1.173	1.66	2.919	3.439	2.632
Mo-Cs	0.941	1.33	2.341	3.659	2.695

4.4. Model Results

With target parameters specified, we can now apply our fitting routine to the linear combination and ZWJ models for the ten alkali-metal/transition-metal systems we wish to study. For comparison, we include the calculated least square error for the Johnson prescription, even though no fitting is done for this potential. The results for all systems are organized in Table 4.7

Examining these results, it is clear that the ZWJ model consistently performs the best for all systems. This is not at all surprising; as discussed earlier, the ZWJ introduces six free parameters that are tuned to match the target outputs.

What is interesting to note is the failure of the Johnson prescription for the larger alkali metals. Examining the data, it appears as though the error for the Johnson prescription increases

Table 4.7. Target parameters for a quarter monolayer of Li, Na, K, Rb, and Cs on W and Mo.

System	Model	ν_1 (THz)	ν_2 (THz)	ν_3 (THz)	h (ang)	E (eV)	Error
W-Li	JP	7.37	7.94	13.81	2.28	2.48	0.1811
	LC	4.08	6.05	11.17	2.30	2.00	0.0119
	ZWJ	4.16	5.78	10.18	2.47	2.33	0.0023
Mo-Li	JP	6.25	6.35	11.48	2.26	2.14	0.0616
	LC	4.08	5.81	10.93	2.31	2.04	0.0039
	ZWJ	4.02	5.91	10.10	2.48	2.35	0.0005
W-Na	JP	4.38	4.84	8.46	2.38	2.26	0.2857
	LC	2.26	3.53	6.39	2.47	1.58	0.0373
	ZWJ	2.22	3.13	6.02	2.66	2.35	0.0026
Mo-Na	JP	3.40	3.57	6.74	2.42	1.67	0.0783
	LC	2.28	3.44	6.30	2.47	1.60	0.0244
	ZWJ	2.21	3.13	6.09	2.71	2.20	0.0019
W-K	JP	4.40	5.62	9.08	2.41	3.69	1.0847
	LC	1.77	2.75	4.88	2.49	1.39	0.0708
	ZWJ	1.79	2.48	4.63	3.53	2.76	0.0027
Mo-K	JP	3.60	3.89	7.12	2.45	2.31	0.4012
	LC	1.79	2.57	4.65	2.48	1.39	0.0559
	ZWJ	1.79	2.46	4.34	3.55	2.54	0.0018
W-Rb	JP	3.03	4.17	6.48	2.41	4.13	1.3074
	LC	1.21	1.86	3.25	2.49	1.30	0.0835
	ZWJ	1.21	1.69	3.15	3.57	2.77	0.0023
Mo-Rb	JP	2.47	2.98	5.07	2.44	2.55	0.4951
	LC	1.46	1.61	2.78	2.32	1.35	0.0831
	ZWJ	1.22	1.67	2.91	3.63	2.60	0.0009
W-Cs	JP	2.66	3.92	5.89	2.42	5.26	2.02
	LC	0.99	1.45	2.50	2.48	1.21	0.0951
	ZWJ	0.99	1.37	2.53	3.70	2.75	0.0034
Mo-Cs	JP	2.16	2.87	4.63	2.44	3.20	0.8262
	LC	0.98	1.44	2.52	2.49	1.26	0.0800
	ZWJ	0.95	1.31	2.38	3.74	2.68	0.0002

as we increase the size of the alkali metals. Lithium is around the same size as W and Mo, and so the Johnson prescription performs fairly well in that regime. However, making our way down to Cs on W, the error for the Johnson prescription is three orders of magnitude greater than the error for the ZWJ model. The reason for this increasing error is somewhat more apparent when the potentials are directly compared, as in figs. 4.3 and 4.4.

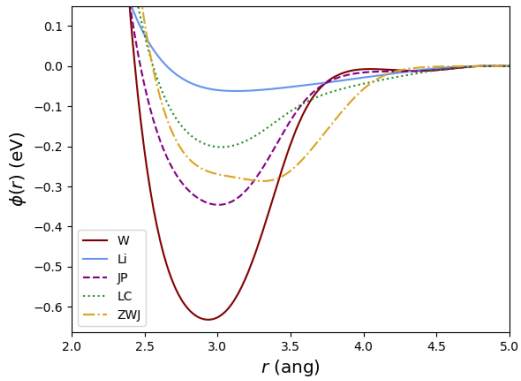

(a) The W-Li heterogeneous interactions.

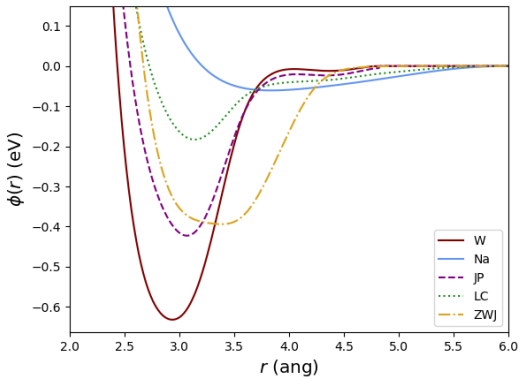

(b) The W-Na heterogeneous interactions.

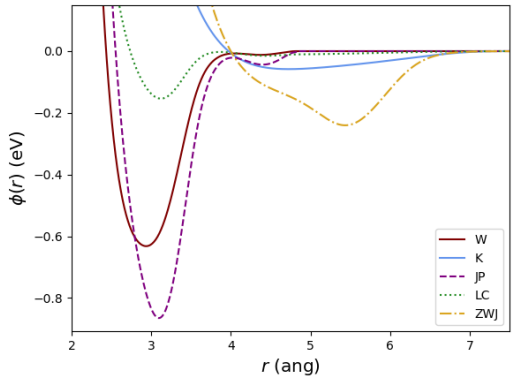

(c) The W-K heterogeneous interactions.

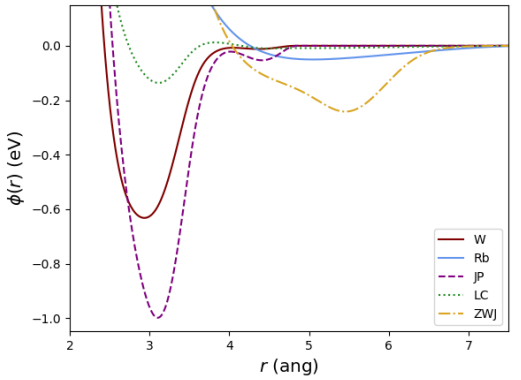

(d) The W-Rb heterogeneous interactions.

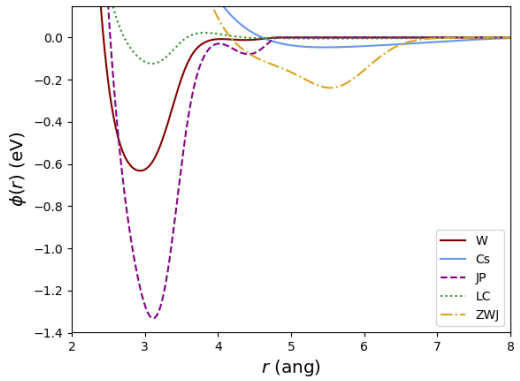

(e) The W-Cs heterogeneous interactions.

Figure 4.3. Potential energy graphs for the Johnson prescription (JP), linear combination (LC), and ZWJ heterogeneous models for the alkali metals on W. The homogeneous potentials for W and the alkalis are also shown, for comparison.

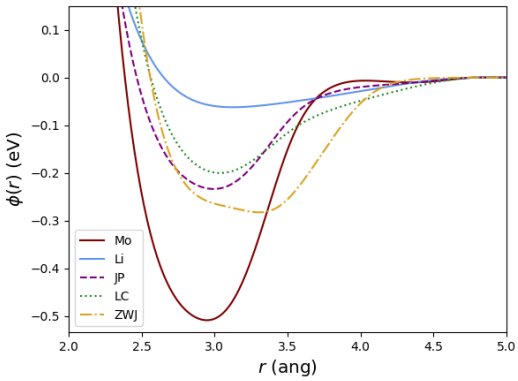

(a) The Mo-Li heterogeneous interactions.

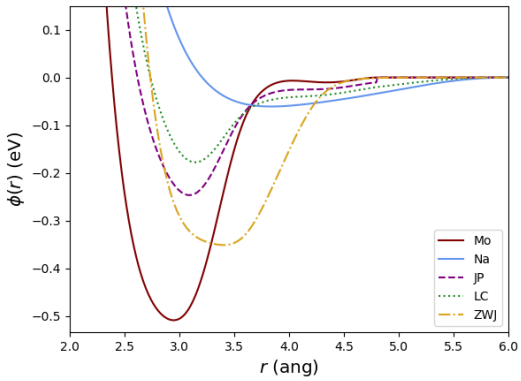

(b) The Mo-Na heterogeneous interactions.

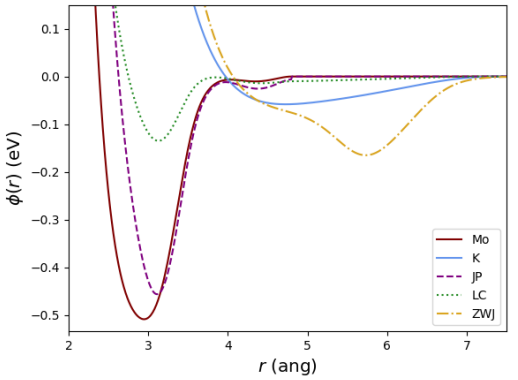

(c) The Mo-K heterogeneous interactions.

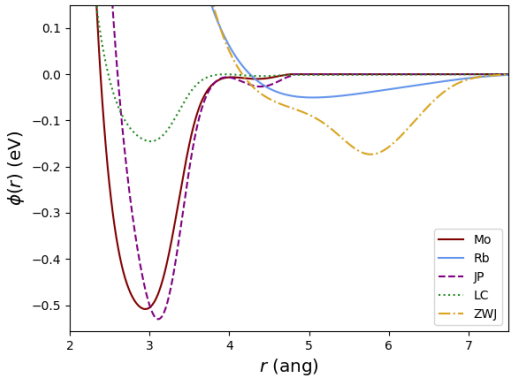

(d) The Mo-Rb heterogeneous interactions.

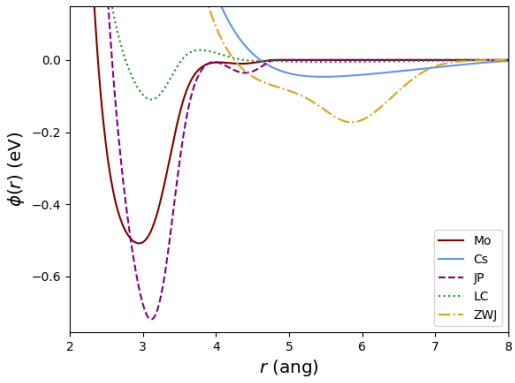

(e) The Mo-Cs heterogeneous interactions.

Figure 4.4. Potential energy graphs for the Johnson prescription (JP), linear combination (LC), and ZWJ heterogeneous models for the alkali metals on Mo. The homogeneous potentials for Mo and the alkalis are also shown, for comparison.

Examining figs. 4.3 and 4.4, the failure of the Johnson prescription becomes much more understandable. In the JP potentials for K, Rb, and Cs on W and Mo, the well depth is far too deep, falling below the substrate well depth. Further, the position of the well tends to stay near the substrate well position. Taking the ZWJ as an example of what an effective model should look like, it appears as though the position of the well for a heterogeneous potential ought to be nearer the alkali well, rather than the substrate well.

This observation also helps explain why the JP does well for Li and Na. Since Li, and to a lesser degree Na, are around the same size as W and Mo, their homogeneous well positions are all around the same spot. Therefore, even if the JP tends to favor a well position closer to W or Mo, the resulting potential still does a reasonable job, since the well position is close to both the alkali and transition metal well potentials. In Johnson's original formulation [72], he was describing alloys of atoms which were roughly the same size, and thus did not run into the problem we see above. Therefore, we can view this results as shedding light on the efficacy of the JP.

For completeness, the parameters for each of the linear combination and ZWJ models we have constructed are shown in Tables 4.8 and 4.9, respectively.

Table 4.8. The parameters for the linear combination interaction of Li, Na, K, Rb, and Cs on W and Mo.

System	α_{Alkali}	$\alpha_{Substrate}$
Mo-Li	1.654	0.198
Mo-Na	0.720	0.417
Mo-K	0.185	0.510
Mo-Rb	0.034	0.349
Mo-Cs	0.131	0.545
W-Li	1.490	0.180
W-Na	0.700	0.347
W-K	0.196	0.457
W-Rb	0.185	0.465
W-Cs	0.116	0.437

Table 4.9. The parameters for the ZWJ interaction of Li, Na, K, Rb, and Cs on W and Mo.

System	r_1 (ang)	K_0 (eV)	$K_1(eV)$	α	δ	κ
Mo-Li	2.808	1.444	1.659	8.137	6.561	0.216
Mo-Na	2.948	1.413	1.664	8.305	6.037	0.214
Mo-K	4.668	1.208	1.267	7.146	6.760	0.215
Mo-Rb	4.721	1.212	1.270	7.100	6.697	0.210
Mo-Cs	4.775	1.213	1.273	7.121	6.67	0.213
W-Li	2.815	1.443	1.667	8.107	6.540	0.215
W-Na	2.974	1.387	1.716	8.058	5.952	0.201
W-K	4.631	1.193	1.301	7.184	6.544	0.171
W-Rb	4.649	1.193	1.301	7.192	6.531	0.171
W-Cs	4.712	1.201	1.298	7.248	6.558	0.172

4.5. Conclusions

There are two main results from our model-construction process. First, it is clear that the ZWJ model is the best performer for all the systems we wish to study. As discussed earlier, this should not come as a surprise, due to the large number of free parameters in the ZWJ model. Although the linear combination approach does a reasonably good job describing vibrational frequencies, it systematically failed to describe the binding energy of the alkali-metal/transition-metal systems.

Further, when analyzing the models of a full monolayer of Li on Mo, the ZWJ still did the best job. Because the models were not fit to the full monolayer data, this suggests that the ZWJ approach can be extended to different coverages and surfaces, and still give dependable results. Therefore, we choose to use the ZWJ model in our examination of different interface systems in Chapter Five.

The second, perhaps surprising, result is the failure of the Johnson prescription. Since the JP is widely used, it is interesting to see under what regimes it fails. Our analysis suggests that the JP can only accurately be used to model the interaction between two different metals when the metals are roughly the same size. This discovery should help guide future investigations of alloy systems.

CHAPTER 5
RESULTS

Chapters two through four of this thesis have been dedicated to building the tools necessary to analyze the alkali-metal/transition-metal interface. In this chapter, we use those tools to calculate the vibrational properties of a number of systems. These systems consist of substrates of W or Mo, oriented on their (110), (100), and (111) surfaces. On each of these surfaces, we adsorb a layer of alkali metal in increasing coverage. The intent of examining multiple coverages is to probe the effect of increasing alkali atom density on vibrational properties.

5.1. (110) Surface

On the (110) surface of W and Mo, we examine Li at coverages of a sixth, a quarter, a third, and a full monolayer. These coverages of Li have been observed on W (110) by [10], and on Mo (110) by [11]. The three fractional coverages are shown in Figure 5.1, with unit cells outlined in red. The Brillouin zones for each of these systems is shown in Figure 5.2.

We choose to place the Li atoms on the long bridge site, in line with the calculations of Vella *et. al* [78]. These calculations suggest that the binding energy is minimized when the adsorbed atoms are placed on the long bridge site.

When calculating the densities of states and Debye temperatures, we use the IBZ for each coverage. For the full monolayer, we use 88,746 IBZ points. For a third monolayer, we use 16,512 IBZ points. For the quarter monolayer, we use 22,262 IBZ points. Finally, for the sixth monolayer, we use 5,620 IBZ points. The exact number of points used for each IBZ is a result of the size and shape of the IBZ. Each mesh has the same k-space density, so the IBZs which are smaller (i.e., the sixth monolayer IBZ) end up with fewer points. Although the less dense coverages use a smaller number of points, the total number of modes calculated for each coverage remains similar. This is because the number of modes per IBZ points scales linearly with the number of atoms per unit cell. The sixth monolayer has six times as many atoms per

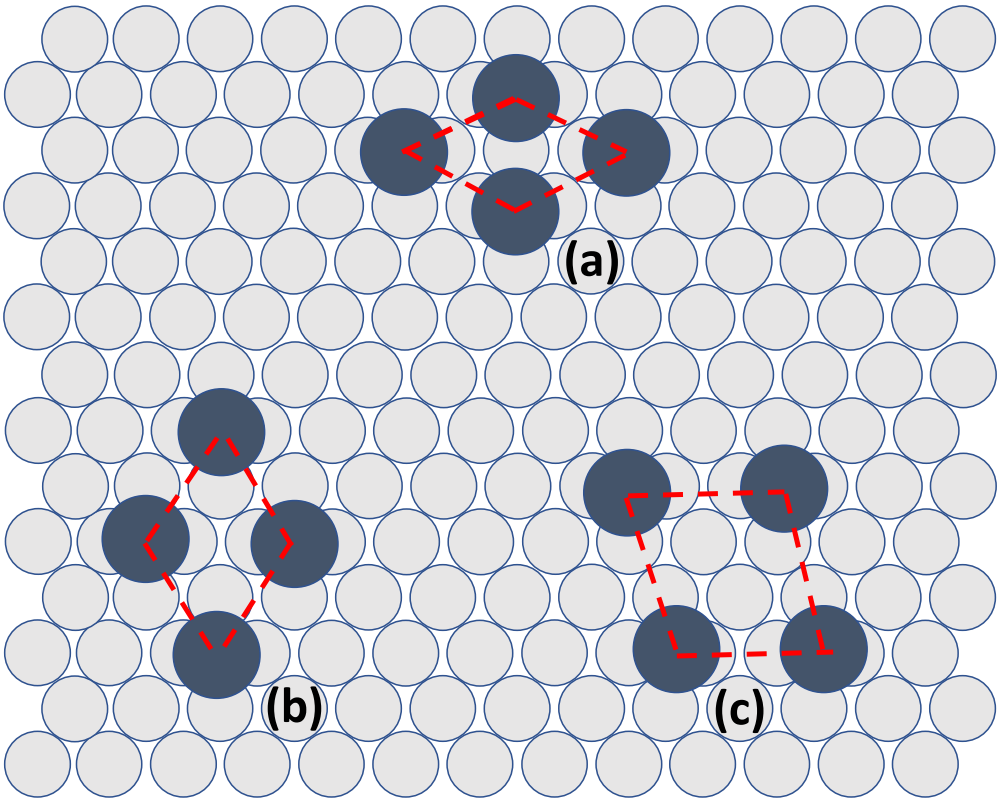

Figure 5.1. Unit cells for a (a) third, (b) quarter, and (c) sixth monolayer on the (110) surface.

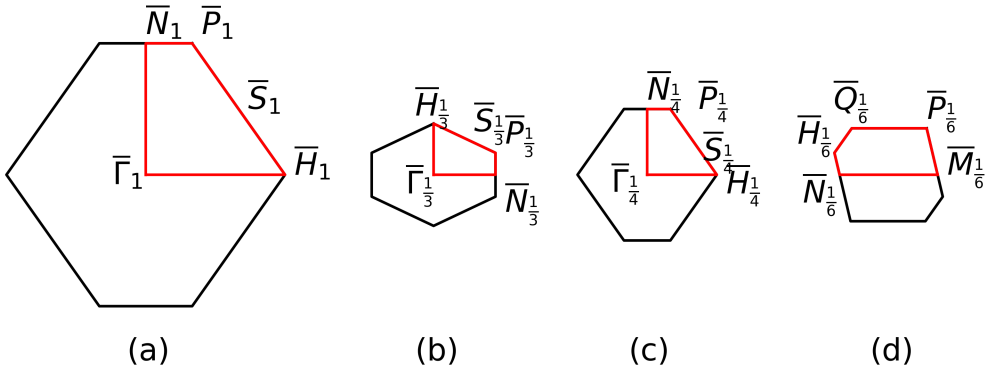

Figure 5.2. The Brillouin zones for a (a) full, (b) third, (c) quarter, and (d) sixth monolayer on the (110) surface.

unit cell as the full monolayer, so that the total number of modes calculated for each system is closer than it would appear.

We use a 51 layer slab of W or Mo for the substrate of the (110) system. We have found that this slab thickness gives vibrational results for the center layer which are nearly identical to the bulk vibrations of W and Mo. This is important, as we expect the atoms in the center of the slab to behave the same as bulk atoms.

5.1.1. W-Li Systems

We begin by looking at a clean slab of W. This allows us to see how vibrational properties change as we add more and more adsorbate atoms. Figures 5.3, 5.4 and 5.5 show the layer resolved dispersion curves and densities of states of the (110) surface of W. The sixth, quarter, third, and full monolayer dispersion curves and densities of states are shown in Figs. 5.6, 5.7, 5.8, 5.9, 5.10, 5.11, 5.12, 5.13, 5.14, 5.15, 5.16, 5.17.

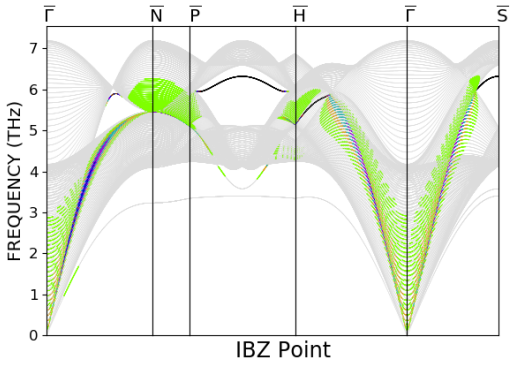

(a) First layer longitudinal polarization

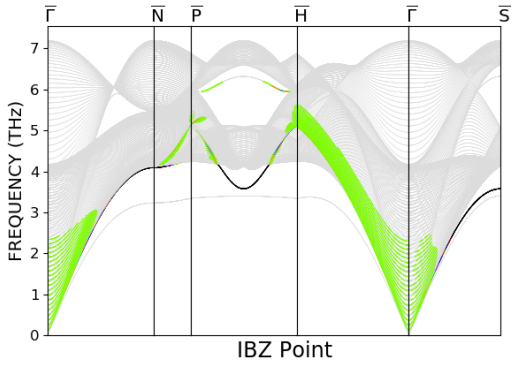

(b) First layer shear horizontal polarization

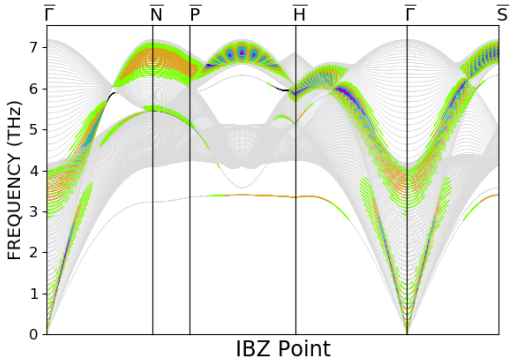

(c) Second layer longitudinal polarization

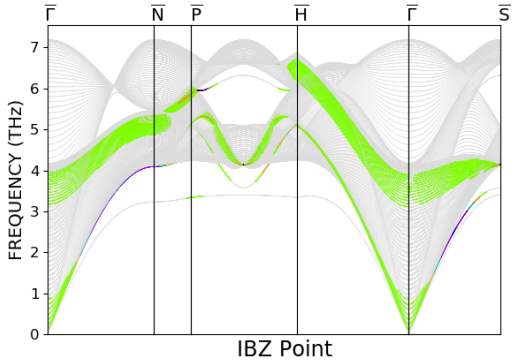

(d) Second layer shear horizontal polarization

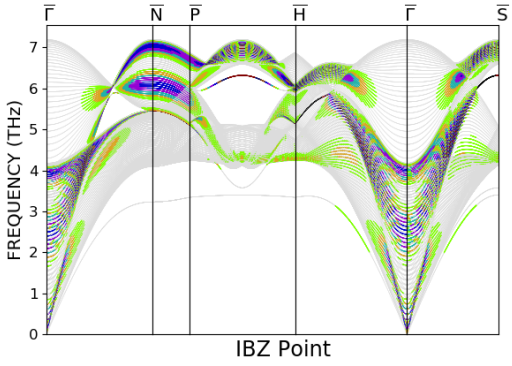

(e) Third layer longitudinal polarization

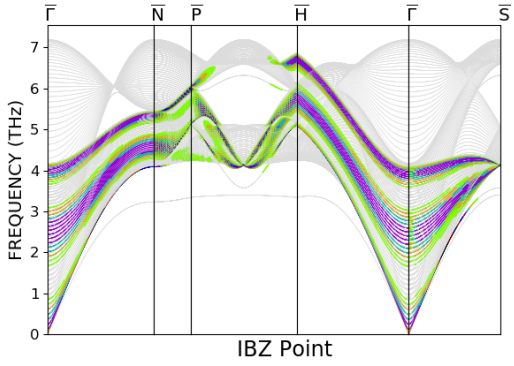

(f) Third layer shear horizontal polarization

Figure 5.3. Dispersion curves for a clean slab of the (110) surface of W. Longitudinal (shear horizontal) projections are shown on the left (right).

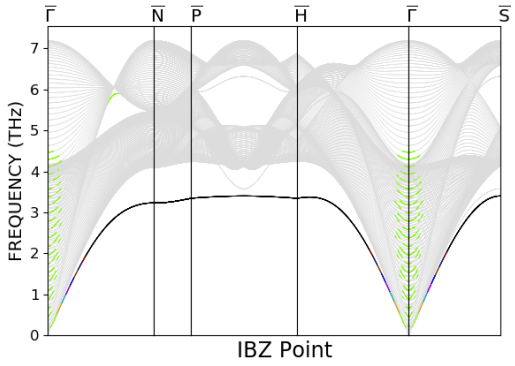

(a) First layer shear vertical polarization

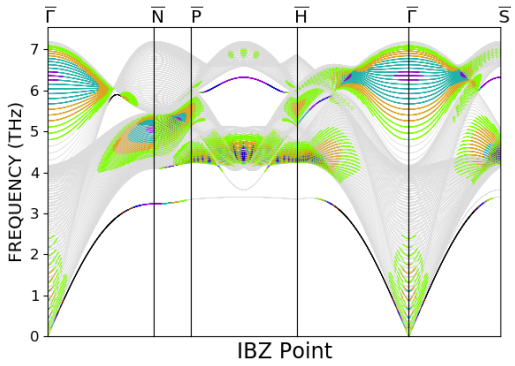

(b) Second layer shear vertical polarization

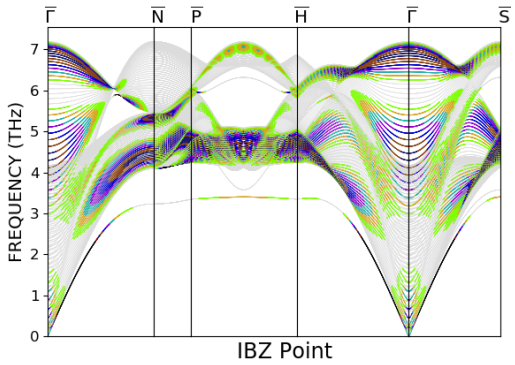

(c) Third layer shear vertical polarization

Figure 5.4. Dispersion curves for a clean slab of the (110) surface of W projected in the shear vertical direction.

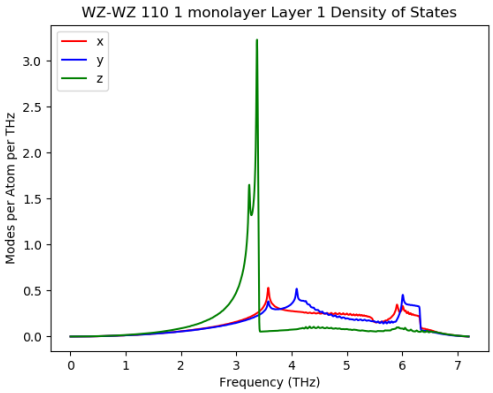

(a) Fist layer density of states

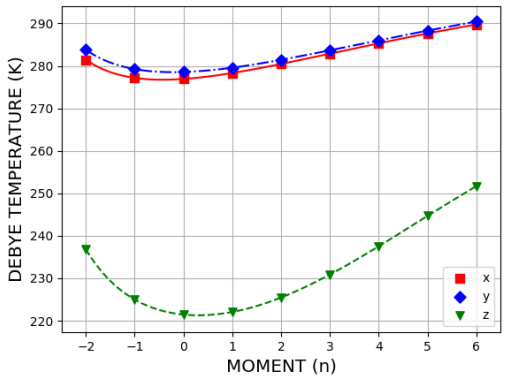

(b) Fist layer Debye tempteratures

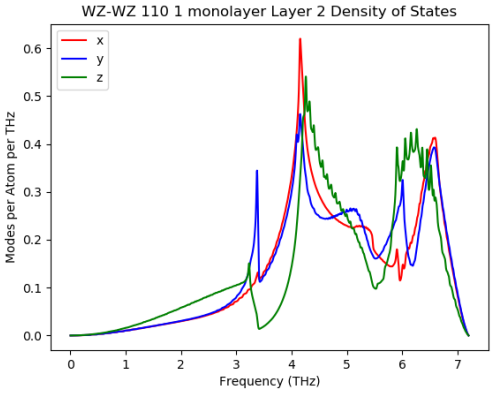

(c) Second layer density of states

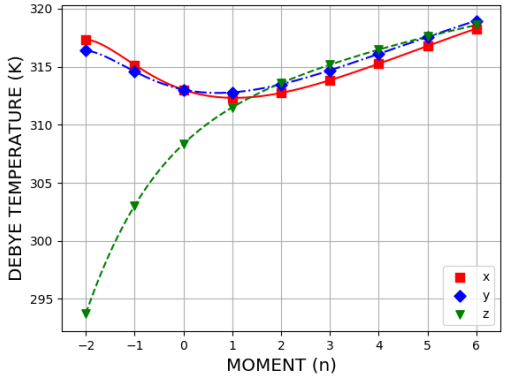

(d) Second layer Debye tempteratures

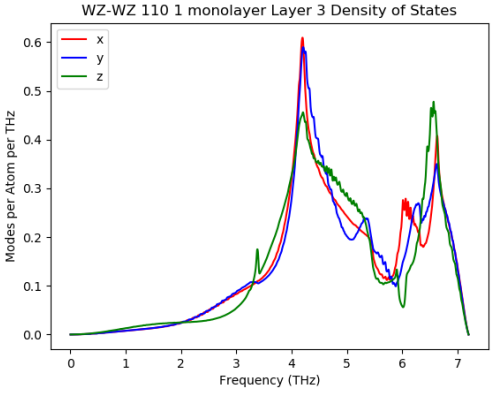

(e) Third layer density of states

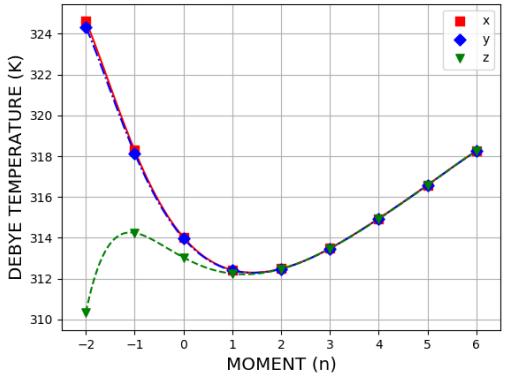

(f) Third layer Debye tempteratures

Figure 5.5. Densities of states and Debye temperatures for a clean slab of the (110) surface of W, projected on to the x, y, and z directions.

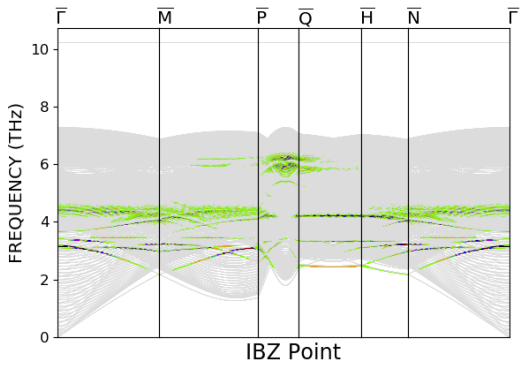

(a) Alkali layer longitudinal polarization

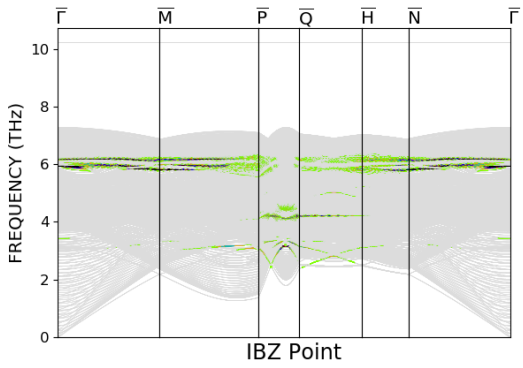

(b) Alkali layer shear horizontal polarization

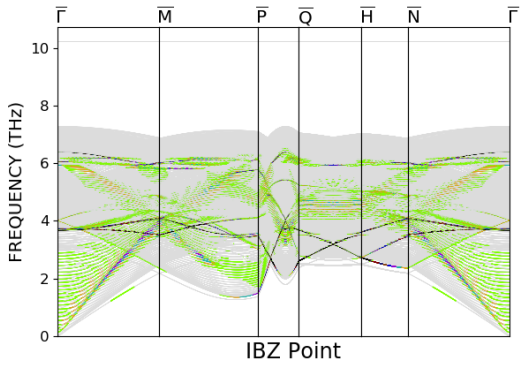

(c) First substrate layer longitudinal polarization

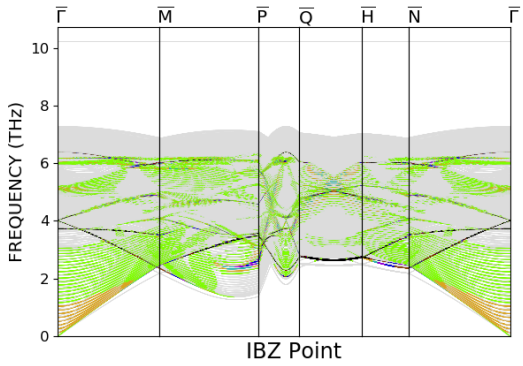

(d) First substrate layer shear horizontal polarization

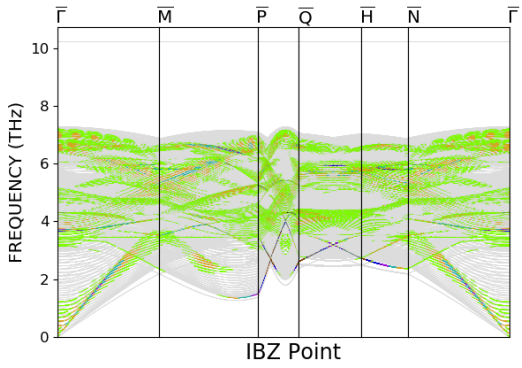

(e) Second substrate layer longitudinal polarization

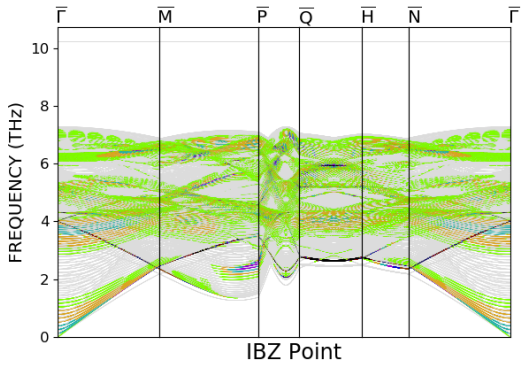

(f) Second substrate layer shear horizontal polarization

Figure 5.6. Dispersion curves for a sixth monolayer of Li on the 110 surface of W. Longitudinal (shear horizontal) projections are shown on the left (right).

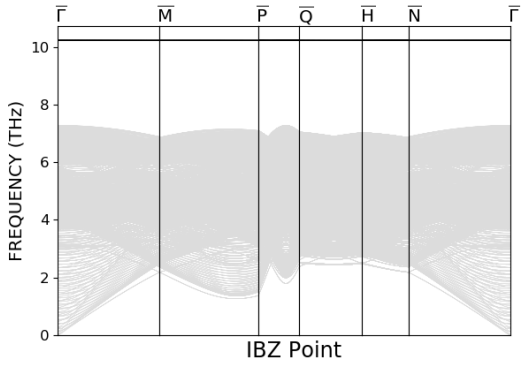

(a) Alkali layer shear vertical polarization

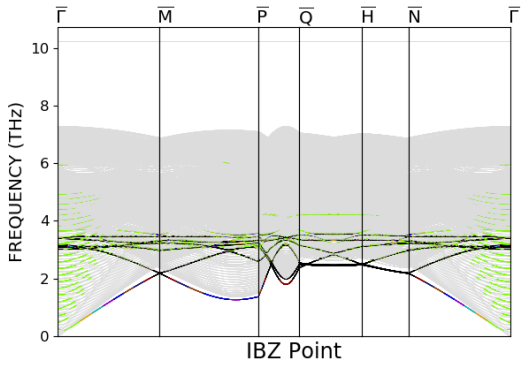

(b) First substrate layer shear vertical polarization

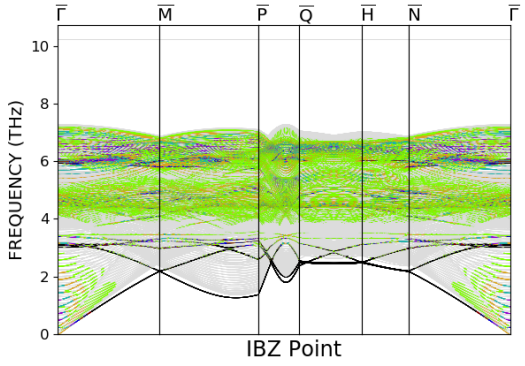

(c) Second substrate layer shear vertical polarization

Figure 5.7. Dispersion curves for a sixth monolayer of Li on the 110 surface of W projected in the shear vertical direction.

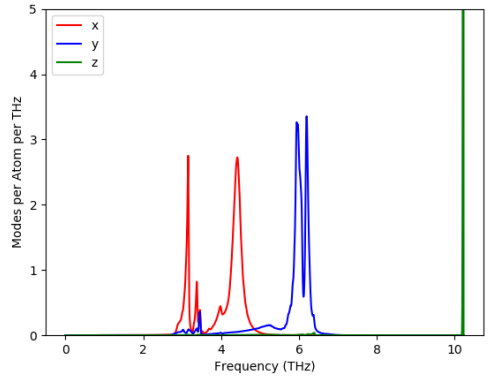

(a) Alkali layer density of states

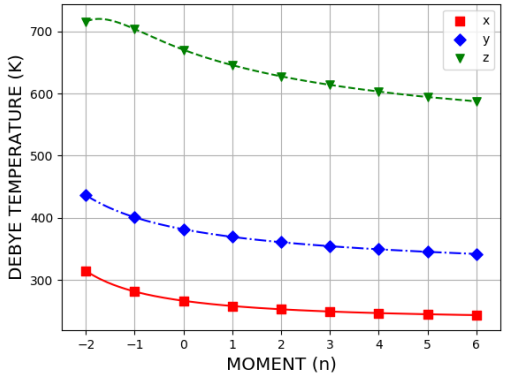

(b) Alkali layer Debye tempteratures

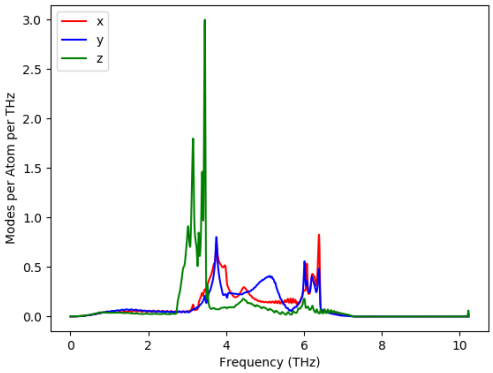

(c) First substrate layer density of states

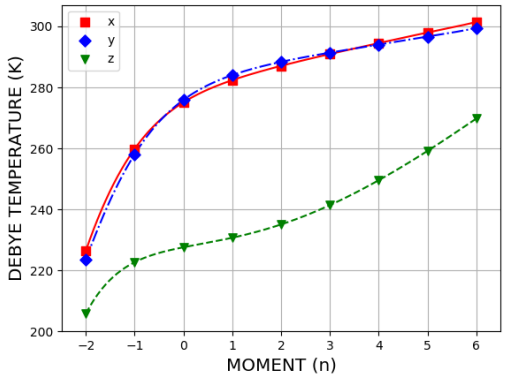

(d) First substrate layer Debye tempteratures

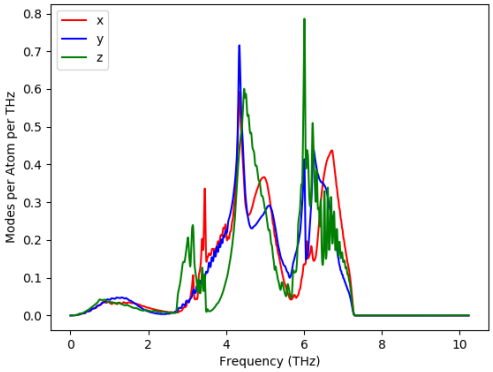

(e) Second substrate layer density of states

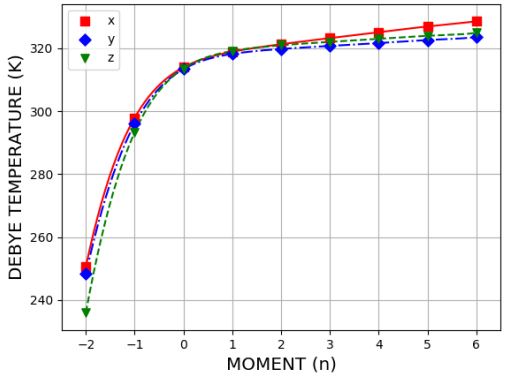

(f) Second substrate layer Debye tempteratures

Figure 5.8. Densities of states and Debye temperatures for a sixth monolayer of Li on the 110 surface of W, projected on to the x, y, and z directions.

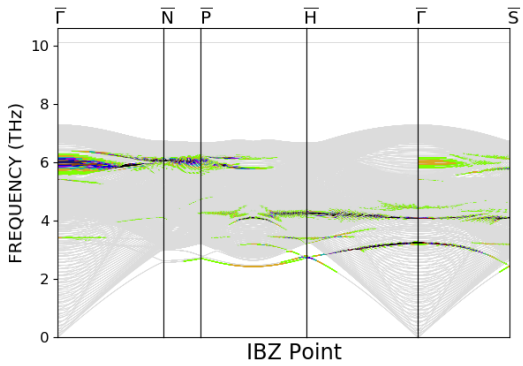

(a) Alkali layer longitudinal polarization

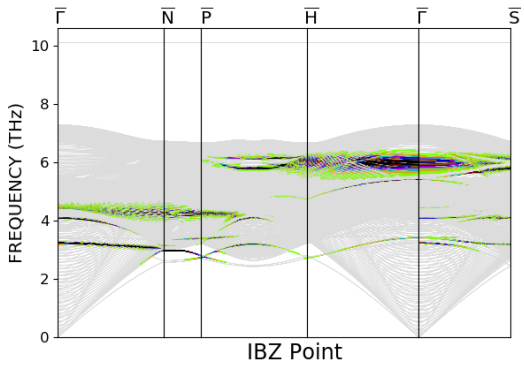

(b) Alkali layer shear horizontal polarization

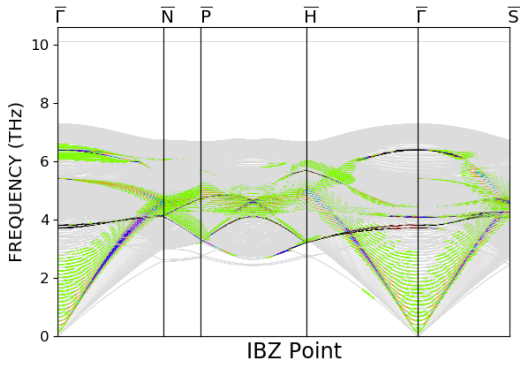

(c) First substrate layer longitudinal polarization

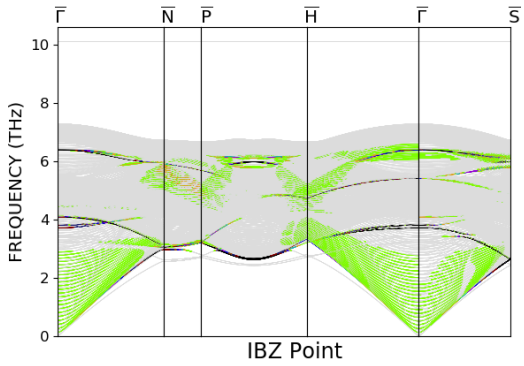

(d) First substrate layer shear horizontal polarization

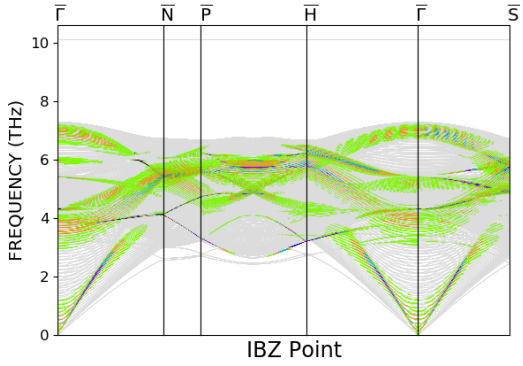

(e) Second substrate layer longitudinal polarization

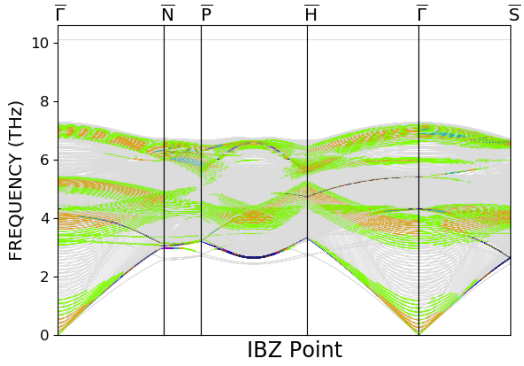

(f) Second substrate layer shear horizontal polarization

Figure 5.9. Dispersion curves for a quarter monolayer of Li on the 110 surface of W. Longitudinal (shear horizontal) projections are shown on the left (right).

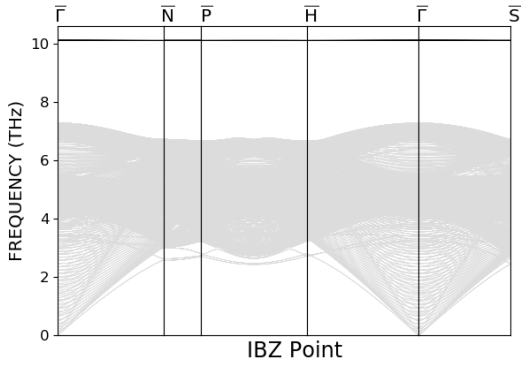

(a) Alkali layer shear vertical polarization

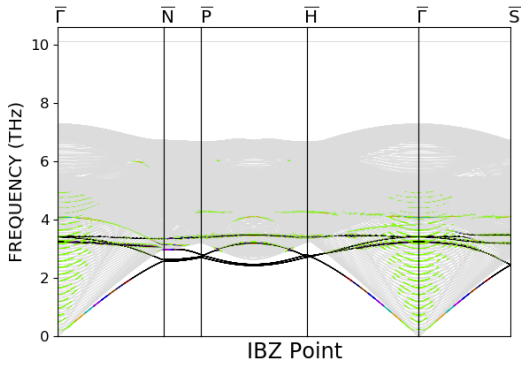

(b) First substrate layer shear vertical polarization

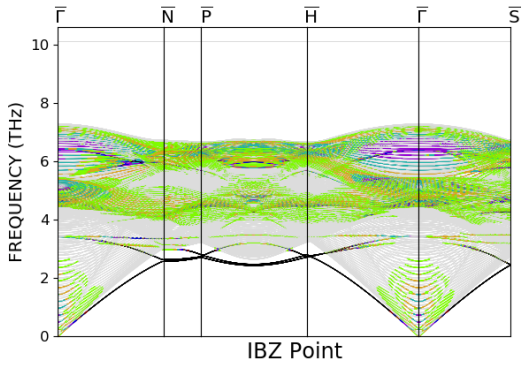

(c) Second substrate layer shear vertical polarization

Figure 5.10. Dispersion curves for a quarter monolayer of Li on the 110 surface of W projected in the shear vertical direction.

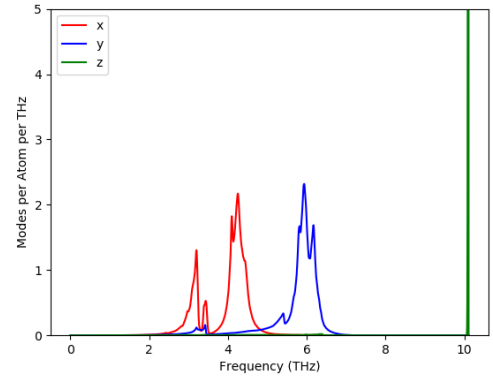

(a) Alkali layer density of states

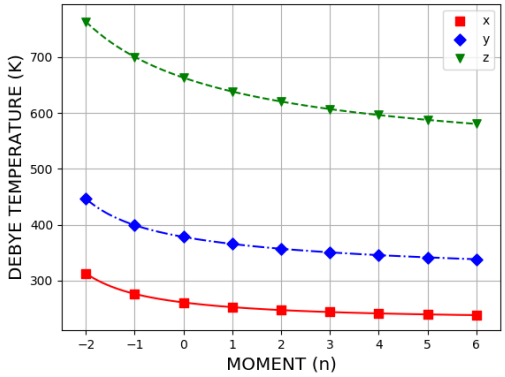

(b) Alkali layer Debye tempteratures

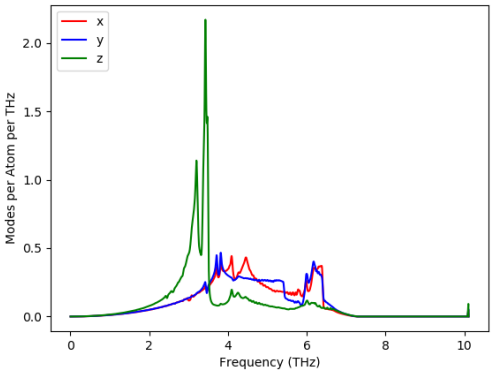

(c) First substrate layer density of states

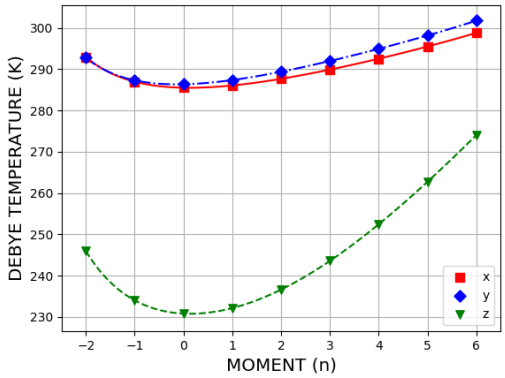

(d) First substrate layer Debye tempteratures

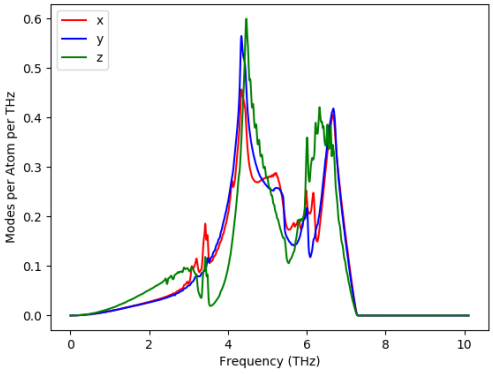

(e) Second substrate layer density of states

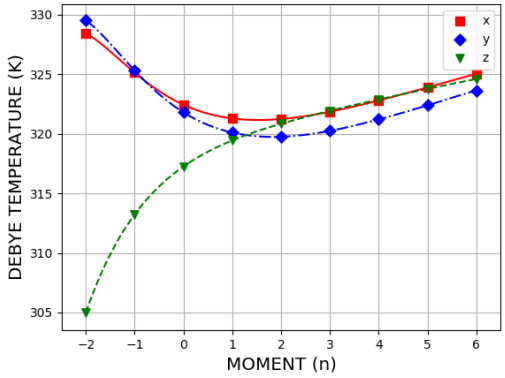

(f) Second substrate layer Debye tempteratures

Figure 5.11. Densities of states and Debye temperatures for a quarter monolayer of Li on the 110 surface of W, projected on to the x, y, and z directions.

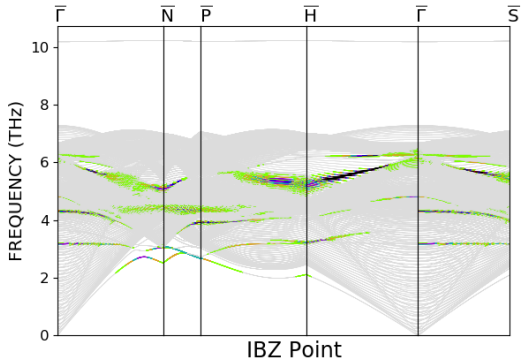

(a) Alkali layer longitudinal polarization

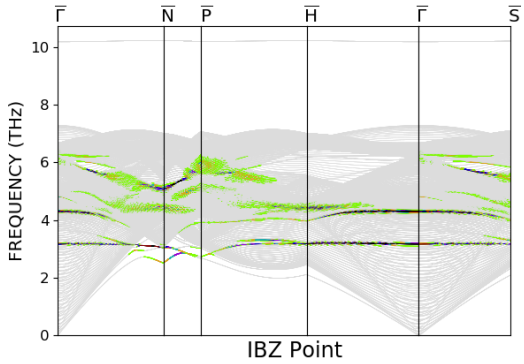

(b) Alkali layer shear horizontal polarization

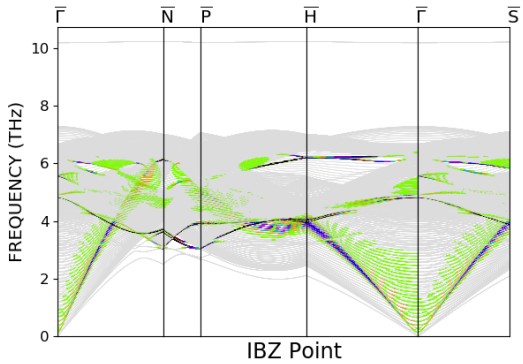

(c) First substrate layer longitudinal polarization

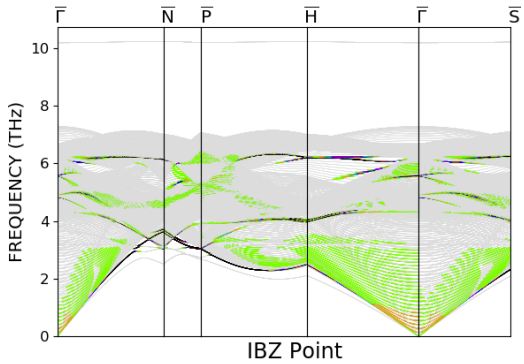

(d) First substrate layer shear horizontal polarization

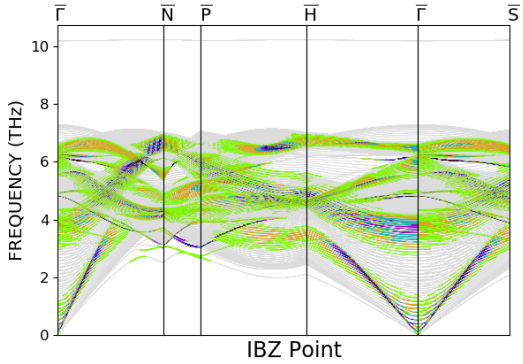

(e) Second substrate layer longitudinal polarization

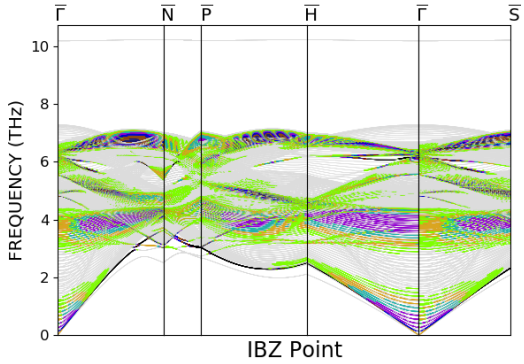

(f) Second substrate layer shear horizontal polarization

Figure 5.12. Dispersion curves for a third monolayer of Li on the 110 surface of W. Longitudinal (shear horizontal) projections are shown on the left (right).

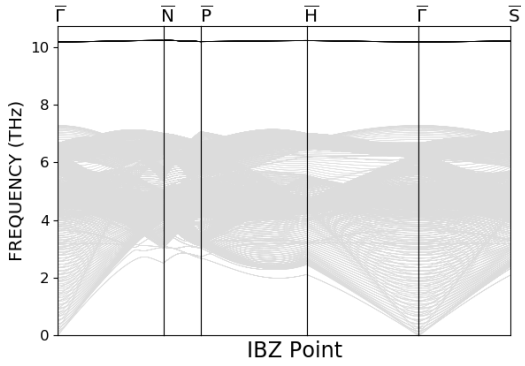

(a) Alkali layer shear vertical polarization

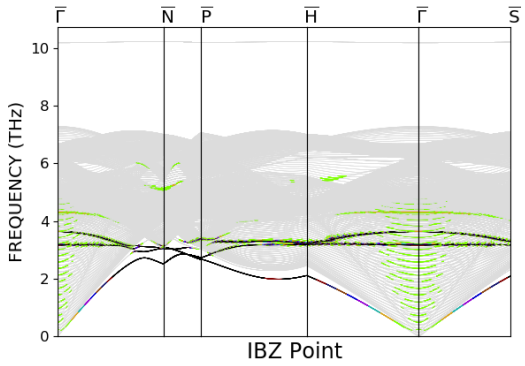

(b) First substrate layer shear vertical polarization

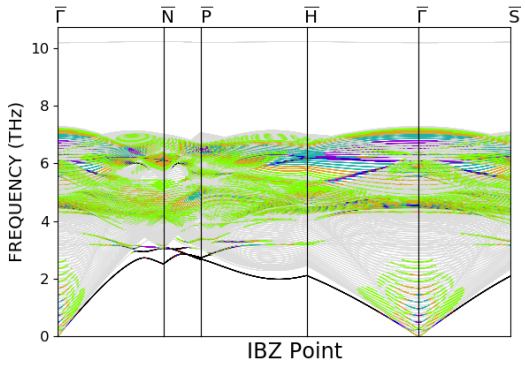

(c) Second substrate layer shear vertical polarization

Figure 5.13. Dispersion curves for a third monolayer of Li on the 110 surface of W projected in the shear vertical direction.

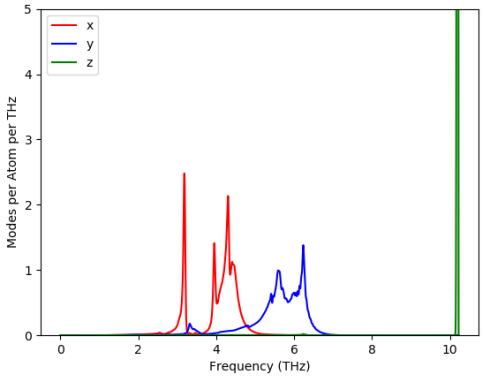

(a) Alkali layer density of states

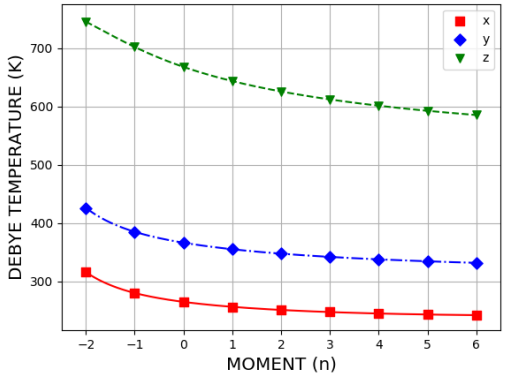

(b) Alkali layer Debye tempteratures

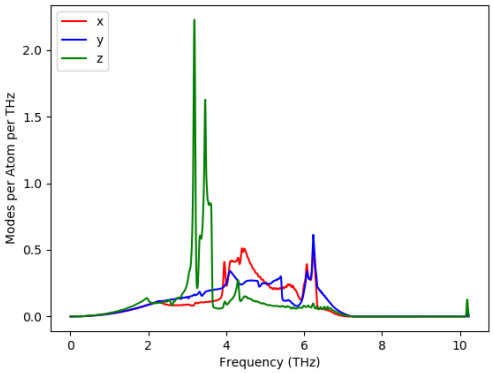

(c) First substrate layer density of states

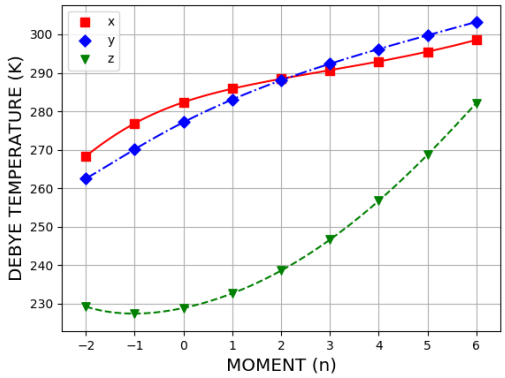

(d) First substrate layer Debye tempteratures

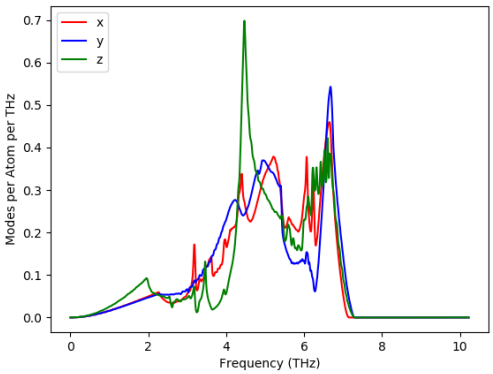

(e) Second substrate layer density of states

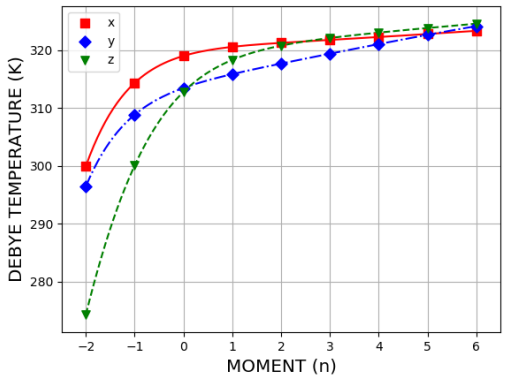

(f) Second substrate layer Debye tempteratures

Figure 5.14. Densities of states and Debye temperatures for a third monolayer of Li on the 110 surface of W, projected on to the x, y, and z directions.

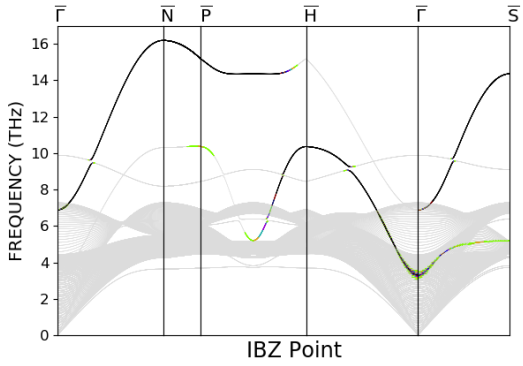

(a) Alkali layer longitudinal polarization

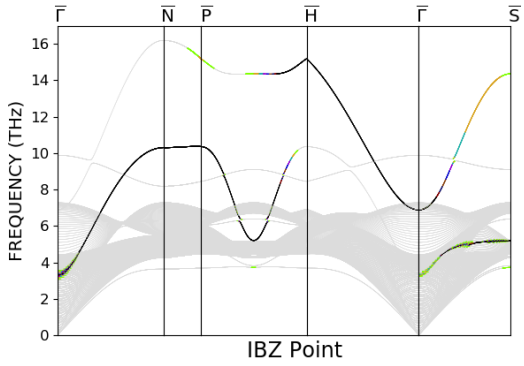

(b) Alkali layer shear horizontal polarization

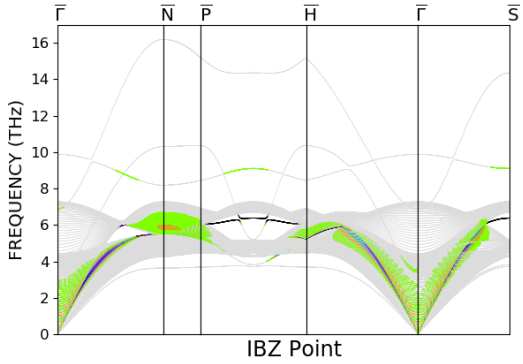

(c) First substrate layer longitudinal polarization

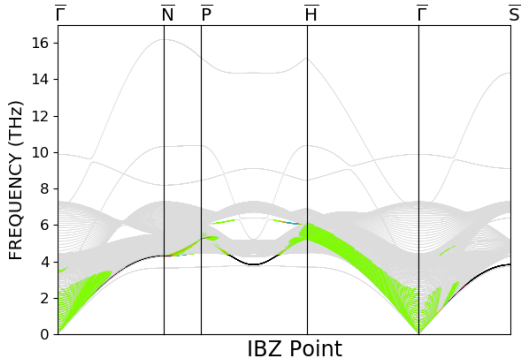

(d) First substrate layer shear horizontal polarization

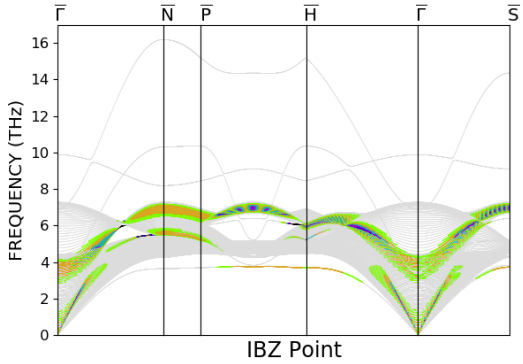

(e) Second substrate layer longitudinal polarization

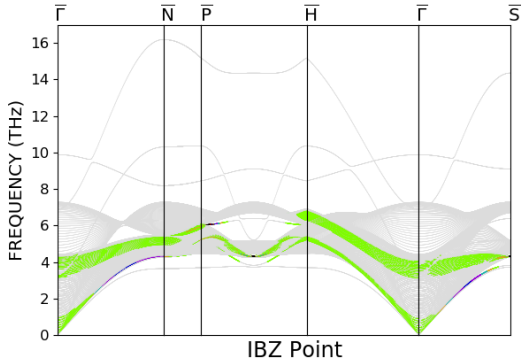

(f) Second substrate layer shear horizontal polarization

Figure 5.15. Dispersion curves for a full monolayer of Li on the 110 surface of W. Longitudinal (shear horizontal) projections are shown on the left (right).

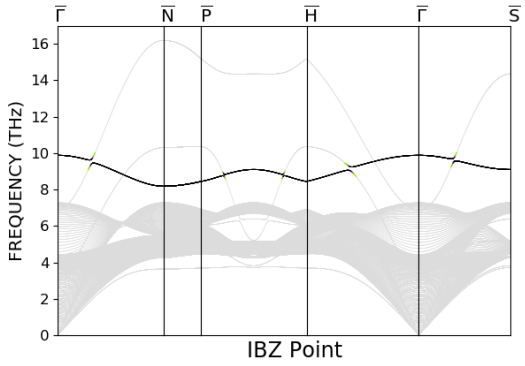

(a) Alkali layer shear vertical polarization

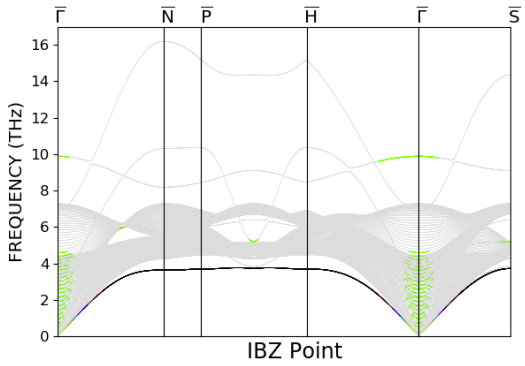

(b) First substrate layer shear vertical polarization

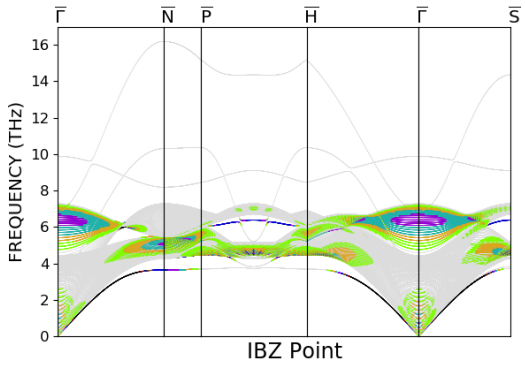

(c) Second substrate layer shear vertical polarization

Figure 5.16. Dispersion curves for a full monolayer of Li on the 110 surface of W projected in the shear vertical direction.

We see significant dispersion in the in-plane motion of the Li layer. This indicates that there is strong interaction between the Li atoms, which we should expect. Because the lattice constant of W is somewhat smaller than the bulk lattice constant of Li, a full monolayer of Li would put the Li atoms closer to each other than they are in bulk Li, leading to the strong dispersion we see.

Alternatively, we see little dispersion in the shear vertical projections of the Li atoms when compared to the in-plane motion. The vertical motion of the Li atoms is dominated by the W-Li interaction, rather than the Li-Li interaction, so this makes sense. We can get a full picture of the allowed frequencies by examining the layer and direction resolved densities of state, shown in Figure 5.17.

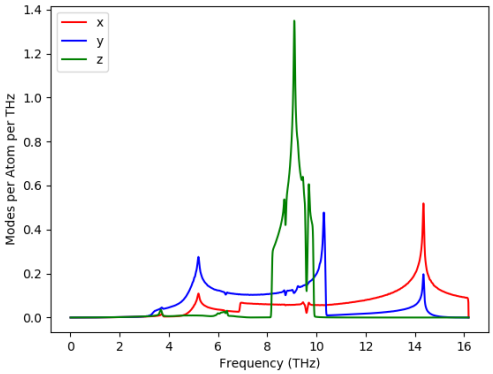

(a) Alkali layer density of states

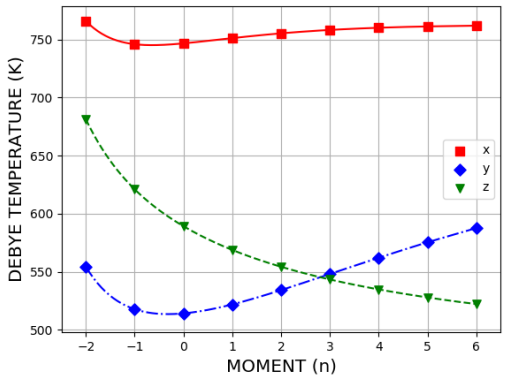

(b) Alkali layer Debye tempteratures

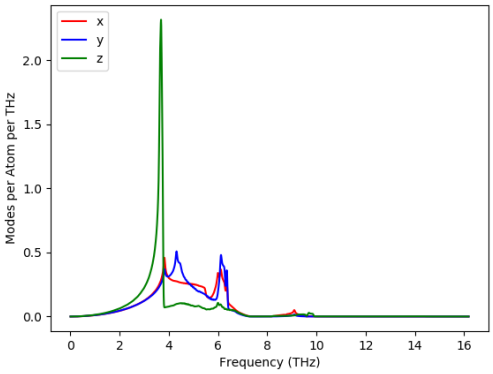

(c) First substrate layer density of states

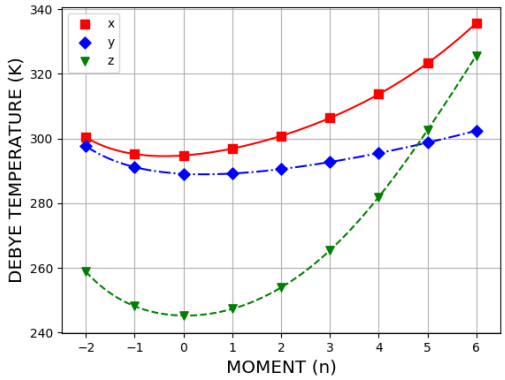

(d) First substrate layer Debye tempteratures

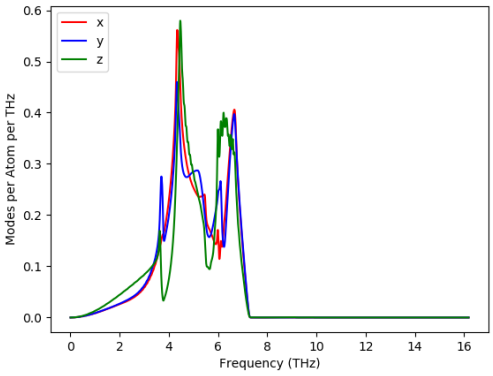

(e) Second substrate layer density of states

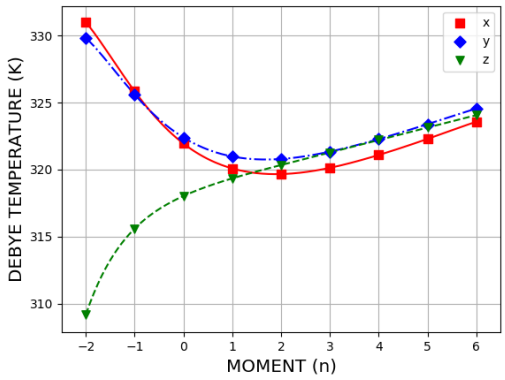

(f) Second substrate layer Debye tempteratures

Figure 5.17. Densities of states and Debye temperatures for a full monolayer of Li on the 110 surface of W, projected on to the x, y, and z directions.

We note that by comparing the dispersion curves of a sixth, quarter, and third monolayer (Figs. 5.6, 5.9, and 5.12), we can see a slight broadening of the modes projected on to the alkali layer. This shows that, as we increase the coverage, the Li-Li interactions become more and more prevalent.

5.1.2. Mo-Li Systems

We repeat the same analysis for Li absorbed on the (110) surface of Mo, once again beginning with a clean slab of Mo with 51 layers. The layer resolved dispersion curves for the in-plane and shear horizontal projections, and the layer resolved densities of states for the clean surface, sixth, quarter, third, and full monolayer are shown in Figs. 5.18, 5.19, 5.20, 5.21, 5.22, 5.23, 5.24, 5.25, 5.26, 5.27, 5.28, 5.29, 5.30, 5.31, 5.32.

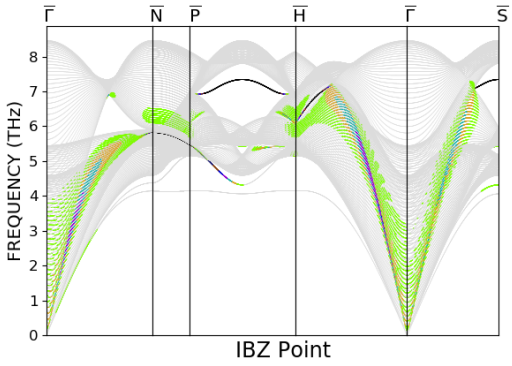

(a) First layer longitudinal polarization

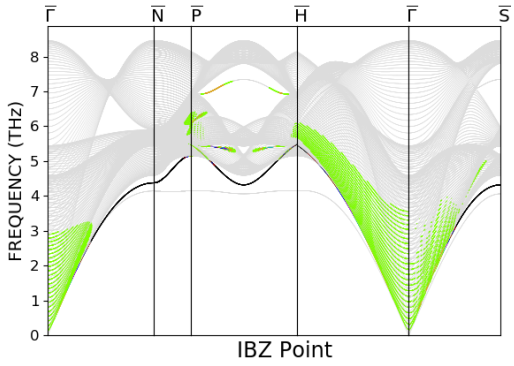

(b) First layer shear horizontal polarization

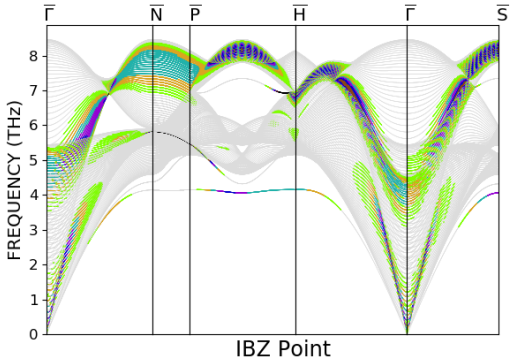

(c) Second layer longitudinal polarization

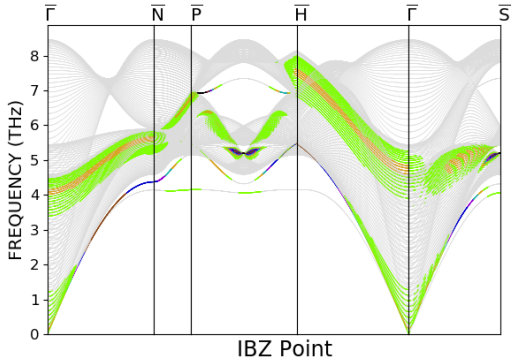

(d) Second layer shear horizontal polarization

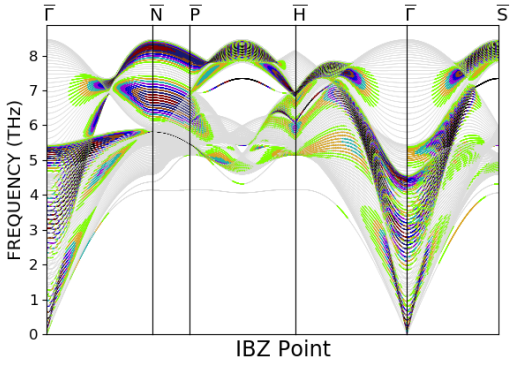

(e) Third layer longitudinal polarization

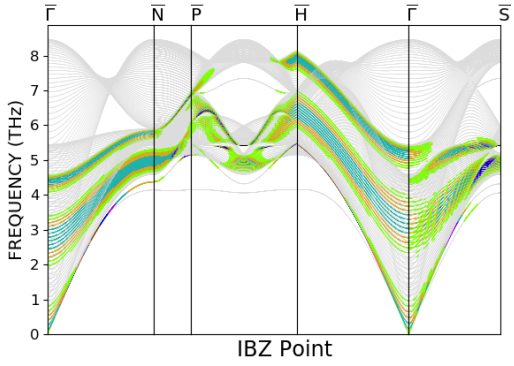

(f) Third layer shear horizontal polarization

Figure 5.18. Dispersion curves for a clean slab of the (110) surface of Mo. Longitudinal (shear horizontal) projections are shown on the left (right).

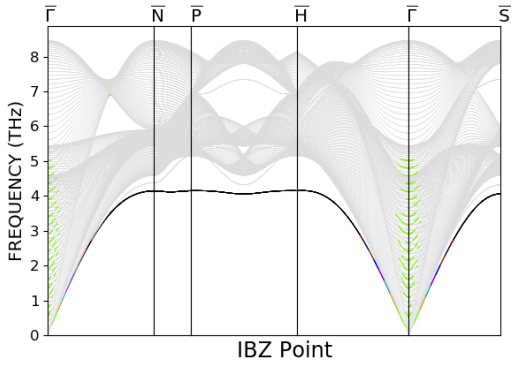

(a) First layer shear vertical polarization

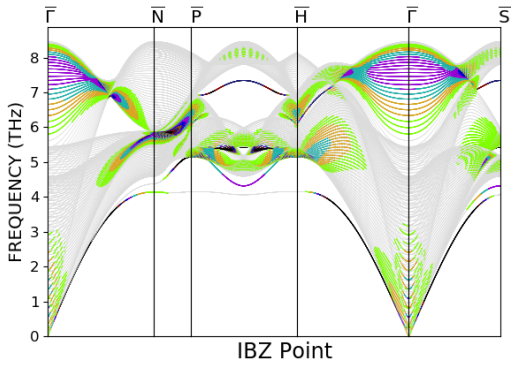

(b) Second layer shear vertical polarization

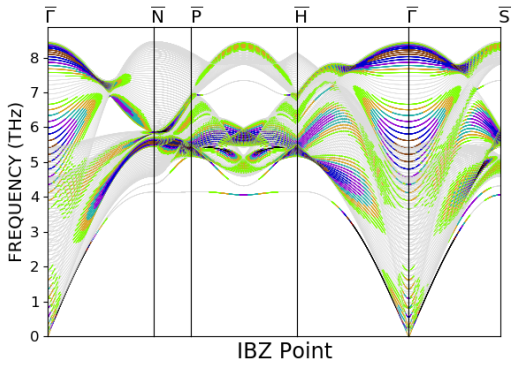

(c) Third layer shear vertical polarization

Figure 5.19. Dispersion curves for a clean slab of the (110) surface of Mo projected in the shear vertical direction.

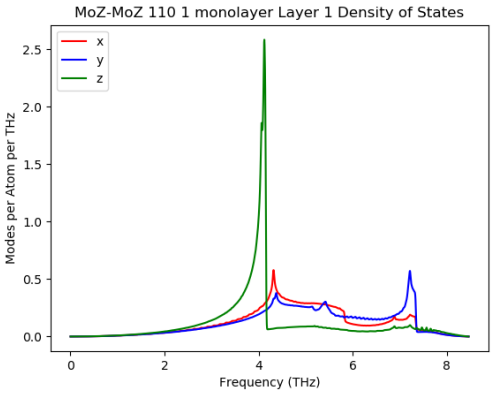

(a) Fist layer density of states

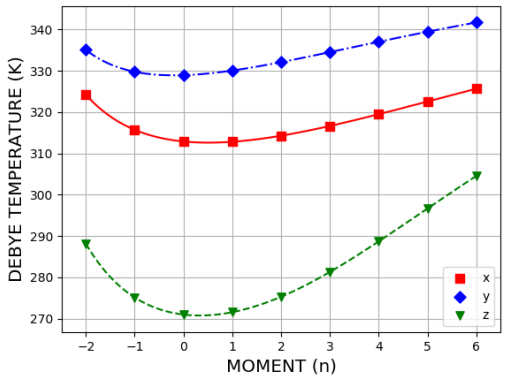

(b) Fist layer Debye tempteratures

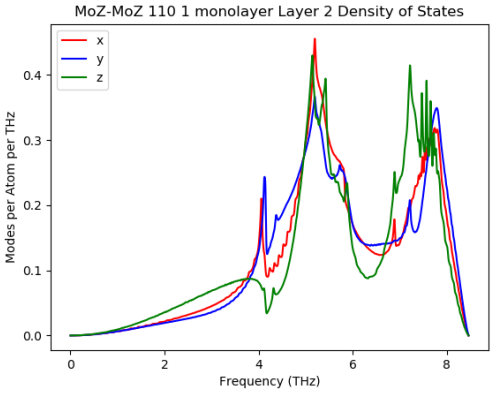

(c) Second layer density of states

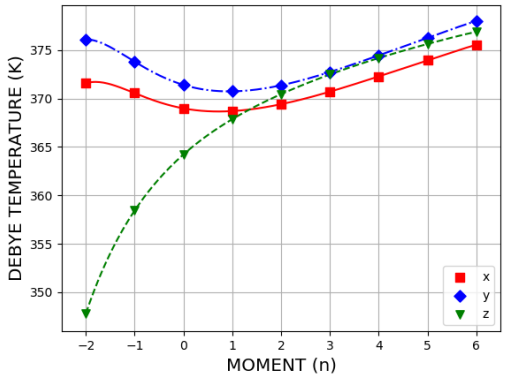

(d) Second layer Debye tempteratures

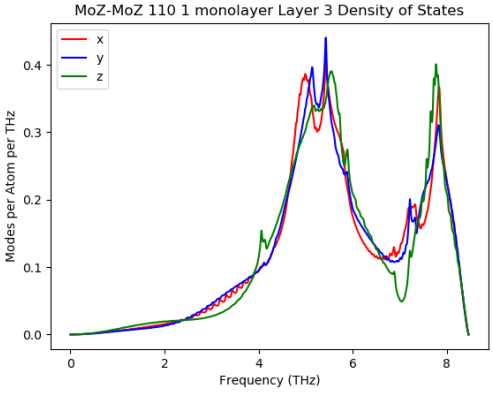

(e) Third layer density of states

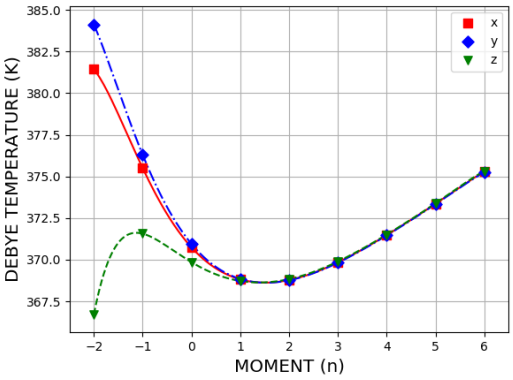

(f) Third layer Debye tempteratures

Figure 5.20. Densities of states and Debye temperatures for a clean slab of the (110) surface of Mo, projected on to the x, y, and z directions.

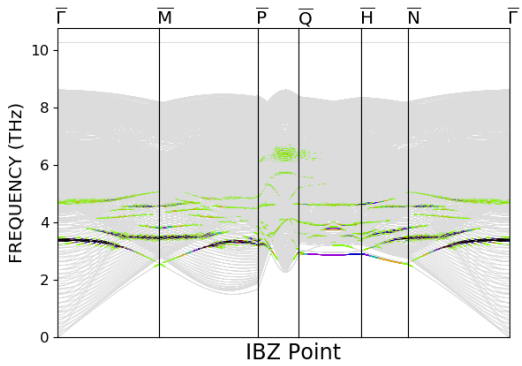

(a) Alkali layer longitudinal polarization

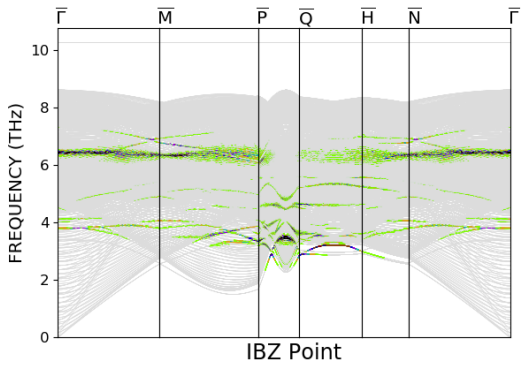

(b) Alkali layer shear horizontal polarization

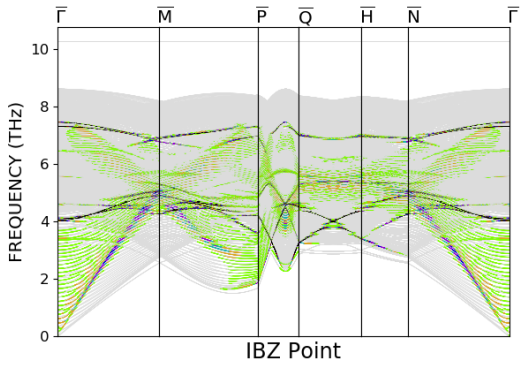

(c) First substrate layer longitudinal polarization

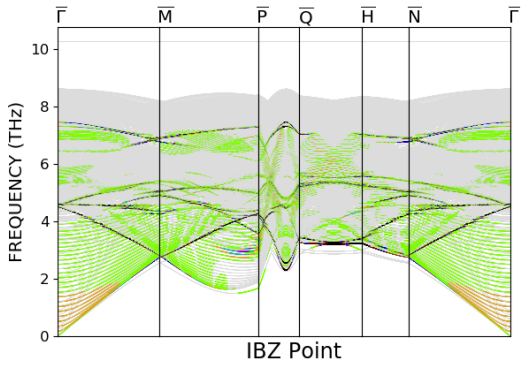

(d) First substrate layer shear horizontal polarization

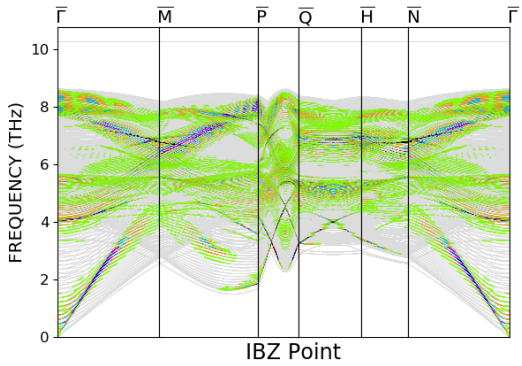

(e) Second substrate layer longitudinal polarization

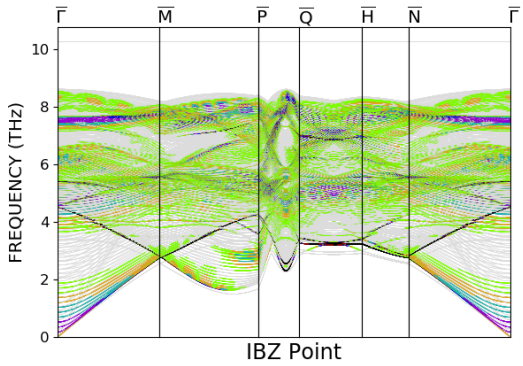

(f) Second substrate layer shear horizontal polarization

Figure 5.21. Dispersion curves for a sixth monolayer of Li on the 110 surface of Mo. Longitudinal (shear horizontal) projections are shown on the left (right).

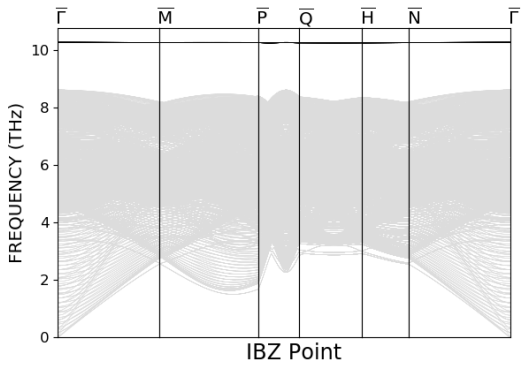

(a) Alkali layer shear vertical polarization

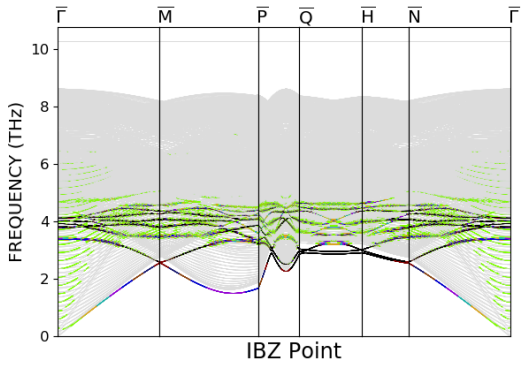

(b) First substrate layer shear vertical polarization

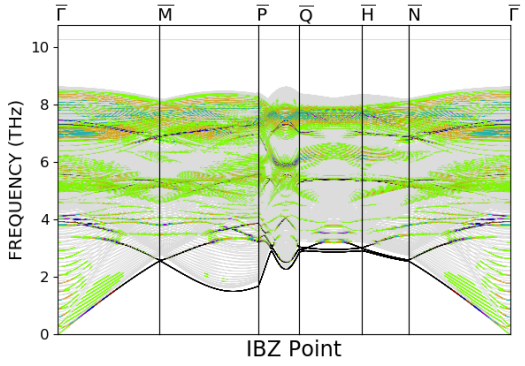

(c) Second substrate layer shear vertical polarization

Figure 5.22. Dispersion curves for a sixth monolayer of Li on the 110 surface of Mo projected in the shear vertical direction.

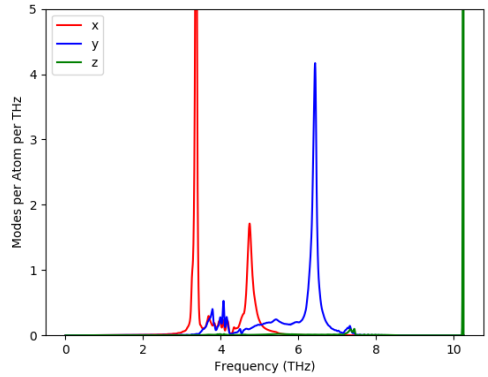

(a) Alkali layer density of states

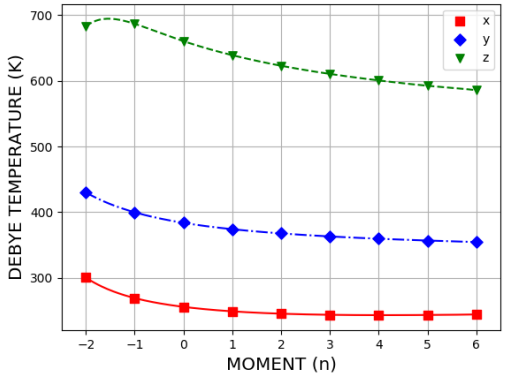

(b) Alkali layer Debye tempteratures

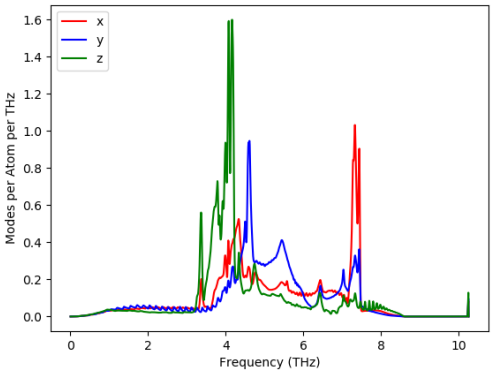

(c) First substrate layer density of states

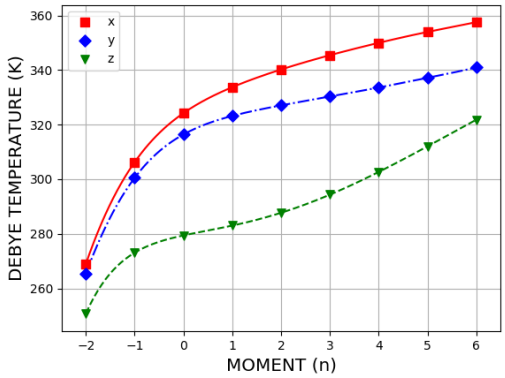

(d) First substrate layer Debye tempteratures

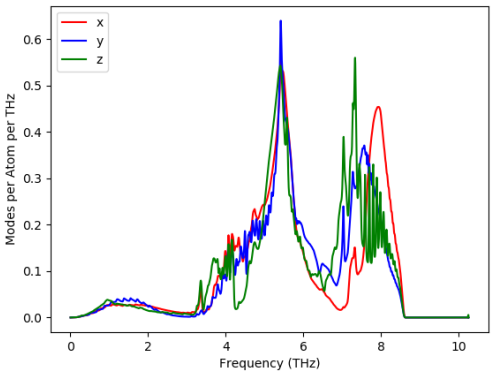

(e) Second substrate layer density of states

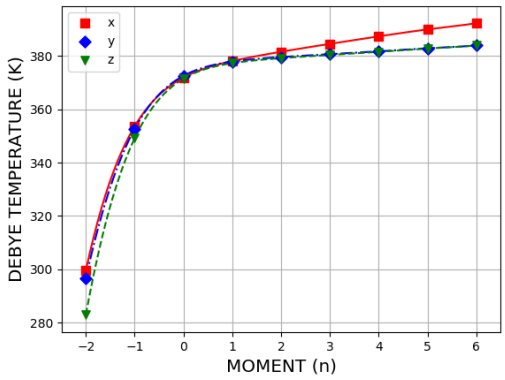

(f) Second substrate layer Debye tempteratures

Figure 5.23. Densities of states and Debye temperatures for a sixth monolayer of Li on the 110 surface of Mo, projected on to the x, y, and z directions.

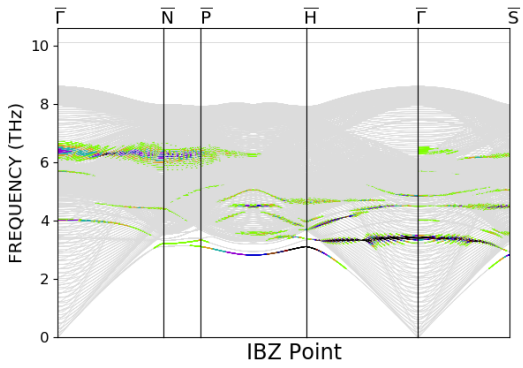

(a) Alkali layer longitudinal polarization

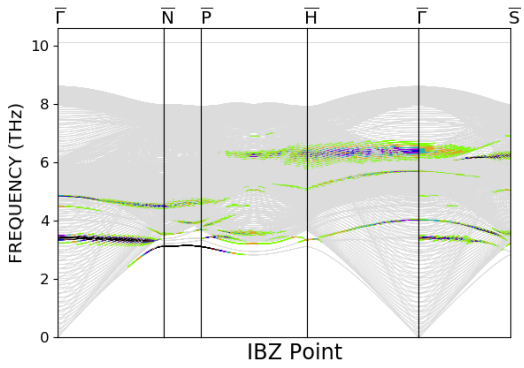

(b) Alkali layer shear horizontal polarization

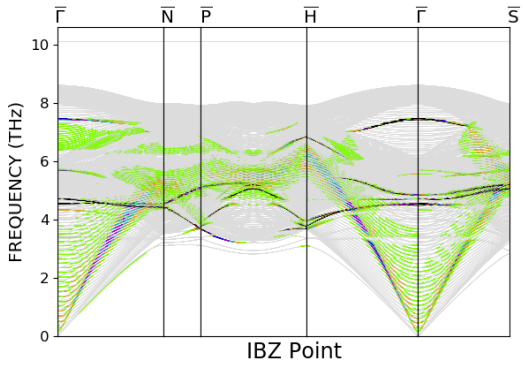

(c) First substrate layer longitudinal polarization

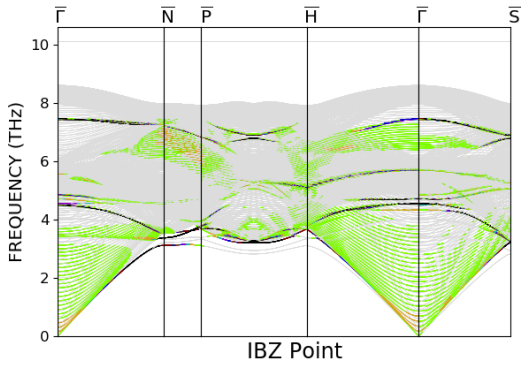

(d) First substrate layer shear horizontal polarization

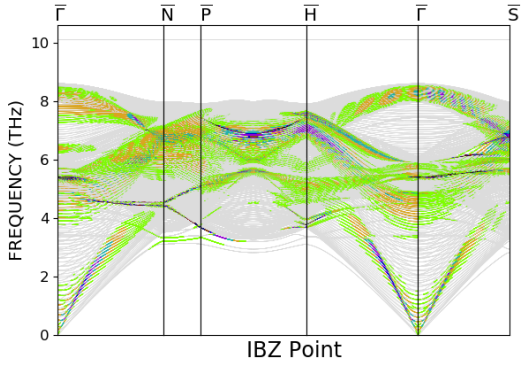

(e) Second substrate layer longitudinal polarization

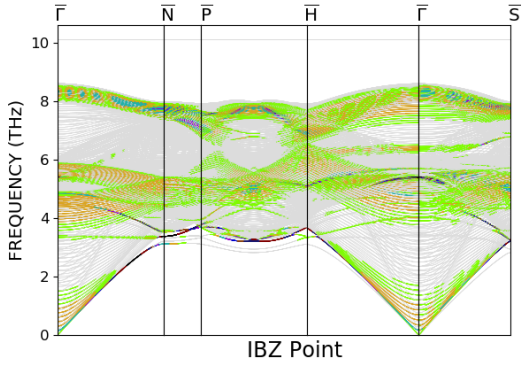

(f) Second substrate layer shear horizontal polarization

Figure 5.24. Dispersion curves for a quarter monolayer of Li on the 110 surface of Mo. Longitudinal (shear horizontal) projections are shown on the left (right).

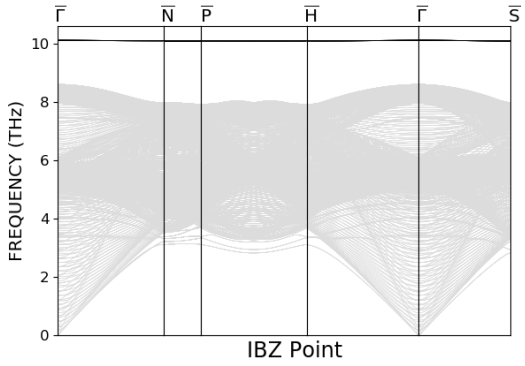

(a) Alkali layer shear vertical polarization

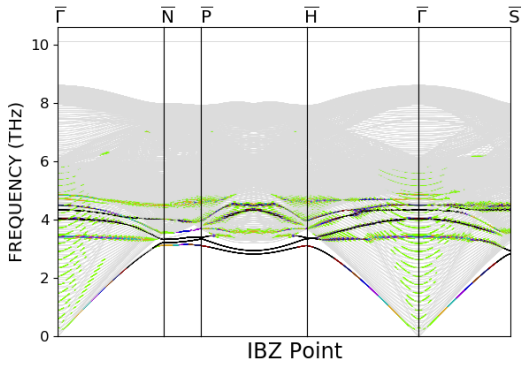

(b) First substrate layer shear vertical polarization

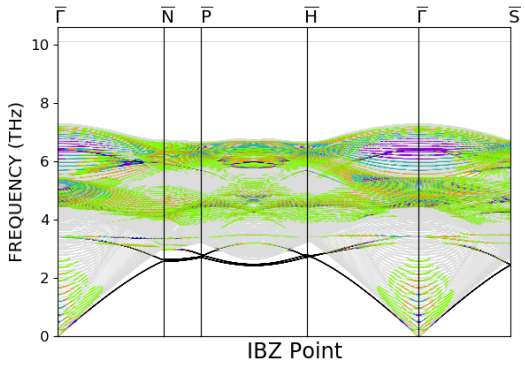

(c) Second substrate layer shear vertical polarization

Figure 5.25. Dispersion curves for a quarter monolayer of Li on the 110 surface of Mo projected in the shear vertical direction.

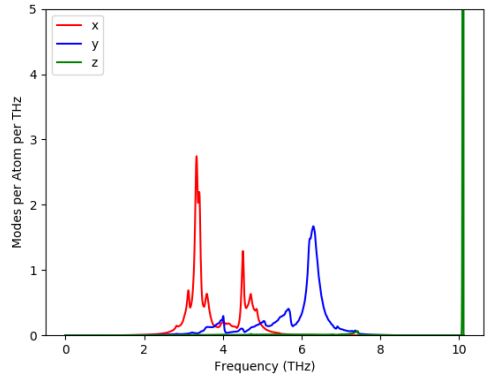

(a) Alkali layer density of states

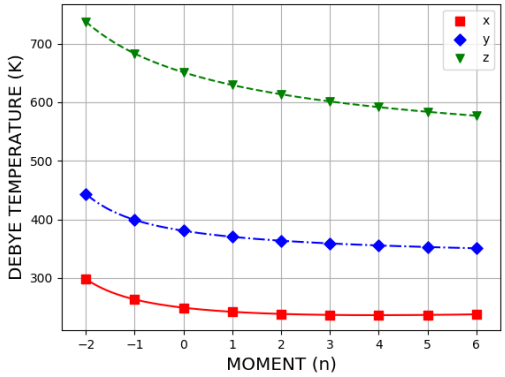

(b) Alkali layer Debye tempteratures

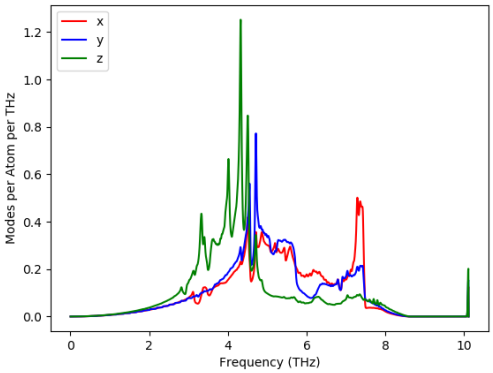

(c) First substrate layer density of states

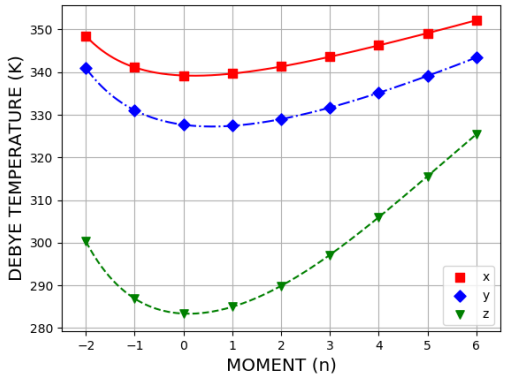

(d) First substrate layer Debye tempteratures

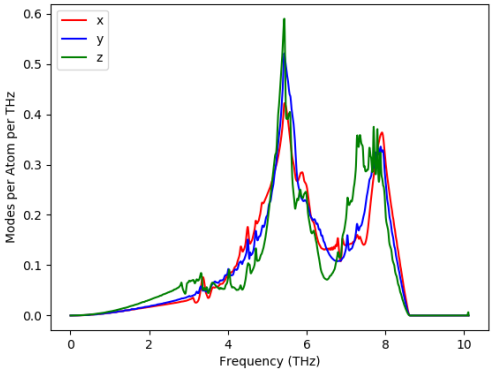

(e) Second substrate layer density of states

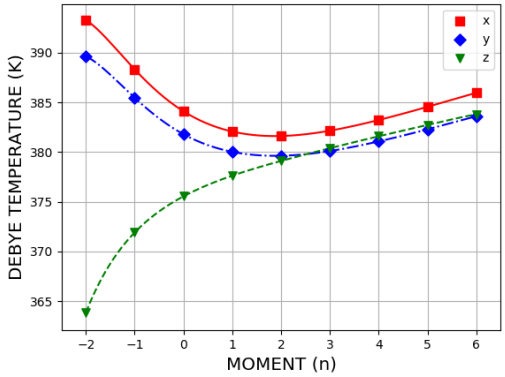

(f) Second substrate layer Debye tempteratures

Figure 5.26. Densities of states and Debye temperatures for a quarter monolayer of Li on the 110 surface of Mo, projected on to the x, y, and z directions.

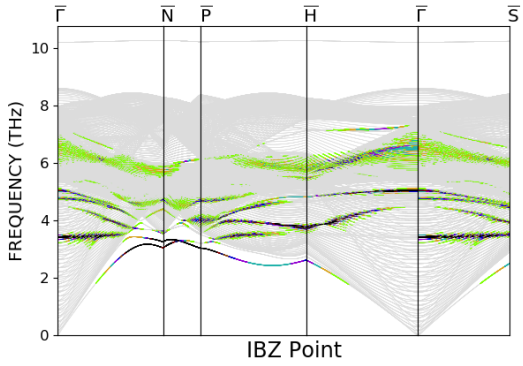

(a) Alkali layer longitudinal polarization

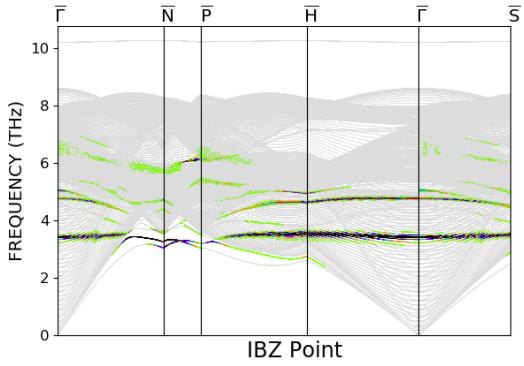

(b) Alkali layer shear horizontal polarization

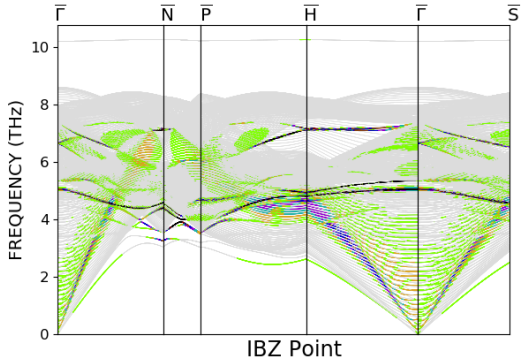

(c) First substrate layer longitudinal polarization

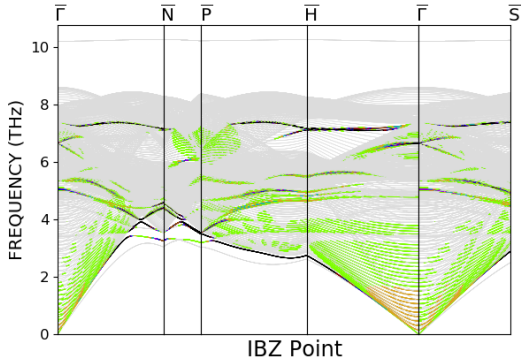

(d) First substrate layer shear horizontal polarization

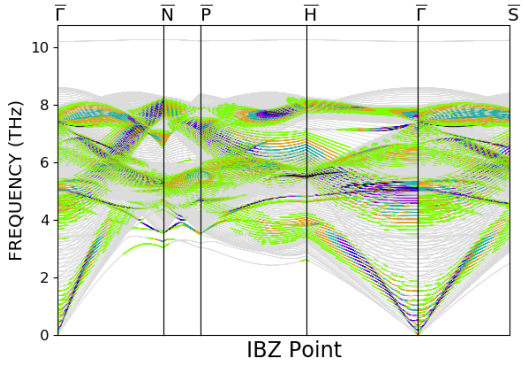

(e) Second substrate layer longitudinal polarization

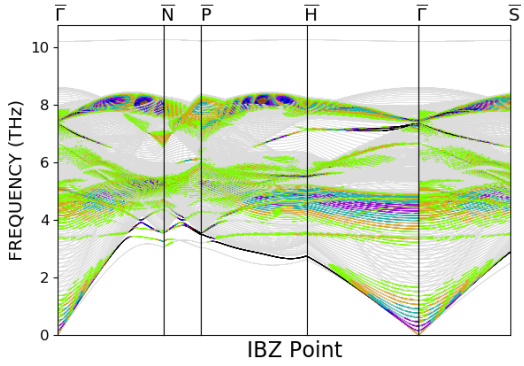

(f) Second substrate layer shear horizontal polarization

Figure 5.27. Dispersion curves for a third monolayer of Li on the 110 surface of Mo. Longitudinal (shear horizontal) projections are shown on the left (right).

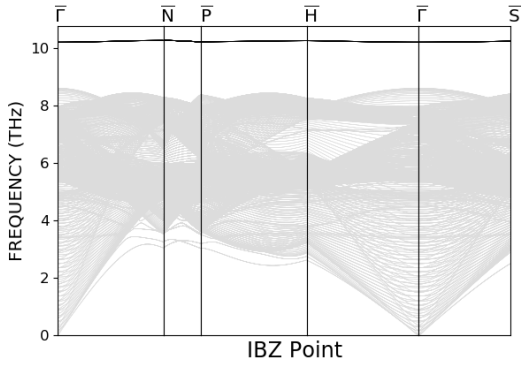

(a) Alkali layer shear vertical polarization

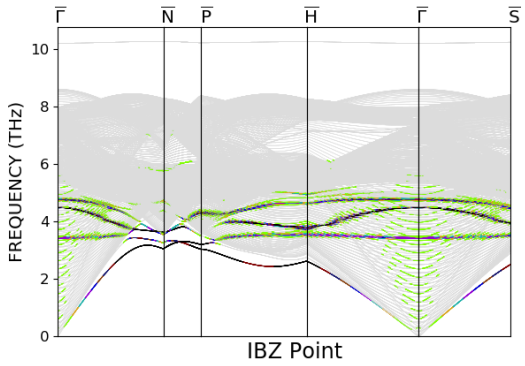

(b) First substrate layer shear vertical polarization

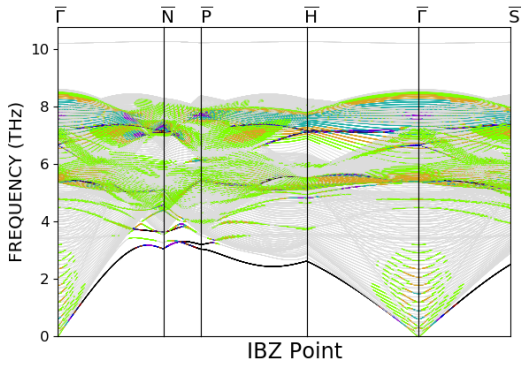

(c) Second substrate layer shear vertical polarization

Figure 5.28. Dispersion curves for a third monolayer of Li on the 110 surface of Mo projected in the shear vertical direction.

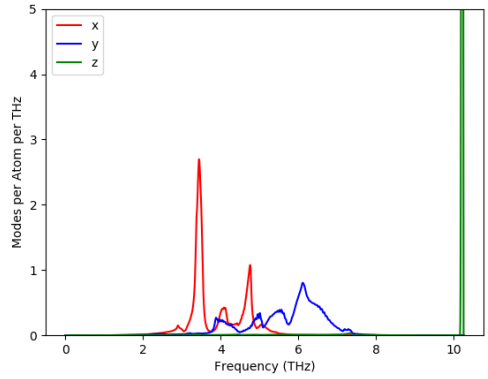

(a) Alkali layer density of states

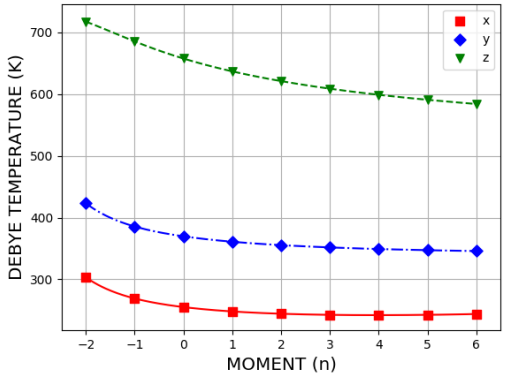

(b) Alkali layer Debye tempteratures

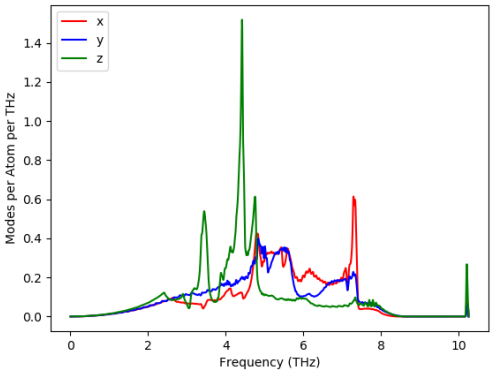

(c) First substrate layer density of states

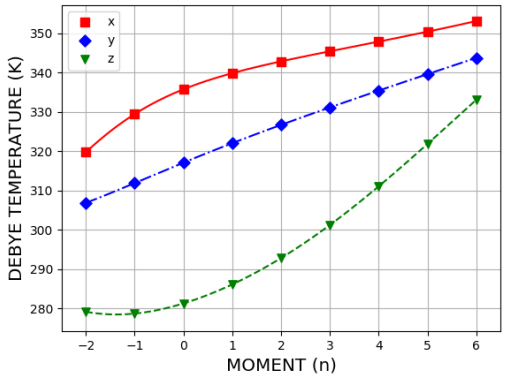

(d) First substrate layer Debye tempteratures

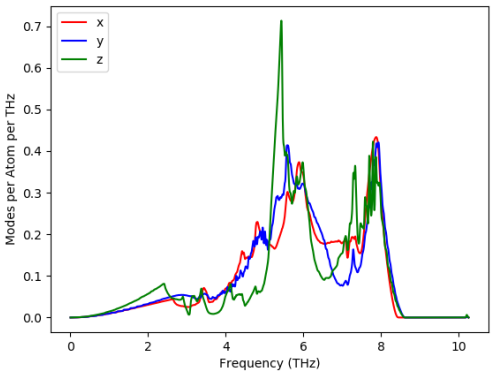

(e) Second substrate layer density of states

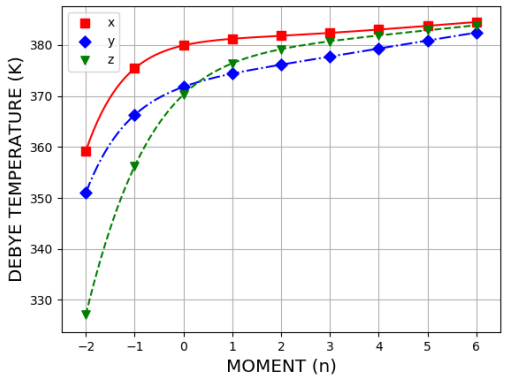

(f) Second substrate layer Debye tempteratures

Figure 5.29. Densities of states and Debye temperatures for a third monolayer of Li on the 110 surface of Mo, projected on to the x, y, and z directions.

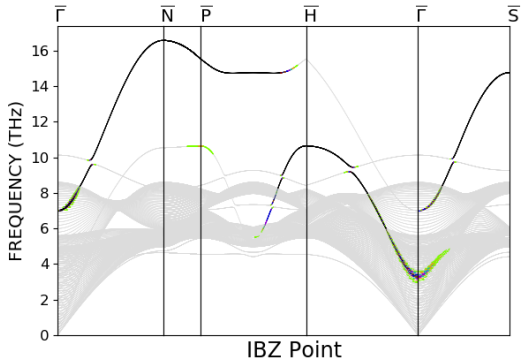

(a) Alkali layer longitudinal polarization

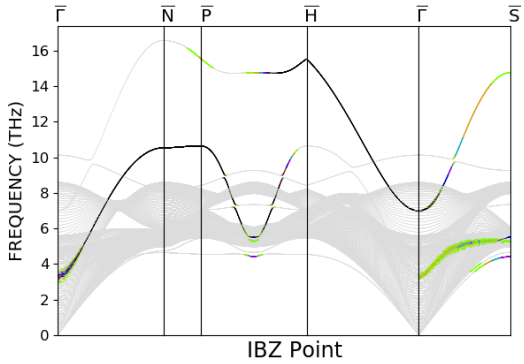

(b) Alkali layer shear horizontal polarization

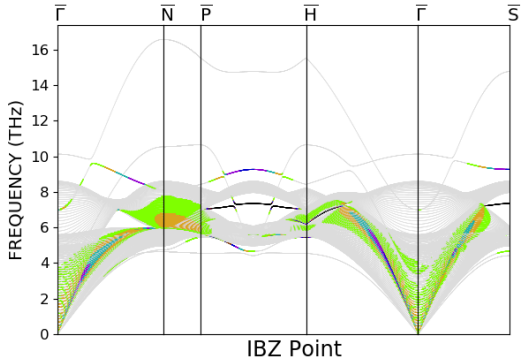

(c) First substrate layer longitudinal polarization

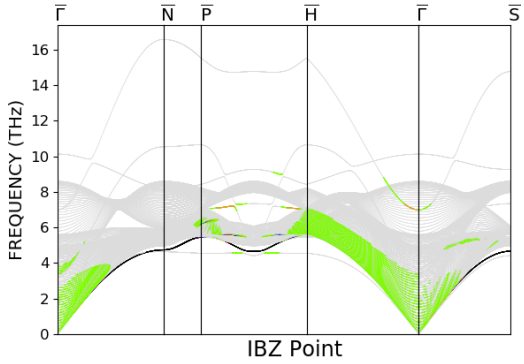

(d) First substrate layer shear horizontal polarization

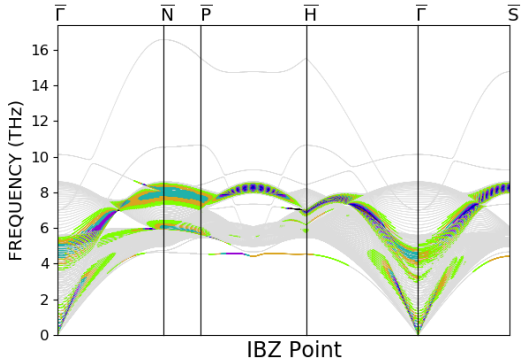

(e) Second substrate layer longitudinal polarization

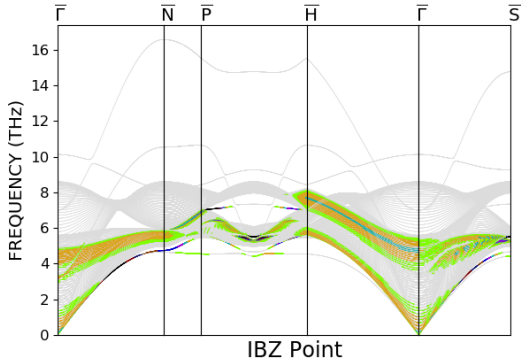

(f) Second substrate layer shear horizontal polarization

Figure 5.30. Dispersion curves for a full monolayer of Li on the 110 surface of Mo. Longitudinal (shear horizontal) projections are shown on the left (right).

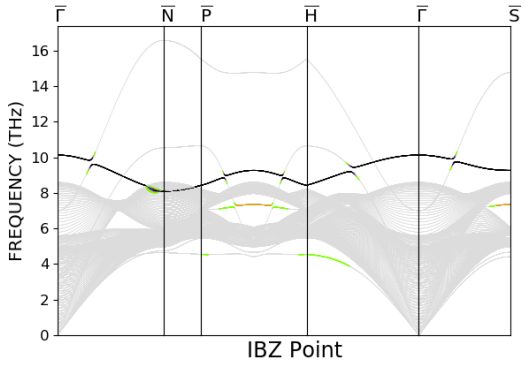

(a) Alkali layer shear vertical polarization

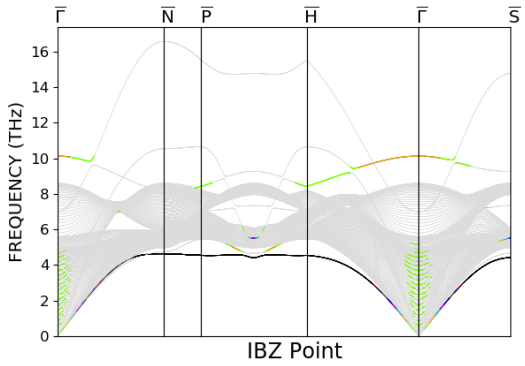

(b) First substrate layer shear vertical polarization

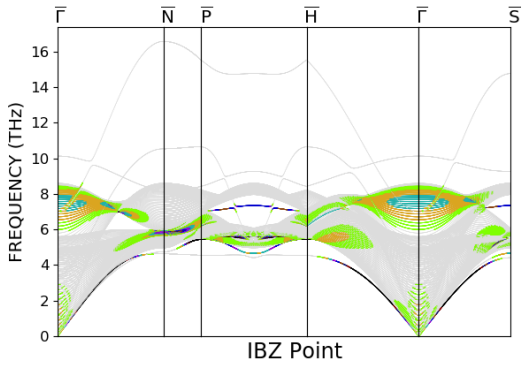

(c) Second substrate layer shear vertical polarization

Figure 5.31. Dispersion curves for a full monolayer of Li on the 110 surface of Mo projected in the shear vertical direction.

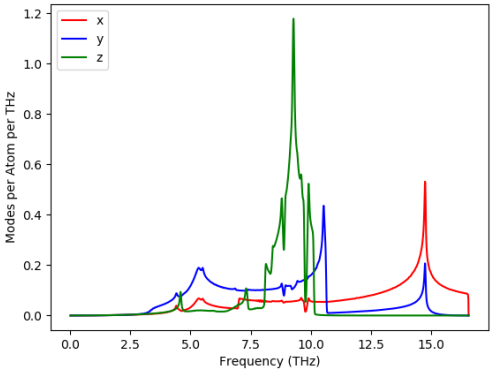

(a) Alkali layer density of states

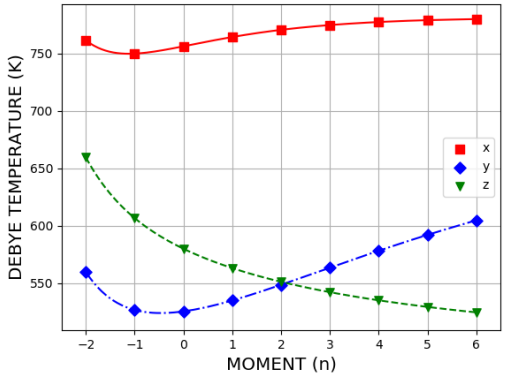

(b) Alkali layer Debye tempteratures

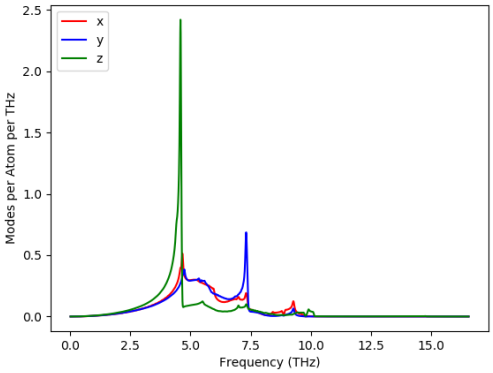

(c) First substrate layer density of states

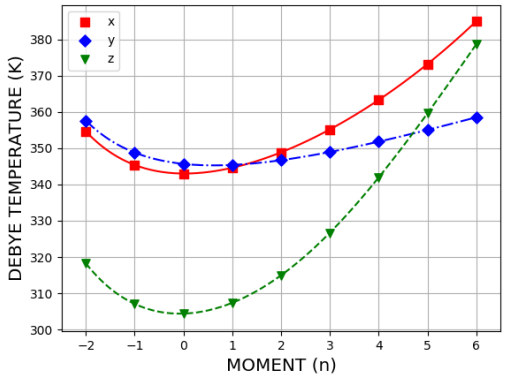

(d) First substrate layer Debye tempteratures

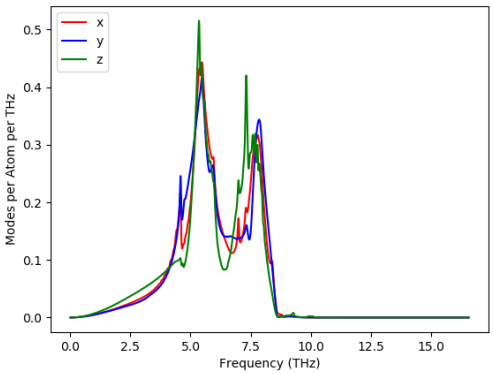

(e) Second substrate layer density of states

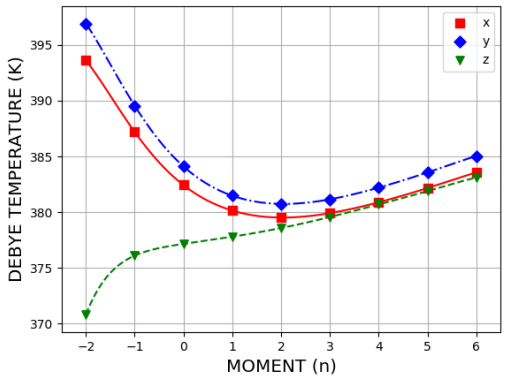

(f) Second substrate layer Debye tempteratures

Figure 5.32. Densities of states and Debye temperatures for a full monolayer of Li on the 110 surface of Mo, projected on to the x, y, and z directions.

The densities of states of Li on W and Mo suggest that the dynamics of these two bimetallic systems are very similar. We can briefly summarize the results by examining the target outputs discussed in chapter 4 for each coverage. These results, which include the three modes obtained by holding the substrate fixed while allowing the alkali layer to be dynamic, the height of the alkali layer, and binding energy of the alkali layer, are shown in Table 5.1.

Table 5.1. Calculated frequencies, binding energies, and Li layer heights for a full, third, quarter, and sixth monolayer of Li on the 110 surface of W and Mo.

Substrate	Coverage	h (ang)	E_{coh} (eV)	ν_1 (THz)	ν_2 (Thz)	ν_3 (Thz)
W	1	2.53	2.48	3.27	6.74	9.68
	$\frac{1}{3}$	2.47	2.34	4.01	5.88	10.09
	$\frac{1}{4}$	2.46	2.33	3.99	5.76	10.01
	$\frac{1}{6}$	2.47	3.33	4.07	5.82	10.13
Mo	1	2.53	2.47	3.23	6.7	9.74
	$\frac{1}{3}$	2.48	2.36	3.90	5.97	10.01
	$\frac{1}{4}$	2.47	2.35	3.85	5.86	9.90
	$\frac{1}{6}$	2.48	2.35	3.96	5.93	10.05

This similarity is not surprising; W and Mo have lattice constants which are very close to each other, and the ZWJ heterogeneous models we constructed in chapter 4 for the W-Li and Mo-Li interaction have parameters which are nearly identical. We can easily compare the vibrations of Li on W(110) and Mo(110) by comparing the alkali layer density of states of a sixth monolayer of Li on W (Figure 5.8) to the alkali layer density of state of a sixth monolayer of Li on Mo(110) (Figure 5.23). These figures suggest that the Li atoms behave the same on W and on Mo. For this reason, the remaining calculations of the (100) and (111) transition metal surfaces will only include results using a W substrate.

We also note that the three fractional coverages for the W substrates, as well as the three fractional coverages on the Mo substrates are nearly identical. This makes sense, given the relatively short range of the heterogeneous potential. In each of these coverages, the Li atoms interact very weakly with each other, evidenced by the relatively flat dispersion of the projection

on to the alkali layer when compared to the dispersion seen in the full monolayer. Therefore, from the perspective of the Li atoms, there is virtually no difference between a third, a quarter, and a sixth of a monolayer.

5.2. (100) Surface

On the (100) surface, we examine K at a coverage of a half and a quarter monolayer. These systems were observed experimentally in [13]. The two coverages are shown in Figure 5.33, with unit cells outlined in red. The Brillouin zones for each of these systems is shown in Figure 5.34.

For the half monolayer IBZ, we use a mesh of 31,375 points to calculate the densities of states. For the quarter monolayer, we use a mesh of 7,875 points. We use a slab with 72 layers of W atoms for our calculations on the (100) surface. This number of layers give a slab thickness of 113.9 Å, which is nearly identical to the 51 layer (110) slab thickness of 114.1 Å. As with the (110) surface, we begin by examining a clean slab of (100) W. The dispersion curves and densities of states for the clean surface, the quarter, and half monolayer are shown in Figs. 5.35, 5.36, 5.37, 5.38, 5.39, 5.40, 5.41, 5.42, and 5.43.

We choose the four-fold hollow site for our K atoms. This is binding site is suggested by a LEED study performed by MacRae *et. al* [14], although more work can be done to verify that this site does indeed minimize the binding energy.

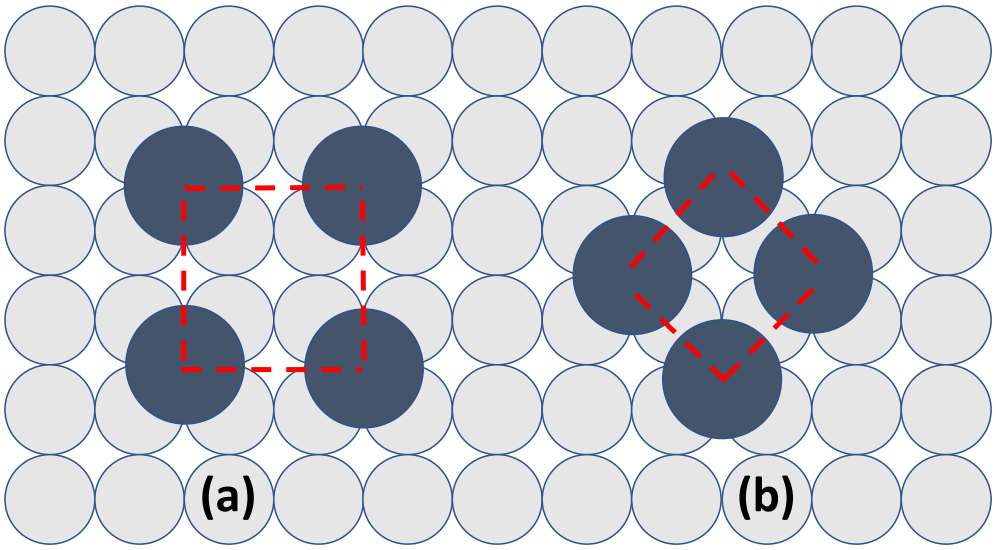

Figure 5.33. Unit cells for a (a) quarter and (b) half monolayer on the (100) surface.

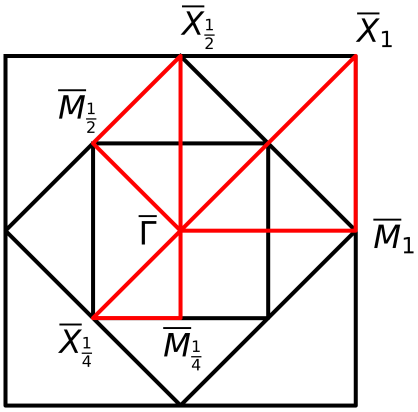

Figure 5.34. The Brillouin zones for a full, half, and quarter, monolayer on the (100) surface. Subscripts on points indicate to which coverage the point corresponds.

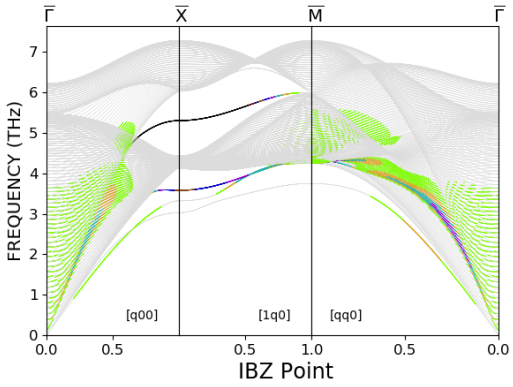

(a) First layer longitudinal polarization

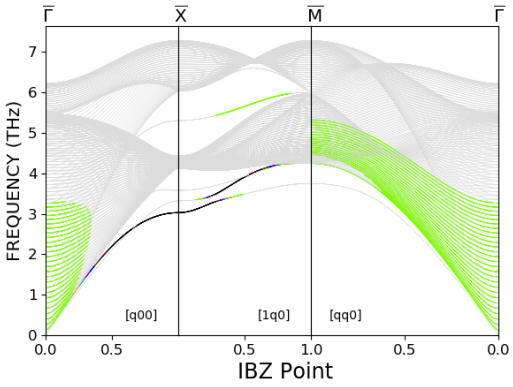

(b) First layer shear horizontal polarization

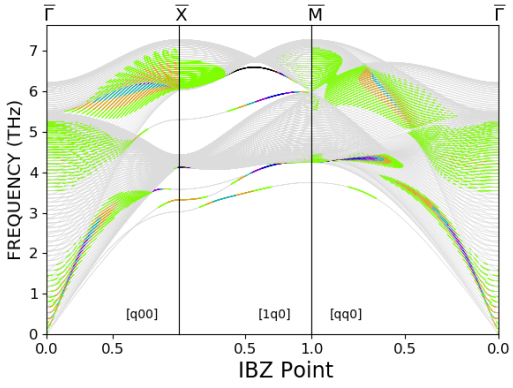

(c) Second layer longitudinal polarization

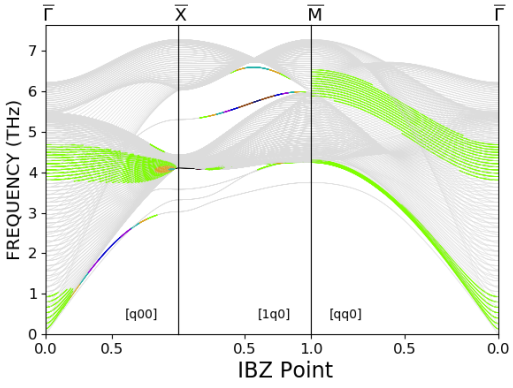

(d) Second layer shear horizontal polarization

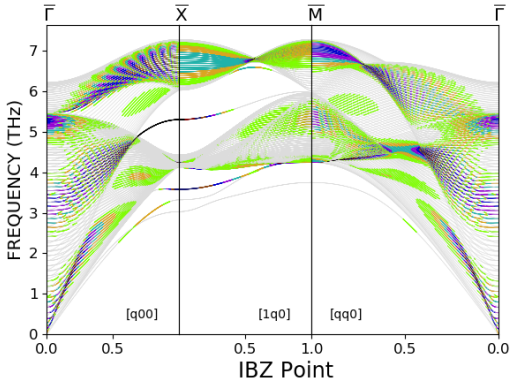

(e) Third layer longitudinal polarization

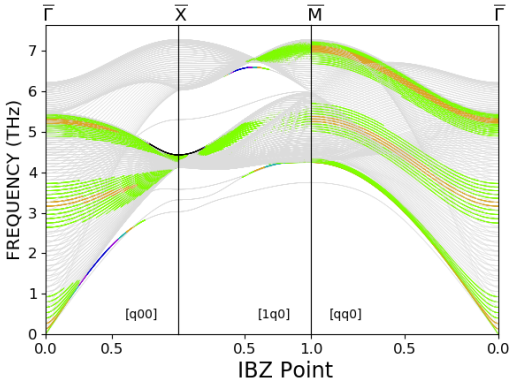

(f) Third layer shear horizontal polarization

Figure 5.35. Dispersion curves for a clean slab of the (100) surface of W. Longitudinal (shear horizontal) projections are shown on the left (right).

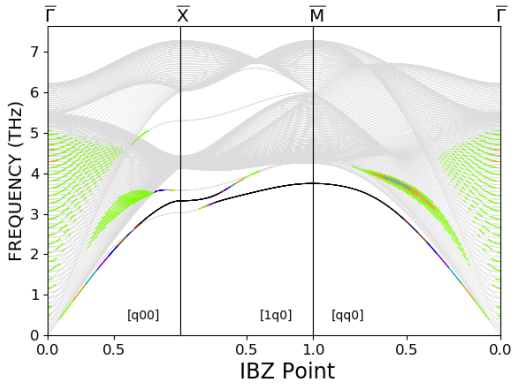

(a) First layer shear vertical polarization

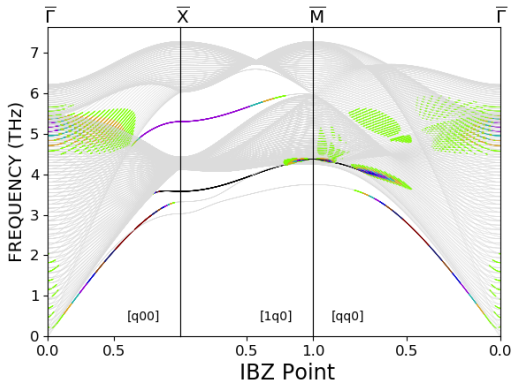

(b) Second layer shear vertical polarization

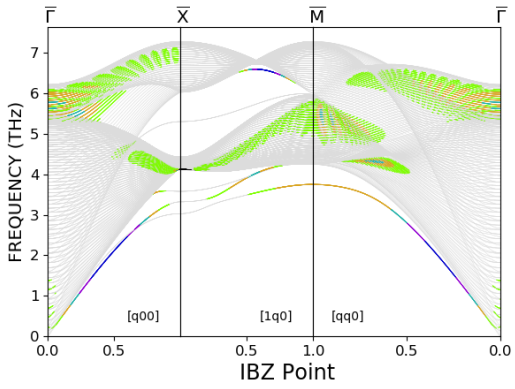

(c) Third layer shear vertical polarization

Figure 5.36. Dispersion curves for a clean slab of the (100) surface of W projected in the shear vertical direction.

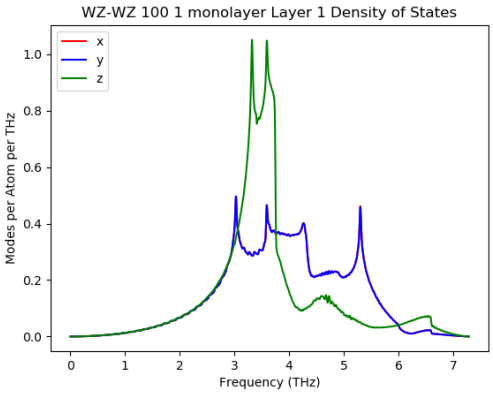

(a) Fist layer density of states

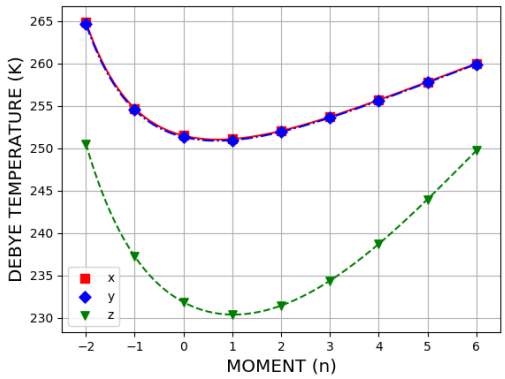

(b) Fist layer Debye tempteratures

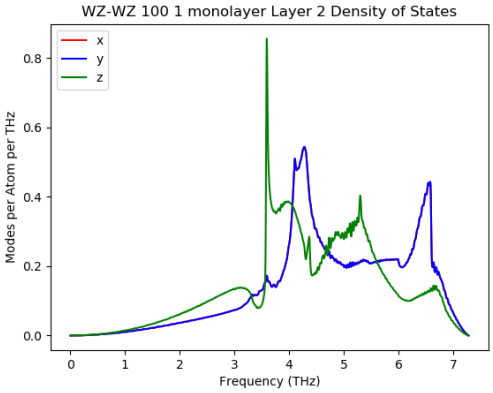

(c) Second layer density of states

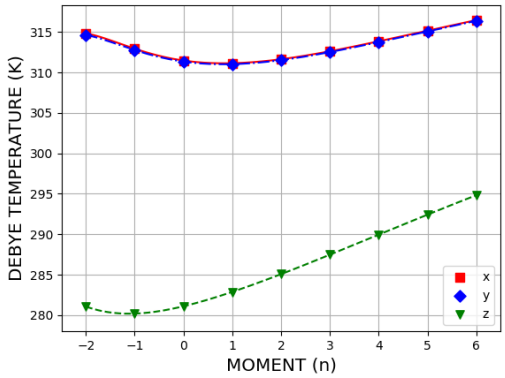

(d) Second layer Debye tempteratures

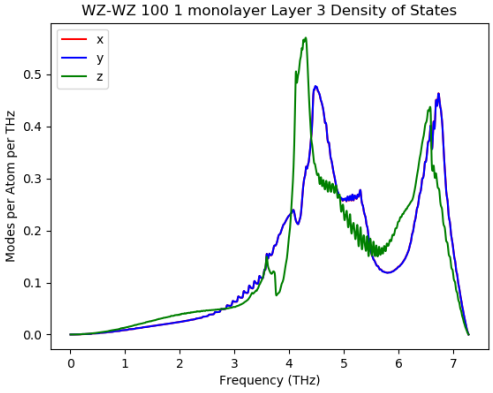

(e) Third layer density of states

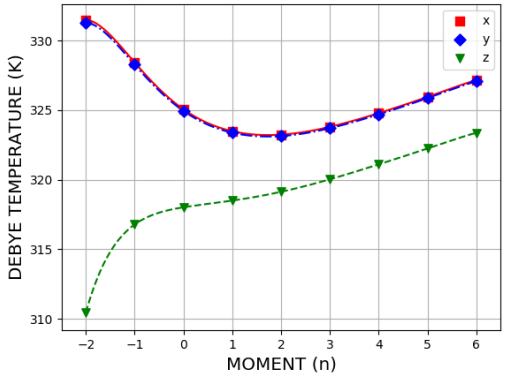

(f) Third layer Debye tempteratures

Figure 5.37. Densities of states and Debye temperatures for a clean slab of the (100) surface of W, projected on to the x, y, and z directions.

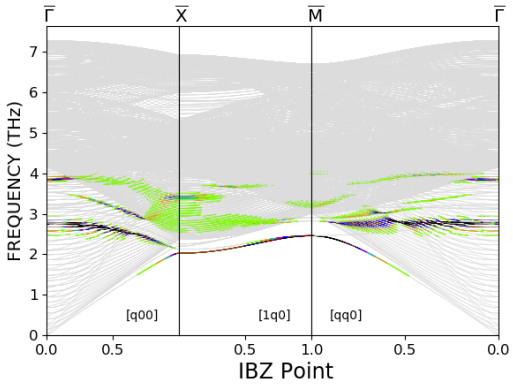

(a) Alkali layer longitudinal polarization

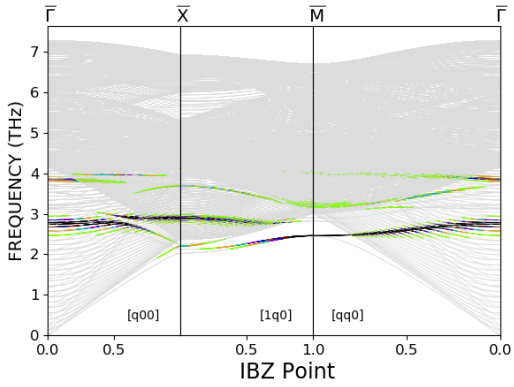

(b) Alkali layer shear horizontal polarization

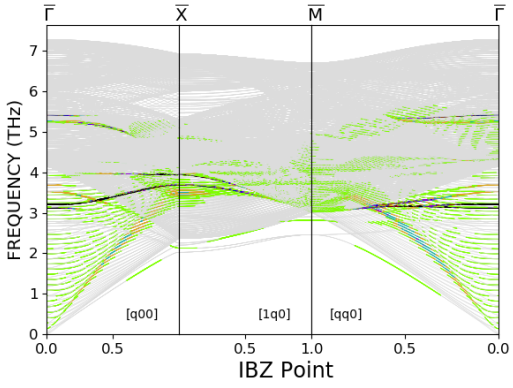

(c) First substrate layer longitudinal polarization

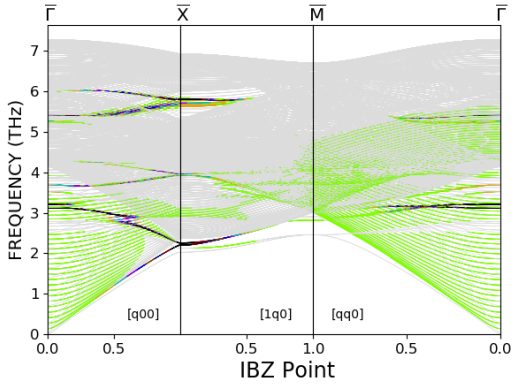

(d) First substrate layer shear horizontal polarization

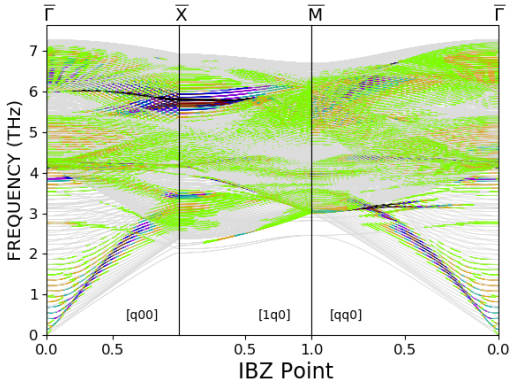

(e) Second substrate layer longitudinal polarization

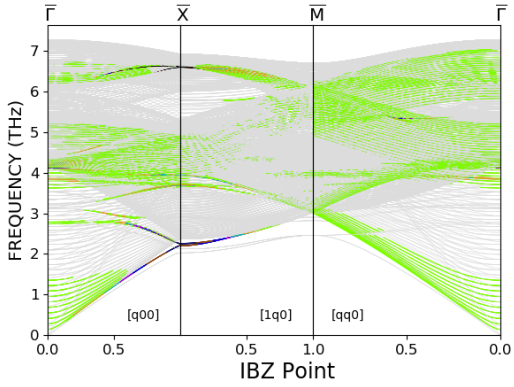

(f) Second substrate layer shear horizontal polarization

Figure 5.38. Dispersion curves for a quarter monolayer of K on the 100 surface of W. Longitudinal (shear horizontal) projections are shown on the left (right).

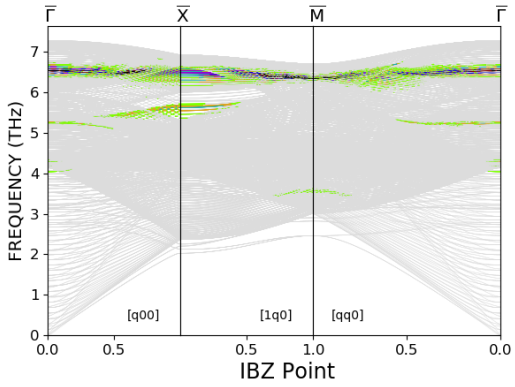

(a) Alkali layer shear vertical polarization

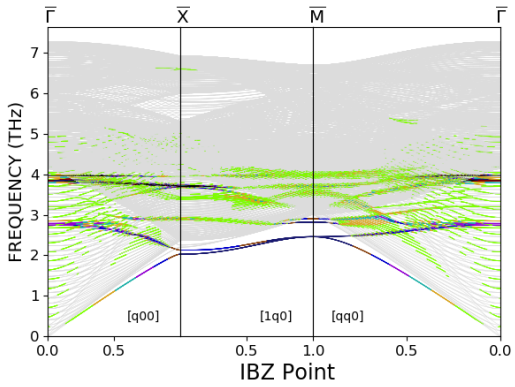

(b) First substrate layer shear vertical polarization

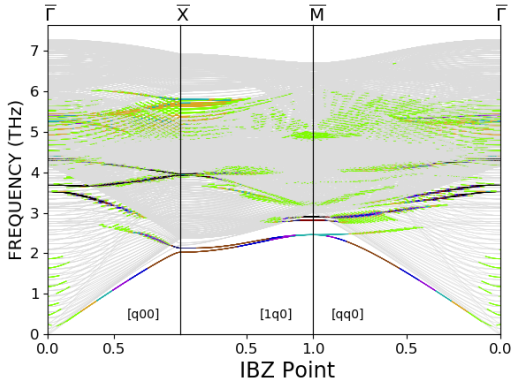

(c) Second substrate layer shear vertical polarization

Figure 5.39. Dispersion curves for a quarter monolayer of K on the 100 surface of W projected in the shear vertical direction.

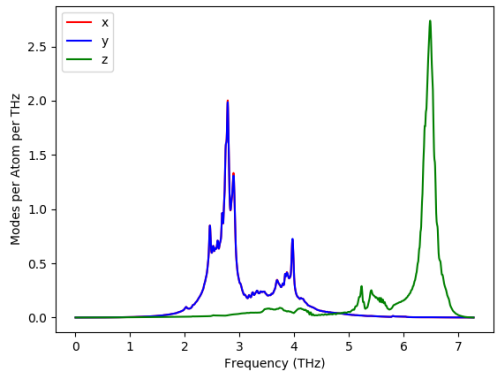

(a) Alkali layer density of states

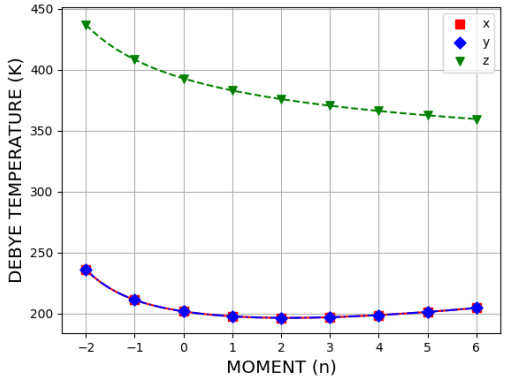

(b) Alkali layer Debye tempteratures

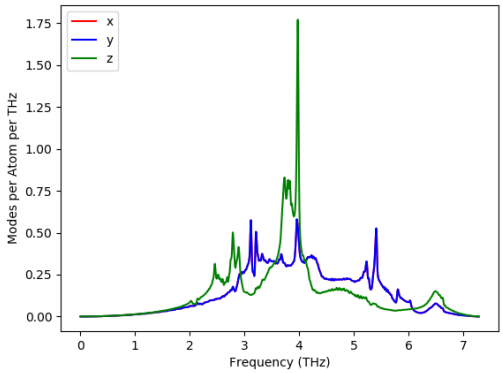

(c) First substrate layer density of states

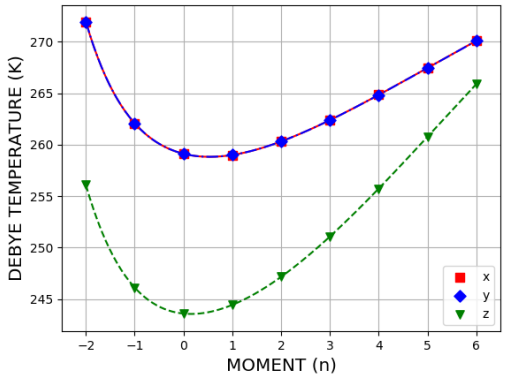

(d) First substrate layer Debye tempteratures

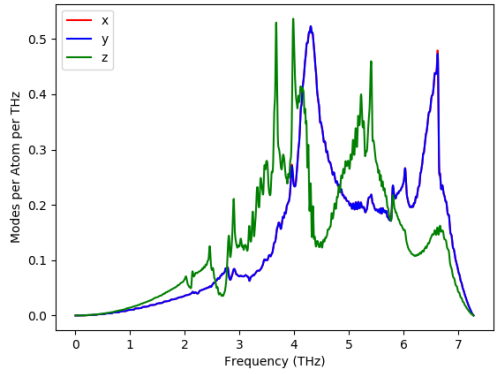

(e) Second substrate layer density of states

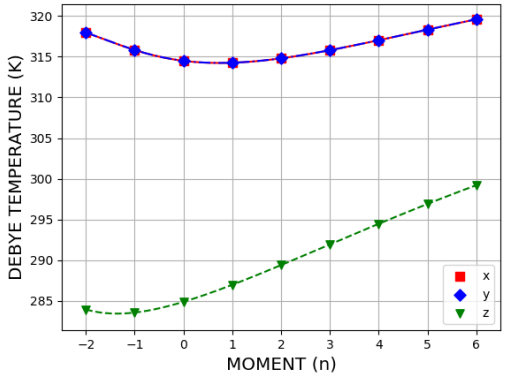

(f) Second substrate layer Debye tempteratures

Figure 5.40. Densities of states and Debye temperatures for a quarter monolayer of K on the 100 surface of W, projected on to the x, y, and z directions.

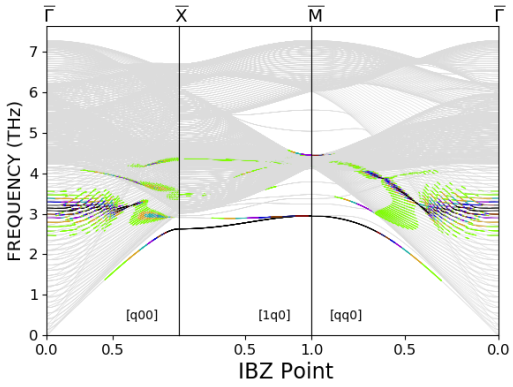

(a) Alkali layer longitudinal polarization

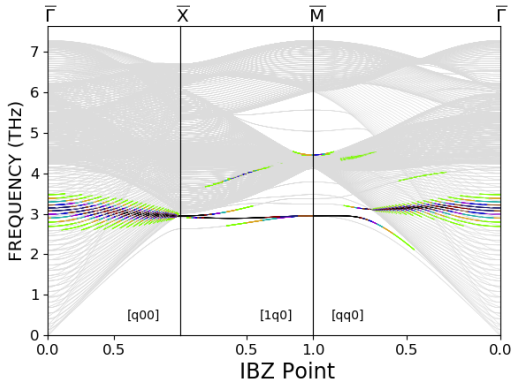

(b) Alkali layer shear horizontal polarization

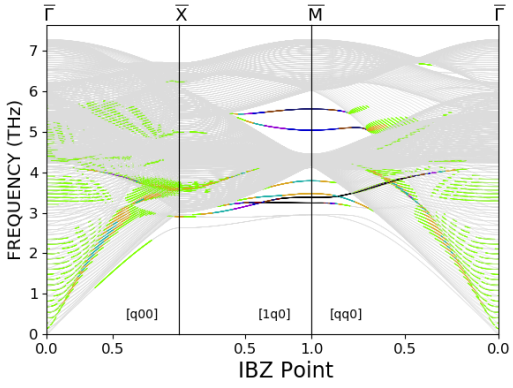

(c) First substrate layer longitudinal polarization

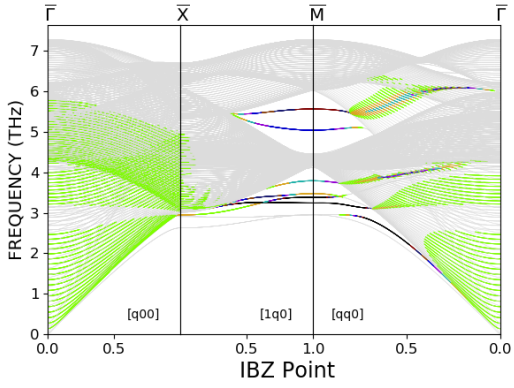

(d) First substrate layer shear horizontal polarization

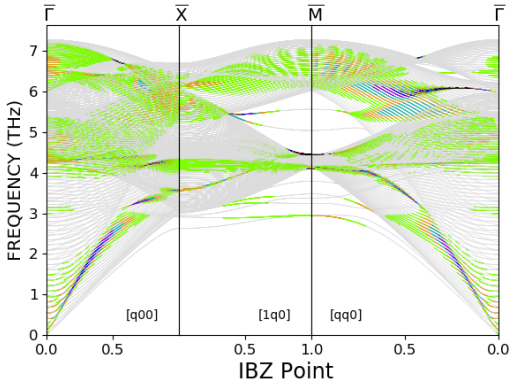

(e) Second substrate layer longitudinal polarization

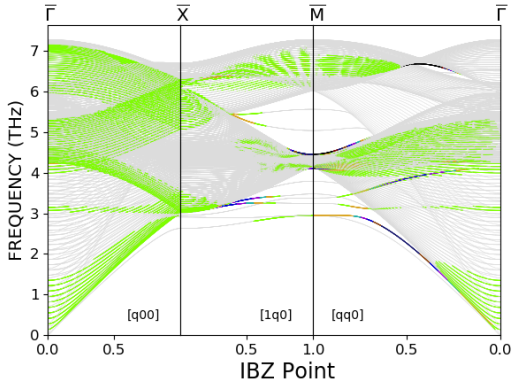

(f) Second substrate layer shear horizontal polarization

Figure 5.41. Dispersion curves for a half monolayer of K on the 100 surface of W. Longitudinal (shear horizontal) projections are shown on the left (right).

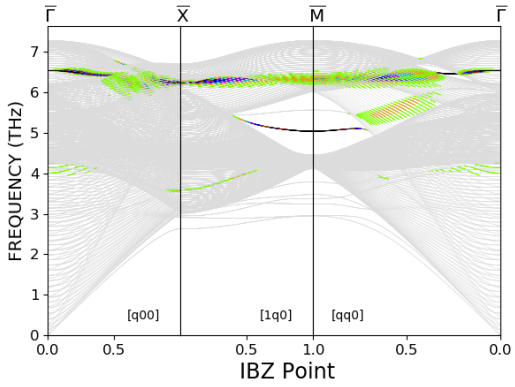

(a) Alkali layer shear vertical polarization

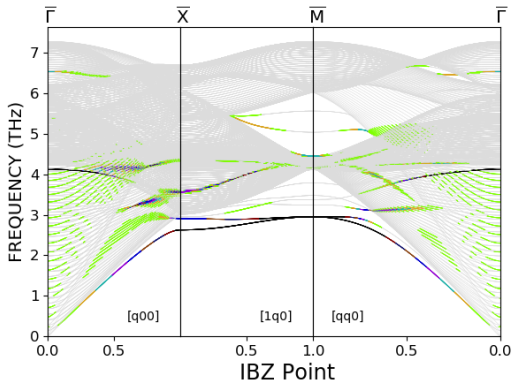

(b) First substrate layer shear vertical polarization

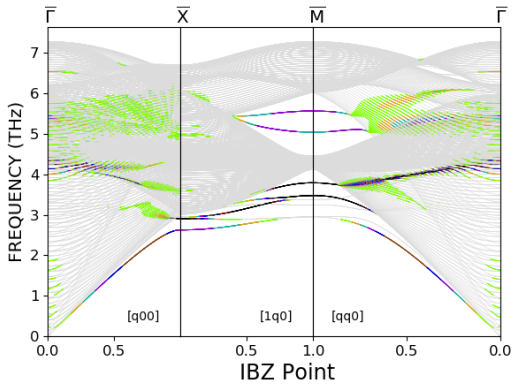

(c) Second substrate layer shear vertical polarization

Figure 5.42. Dispersion curves for a half monolayer of K on the 100 surface of W projected in the shear vertical direction.

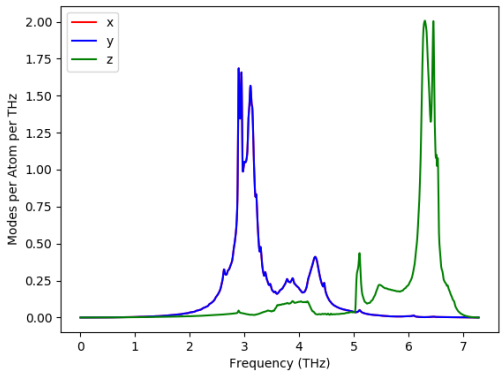

(a) Alkali layer density of states

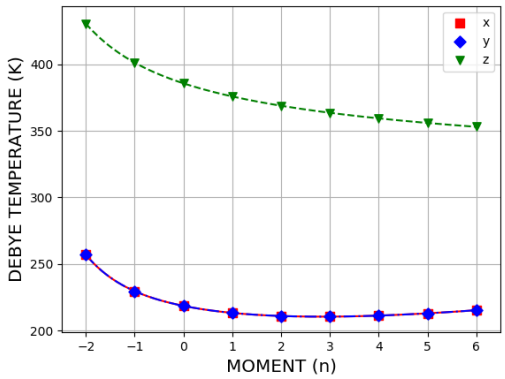

(b) Alkali layer Debye tempteratures

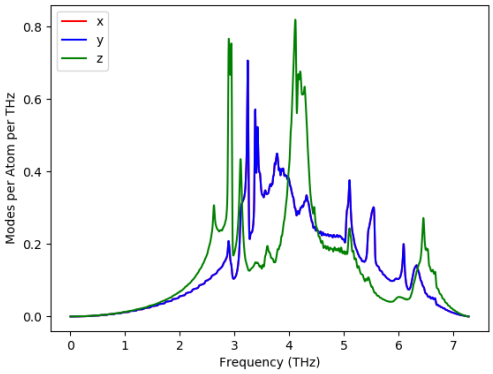

(c) First substrate layer density of states

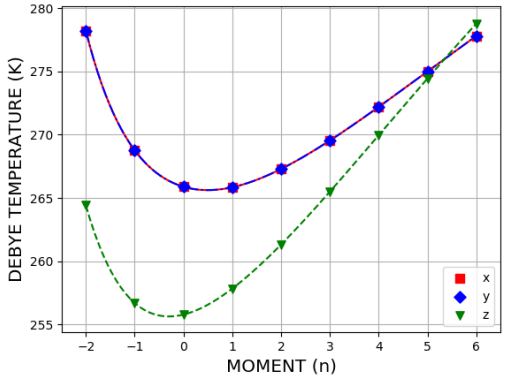

(d) First substrate layer Debye tempteratures

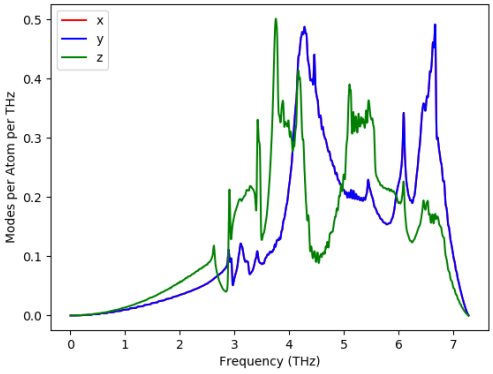

(e) Second substrate layer density of states

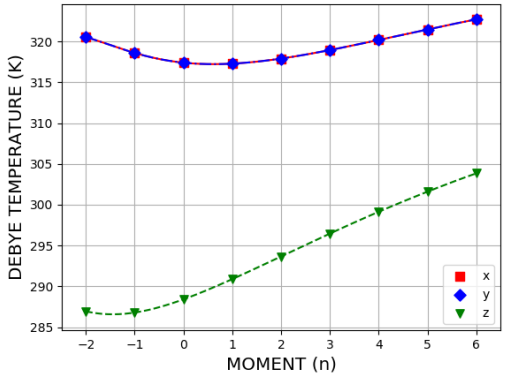

(f) Second substrate layer Debye tempteratures

Figure 5.43. Densities of states and Debye temperatures for a half monolayer of K on the 110 surface of W, projected on to the x, y, and z directions.

As with the (110) results, we can briefly summarize the results by looking at the characteristic values of the three modes obtained when holding the substrate fixed, the height of the

K layer, and the binding energy of the K layer. These results are shown in Table 5.2.

Table 5.2. Calculated frequencies, binding energies, and K layer heights for a half and quarter monolayer of K on the (100) surface of W.

Coverage	h (ang)	E_{coh} (eV)	ν_1 (THz)	ν_2 (Thz)	ν_3 (Thz)
$\frac{1}{2}$	3.10	2.79	3.09	3.09	5.97
$\frac{1}{4}$	3.07	2.65	3.18	3.19	6.05

We note that there is a small difference between the modes obtained with a half monolayer and a quarter monolayer of K. This indicates that, even at these lower coverages, there is some interaction between the K atoms.

5.3. (111) Surface

On the (111) surface, we examine Li, Na, K and Cs at a coverage of a full monolayer. Each of these alkali layers have been seen experimentally in [15]. The full monolayer is shown in Figure 5.44, with the unit cell outlined in red. The Brillouin zones for this system is shown in Figure 5.45.

A first-principles calculation performed by Yi *et. al* [8] suggests that the three-fold hollow FCC binding site minimizes the binding energy. Accordingly, we use this binding site for our system.

Once again, we begin by examining a clean slab of (111) W. We use a slab of 125 layers, once again giving us a slab thickness close to the 51 layers used for the (110) surface. For the IBZ of the full monolayer, we use a mesh of 34,369 points. The dispersion curves and densities of states for the clean surface and the Li, Na, K, and Cs monolayer are shown in Figs. 5.46, 5.47, 5.48, 5.49, 5.50, 5.51, 5.52, 5.53, 5.54, 5.55, 5.56, 5.57, 5.58, 5.59, and 5.60.

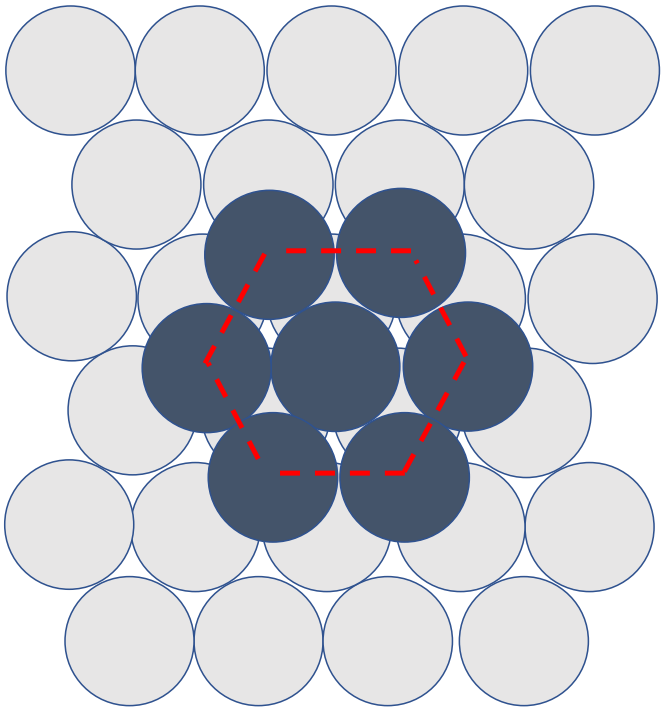

Figure 5.44. Unit cell for a full monolayer on the (111) surface.

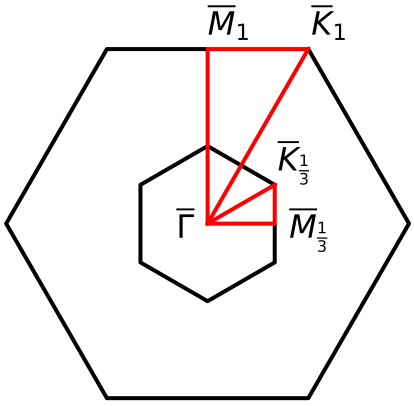

Figure 5.45. The Brillouin zones for a full and third monolayer on the (111) surface. Subscripts on points indicate to which coverage the point corresponds.

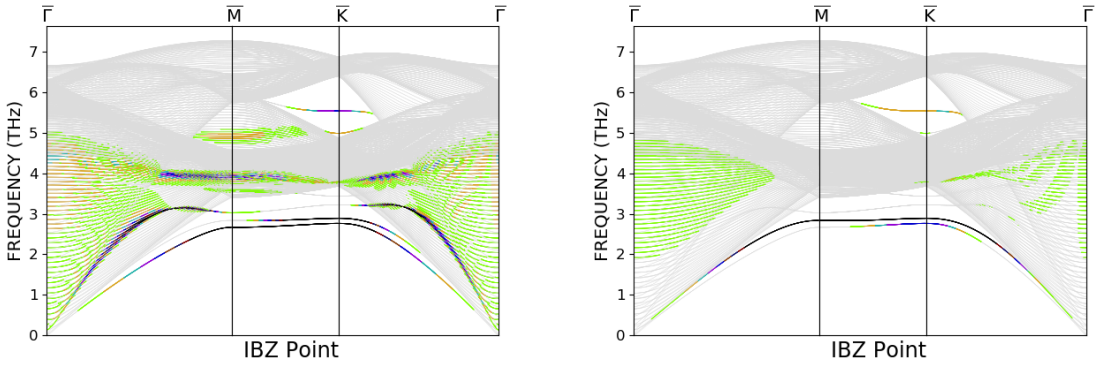

(a) First layer longitudinal polarization

(b) First layer shear horizontal polarization

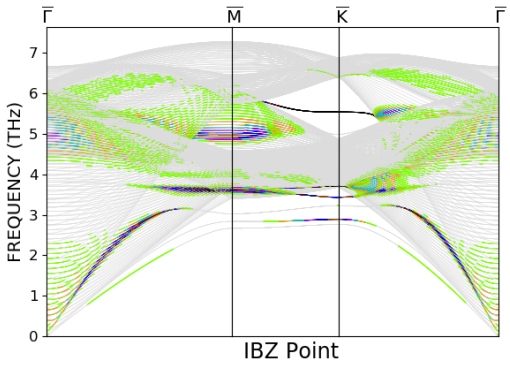

(c) Second layer longitudinal polarization

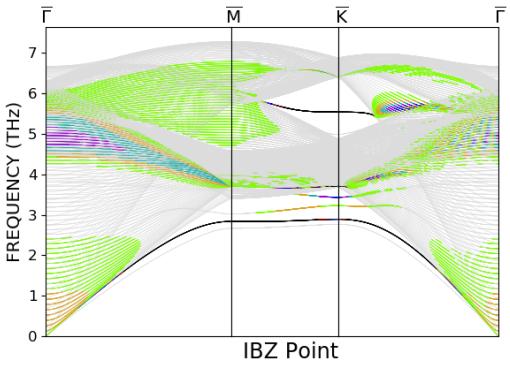

(d) Second layer shear horizontal polarization

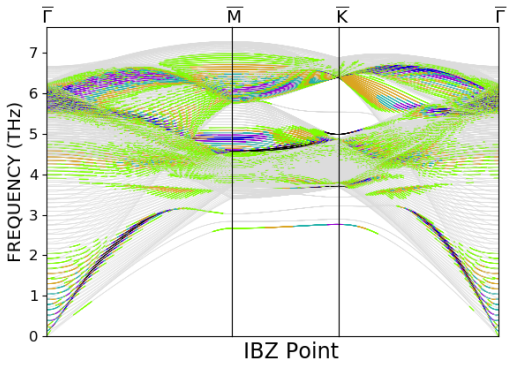

(e) Third layer longitudinal polarization

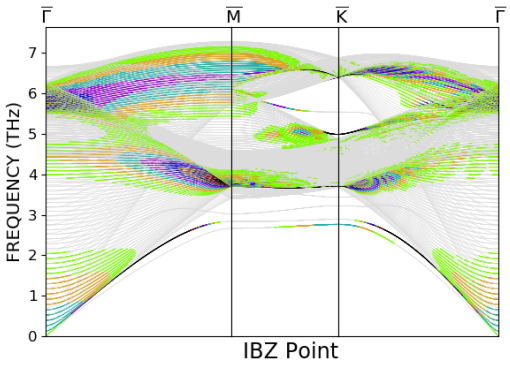

(f) Third layer shear horizontal polarization

Figure 5.46. Dispersion curves for a clean slab of the (111) surface of W. Longitudinal (shear horizontal) projections are shown on the left (right).

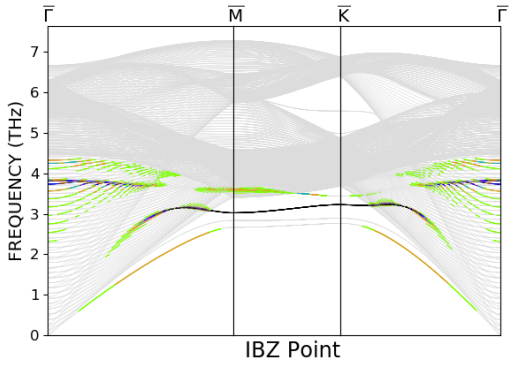

(a) First layer shear vertical polarization

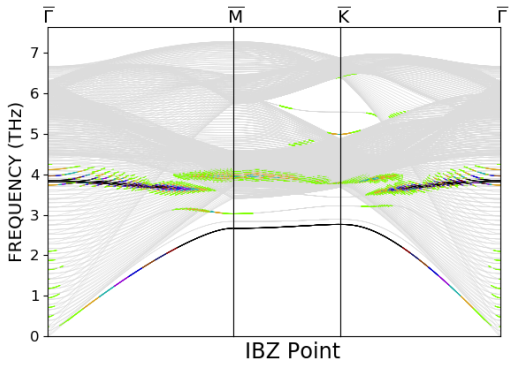

(b) Second layer shear vertical polarization

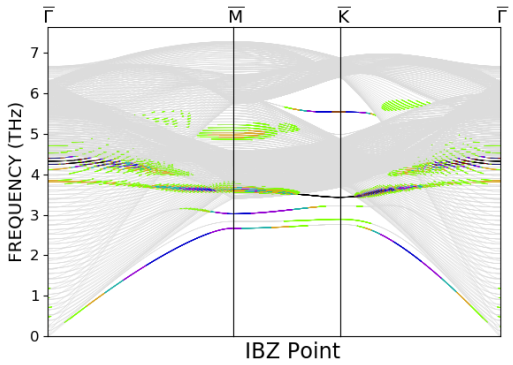

(c) Third layer shear vertical polarization

Figure 5.47. Dispersion curves for a clean slab of the (111) surface of W projected in the shear vertical direction.

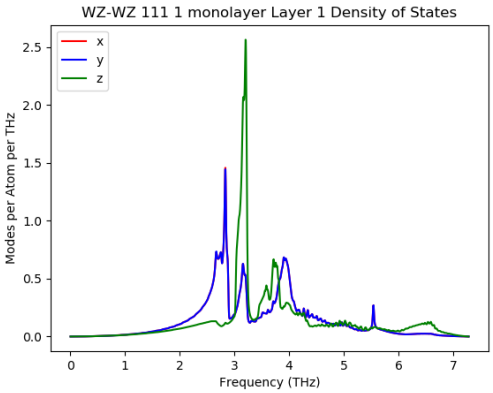

(a) Fist layer density of states

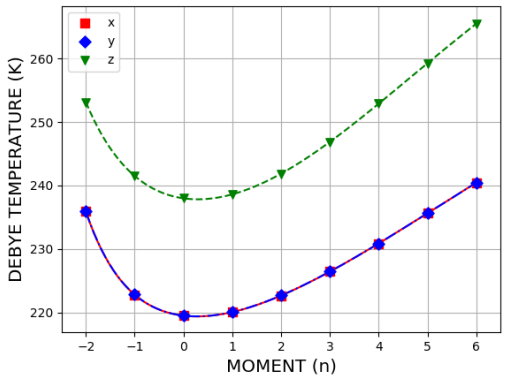

(b) Fist layer Debye tempteratures

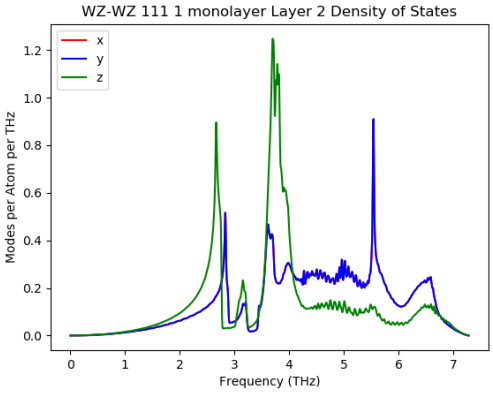

(c) Second layer density of states

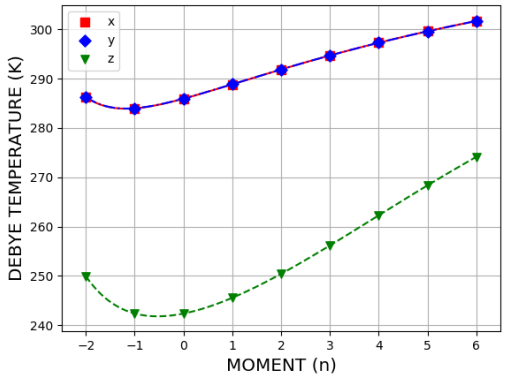

(d) Second layer Debye tempteratures

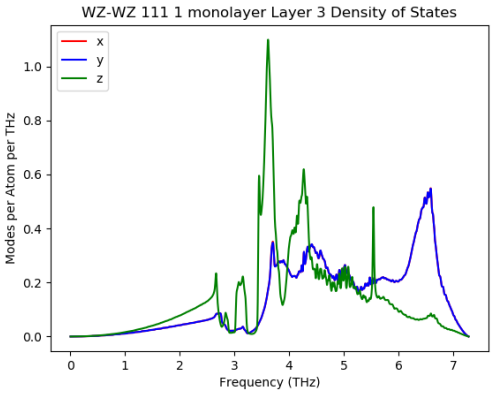

(e) Third layer density of states

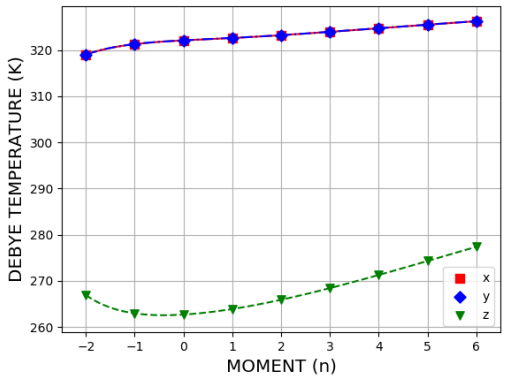

(f) Third layer Debye tempteratures

Figure 5.48. Densities of states and Debye temperatures for a clean slab of the (111) surface of W, projected on to the x, y, and z directions.

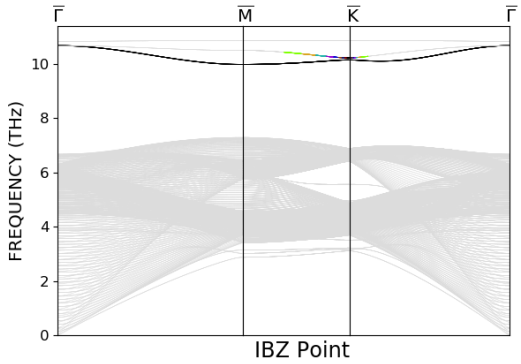

(a) Alkali layer longitudinal polarization

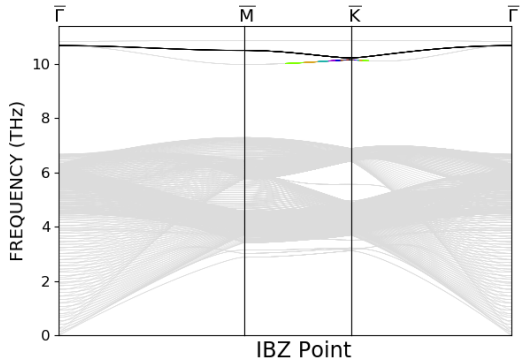

(b) Alkali layer shear horizontal polarization

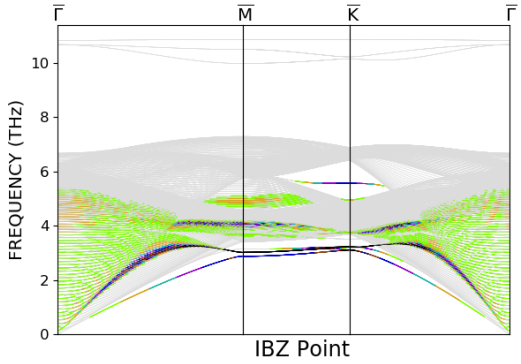

(c) First substrate layer longitudinal polarization

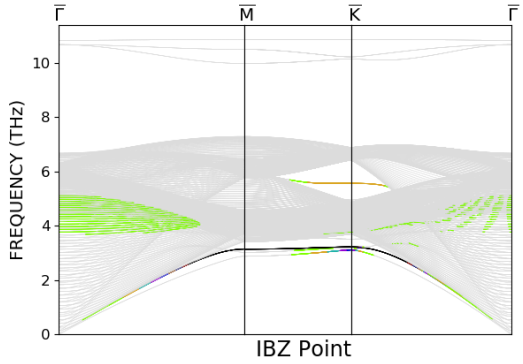

(d) First substrate layer shear horizontal polarization

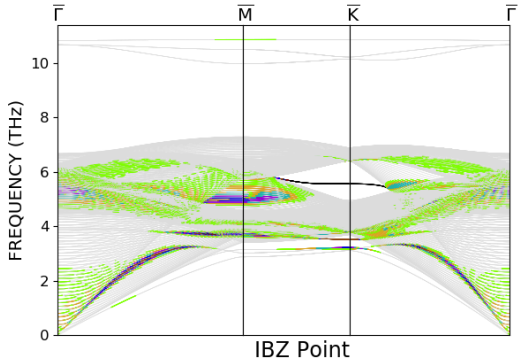

(e) Second substrate layer longitudinal polarization

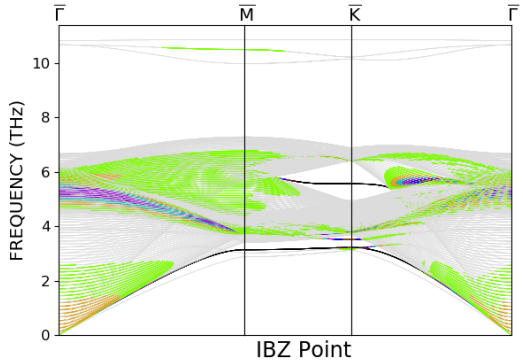

(f) Second substrate layer shear horizontal polarization

Figure 5.49. Dispersion curves for a full monolayer of Li on the 111 surface of W. Longitudinal (shear horizontal) projections are shown on the left (right).

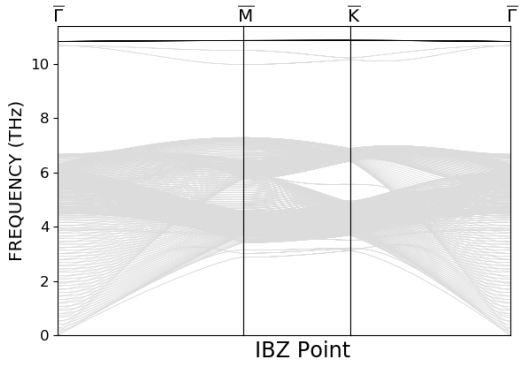

(a) Alkali layer shear vertical polarization

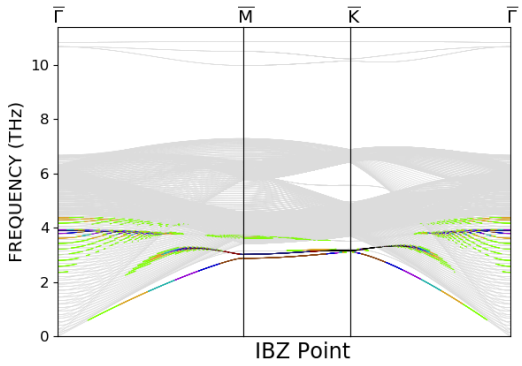

(b) First substrate layer shear vertical polarization

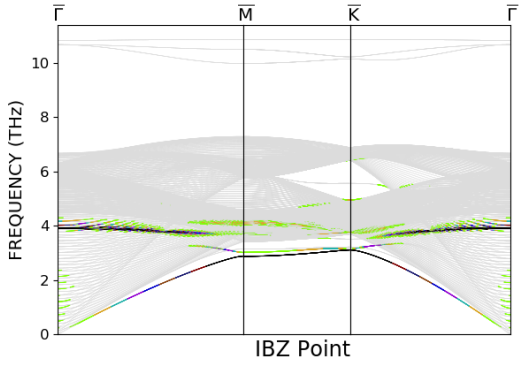

(c) Second substrate layer shear vertical polarization

Figure 5.50. Dispersion curves for a full monolayer of Li on the 111 surface of W projected in the shear vertical direction.

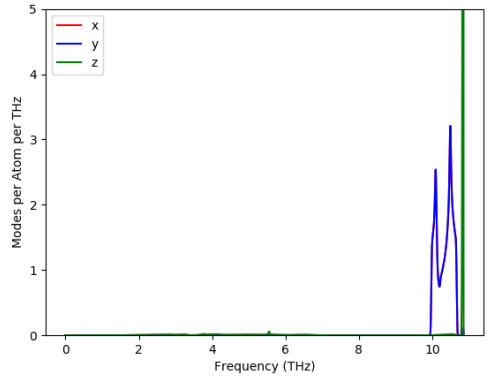

(a) Alkali layer density of states

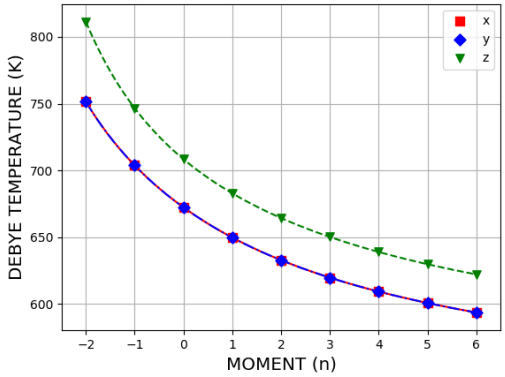

(b) Alkali layer Debye tempteratures

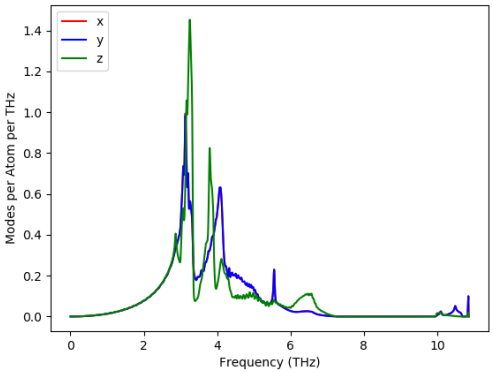

(c) First substrate layer density of states

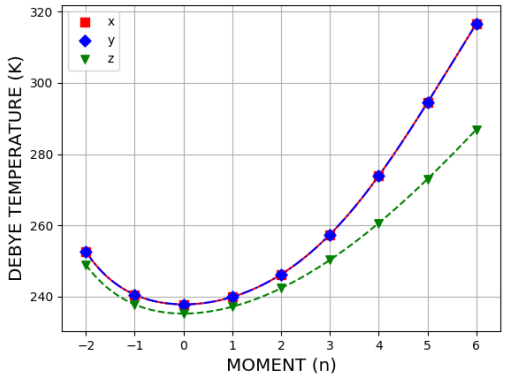

(d) First substrate layer Debye tempteratures

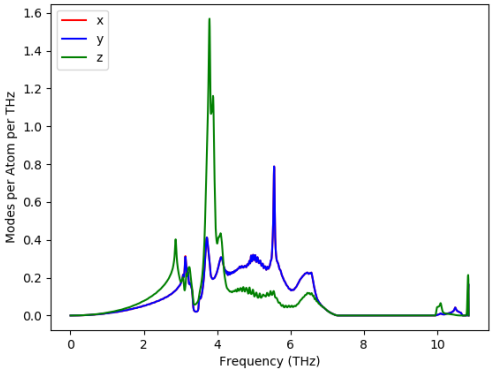

(e) Second substrate layer density of states

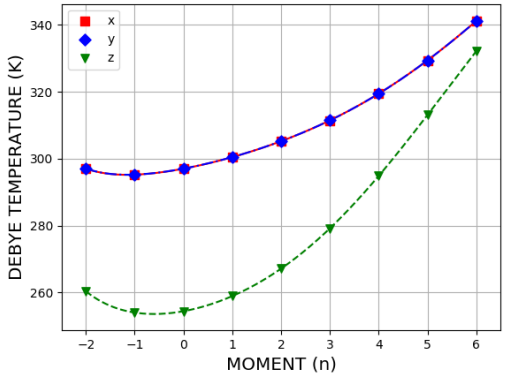

(f) Second substrate layer Debye tempteratures

Figure 5.51. Densities of states and Debye temperatures for a full monolayer of Li on the (111) surface of W, projected on to the x, y, and z directions.

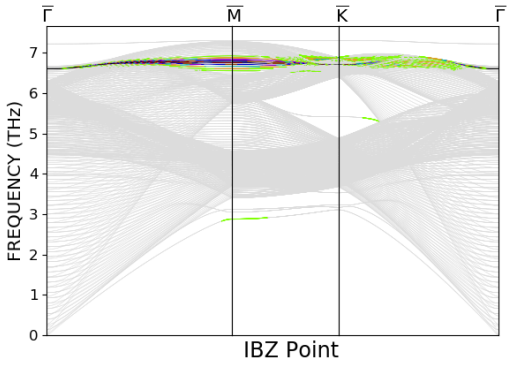

(a) Alkali layer longitudinal polarization

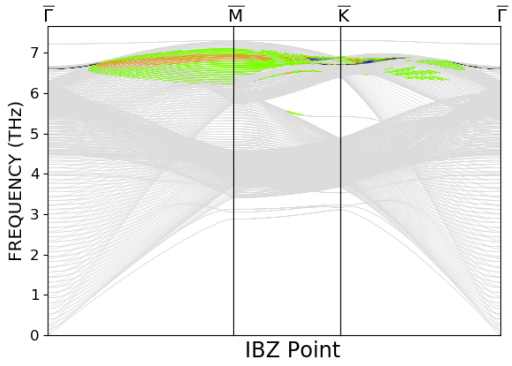

(b) Alkali layer shear horizontal polarization

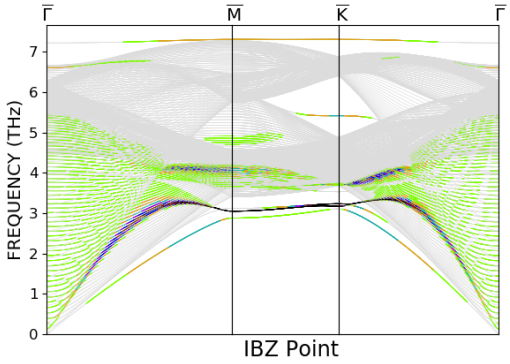

(c) First substrate layer longitudinal polarization

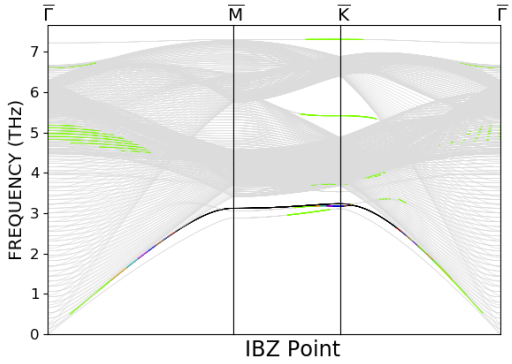

(d) First substrate layer shear horizontal polarization

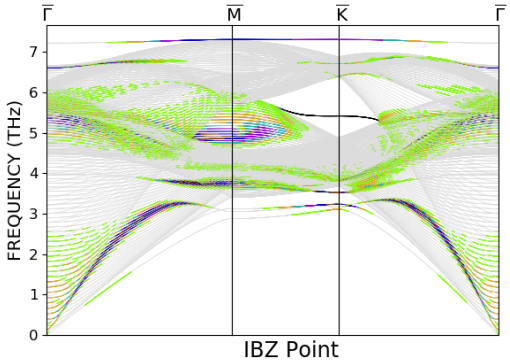

(e) Second substrate layer longitudinal polarization

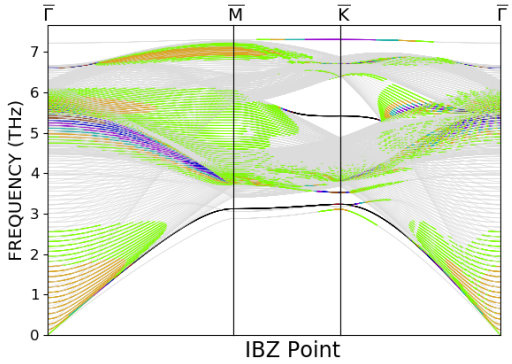

(f) Second substrate layer shear horizontal polarization

Figure 5.52. Dispersion curves for a full monolayer of Na on the 111 surface of W. Longitudinal (shear horizontal) projections are shown on the left (right).

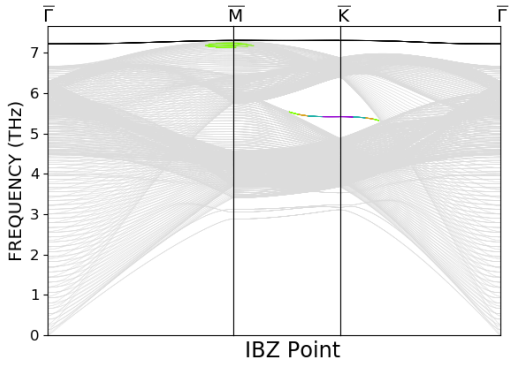

(a) Alkali layer shear vertical polarization

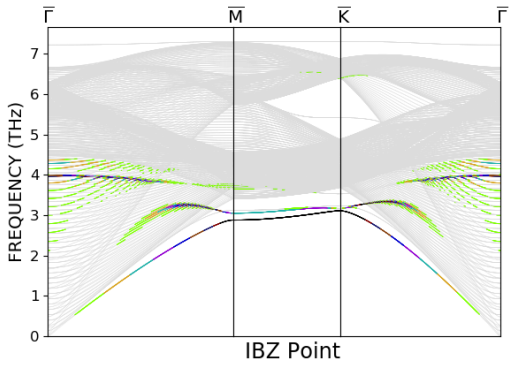

(b) First substrate layer shear vertical polarization

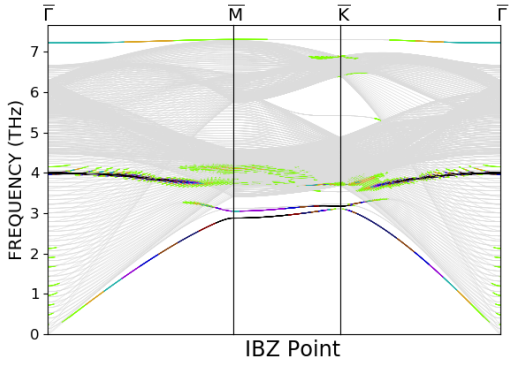

(c) Second substrate layer shear vertical polarization

Figure 5.53. Dispersion curves for a full monolayer of Na on the 111 surface of W projected in the shear vertical direction.

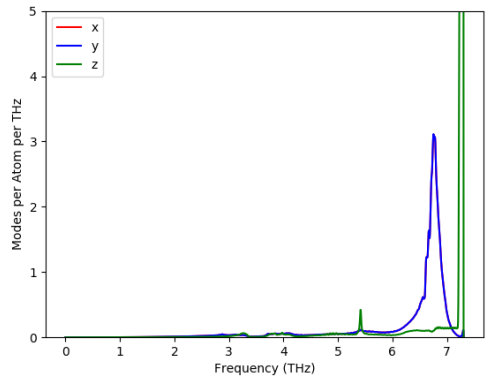

(a) Alkali layer density of states

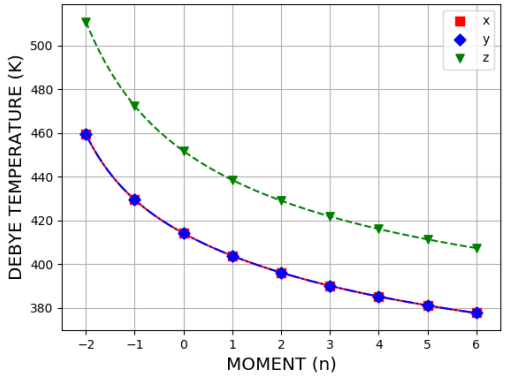

(b) Alkali layer Debye tempteratures

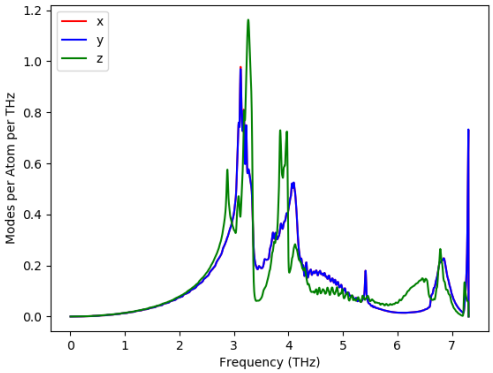

(c) First substrate layer density of states

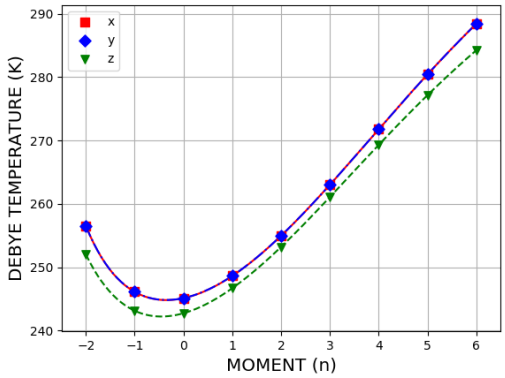

(d) First substrate layer Debye tempteratures

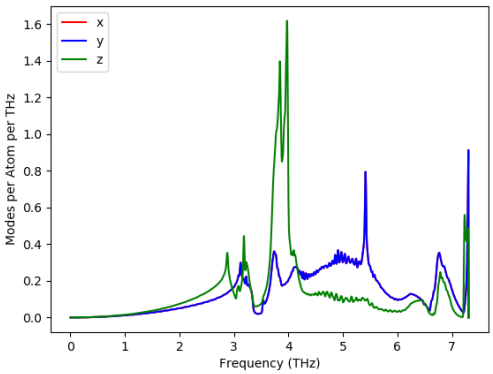

(e) Second substrate layer density of states

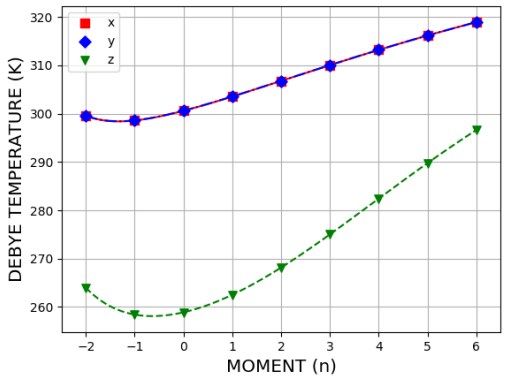

(f) Second substrate layer Debye tempteratures

Figure 5.54. Densities of states and Debye temperatures for a full monolayer of Na on the (111) surface of W, projected on to the x, y, and z directions.

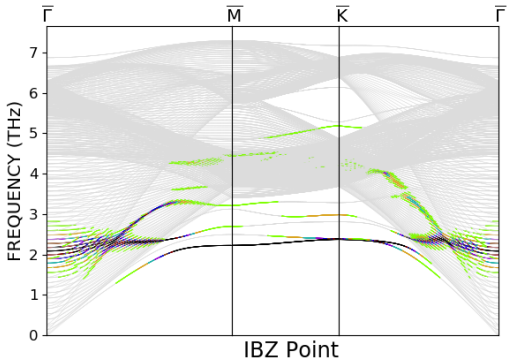

(a) Alkali layer longitudinal polarization

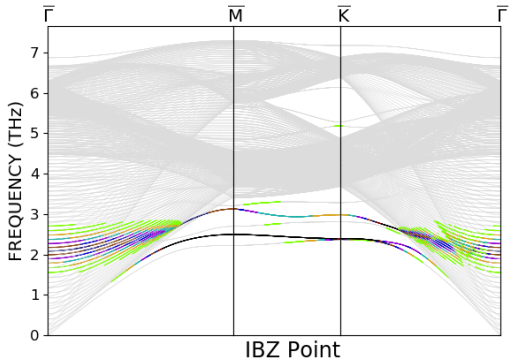

(b) Alkali layer shear horizontal polarization

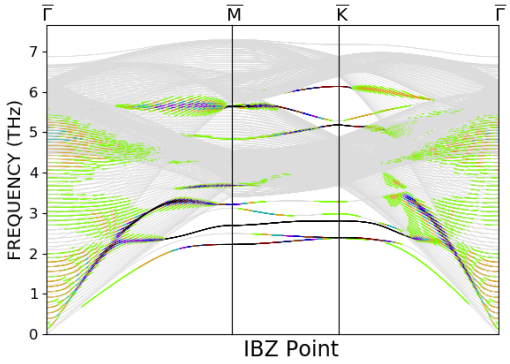

(c) First substrate layer longitudinal polarization

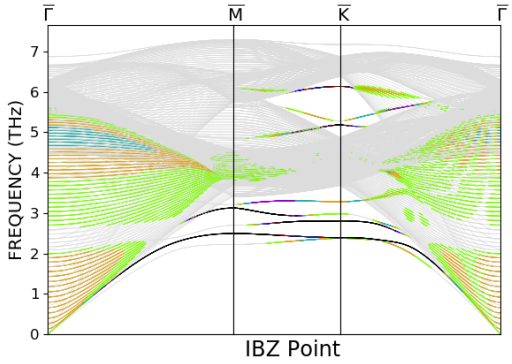

(d) First substrate layer shear horizontal polarization

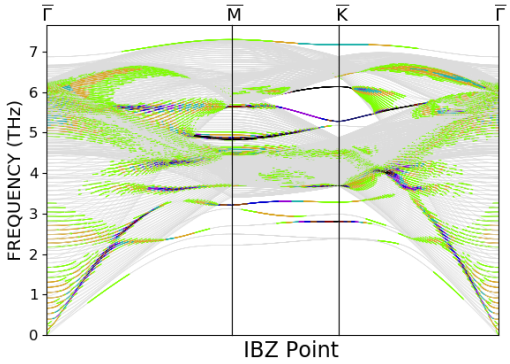

(e) Second substrate layer longitudinal polarization

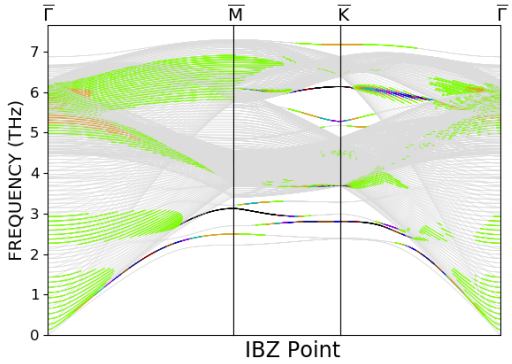

(f) Second substrate layer shear horizontal polarization

Figure 5.55. Dispersion curves for a full monolayer of K on the 111 surface of W. Longitudinal (shear horizontal) projections are shown on the left (right).

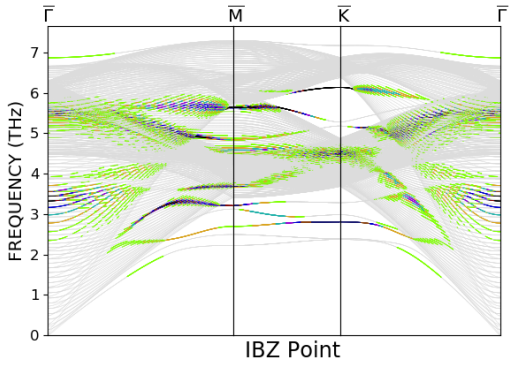

(a) Alkali layer shear vertical polarization

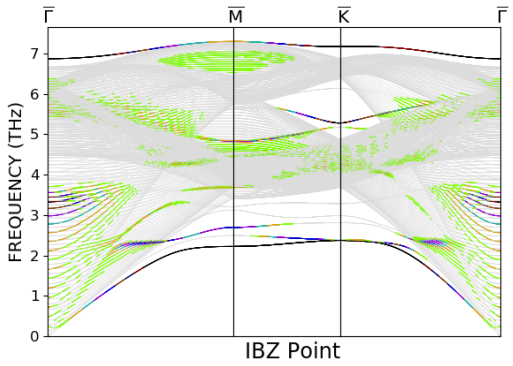

(b) First substrate layer shear vertical polarization

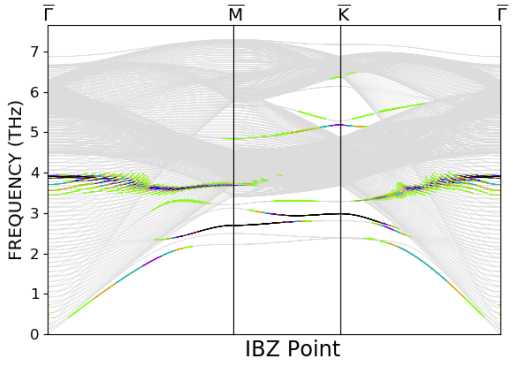

(c) Second substrate layer shear vertical polarization

Figure 5.56. Dispersion curves for a full monolayer of K on the 111 surface of W projected in the shear vertical direction.

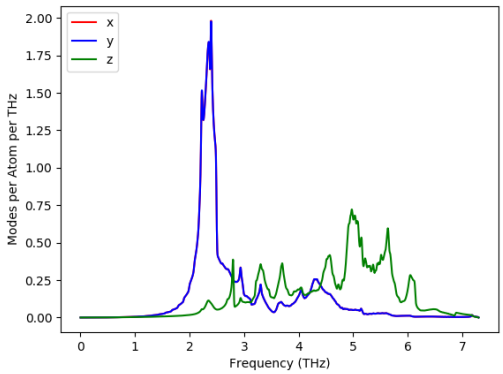

(a) Alkali layer density of states

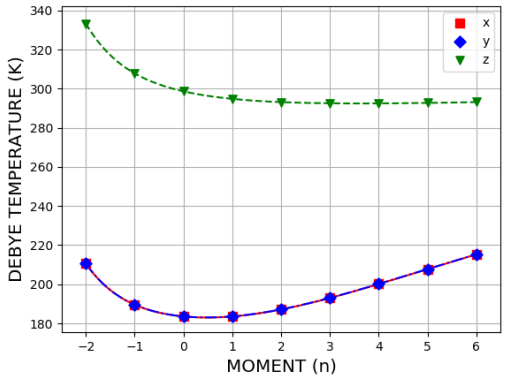

(b) Alkali layer Debye tempteratures

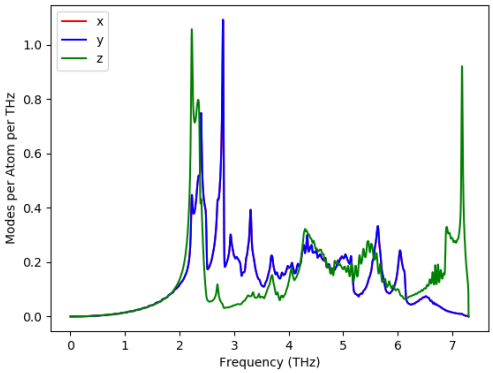

(c) First substrate layer density of states

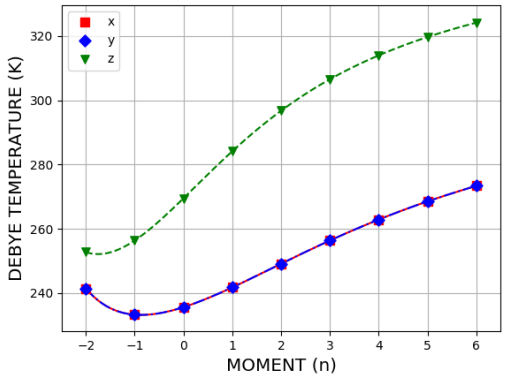

(d) First substrate layer Debye tempteratures

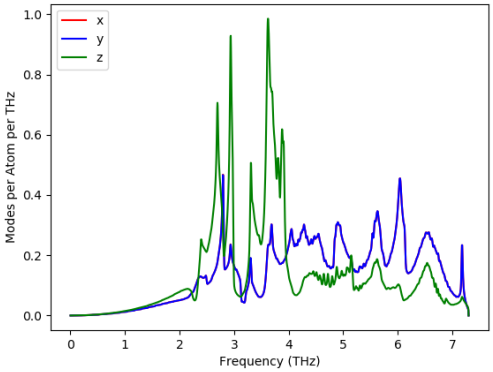

(e) Second substrate layer density of states

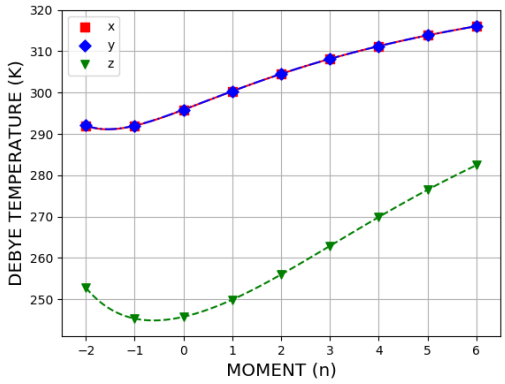

(f) Second substrate layer Debye tempteratures

Figure 5.57. Densities of states and Debye temperatures for a full monolayer of K on the (111) surface of W, projected on to the x, y, and z directions.

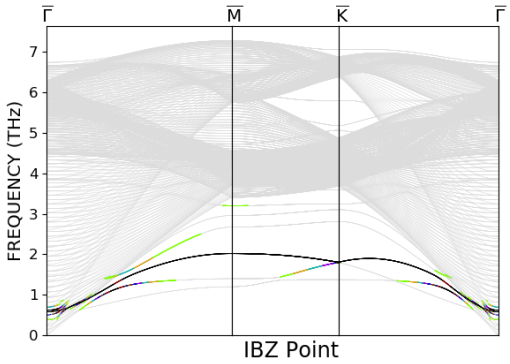

(a) Alkali layer longitudinal polarization

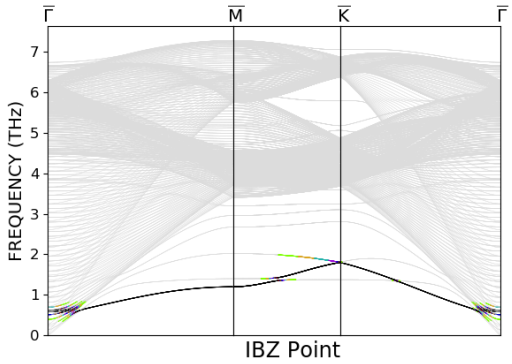

(b) Alkali layer shear horizontal polarization

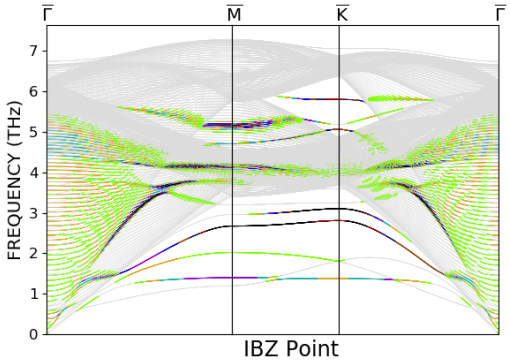

(c) First substrate layer longitudinal polarization

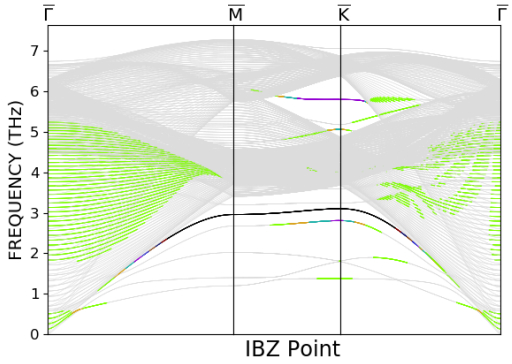

(d) First substrate layer shear horizontal polarization

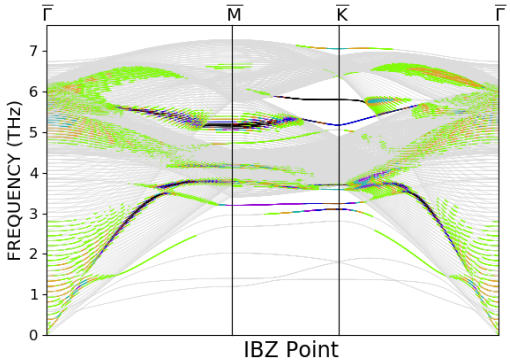

(e) Second substrate layer longitudinal polarization

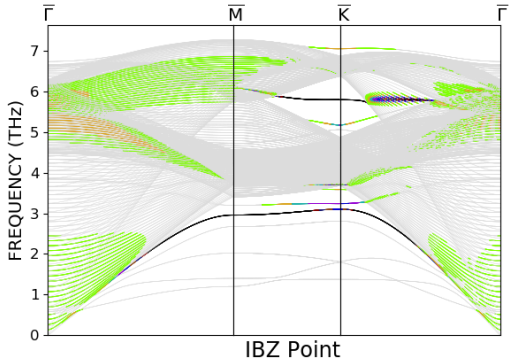

(f) Second substrate layer shear horizontal polarization

Figure 5.58. Dispersion curves for a full monolayer of Cs on the 111 surface of W. Longitudinal (shear horizontal) projections are shown on the left (right).

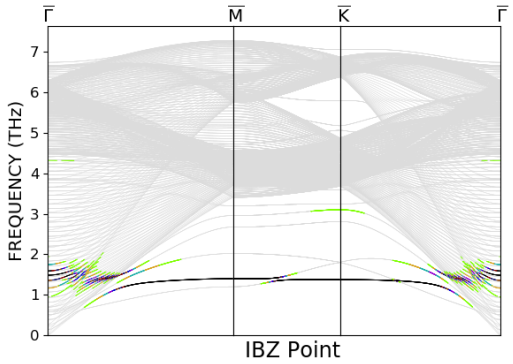

(a) Alkali layer shear vertical polarization

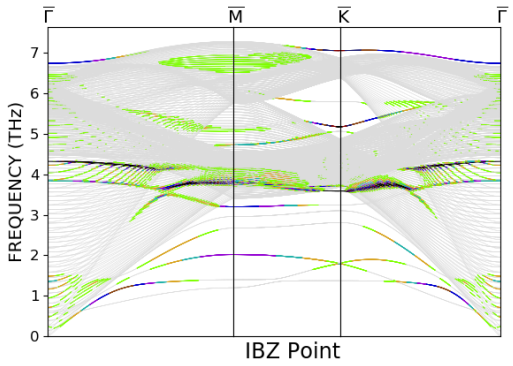

(b) First substrate layer shear vertical polarization

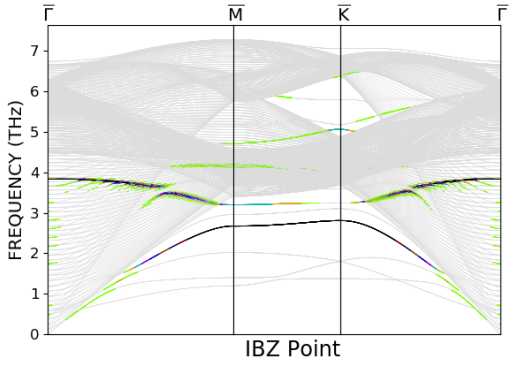

(c) Second substrate layer shear vertical polarization

Figure 5.59. Dispersion curves for a full monolayer of Cs on the 111 surface of W projected in the shear vertical direction.

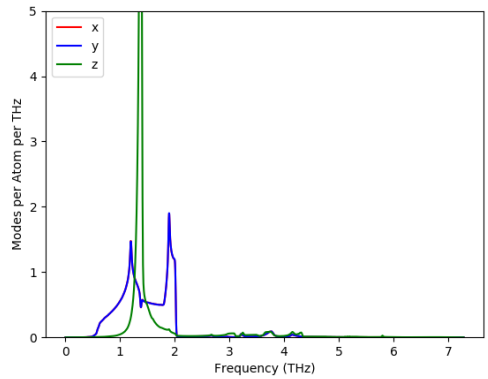

(a) Alkali layer density of states

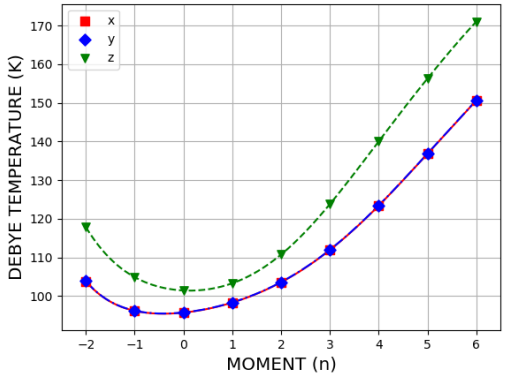

(b) Alkali layer Debye tempteratures

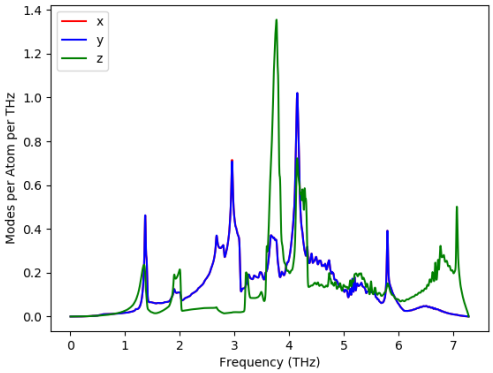

(c) First substrate layer density of states

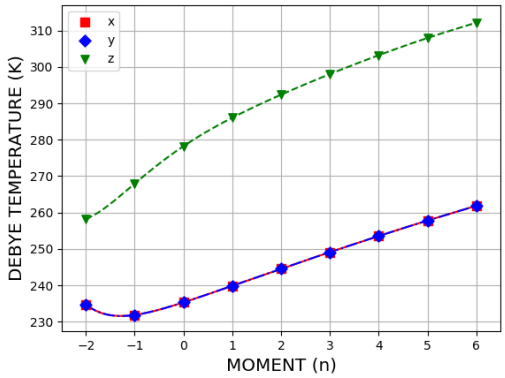

(d) First substrate layer Debye tempteratures

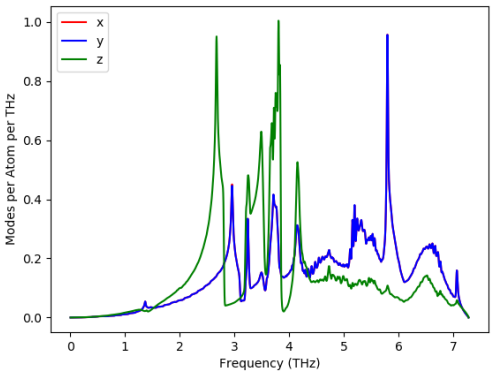

(e) Second substrate layer density of states

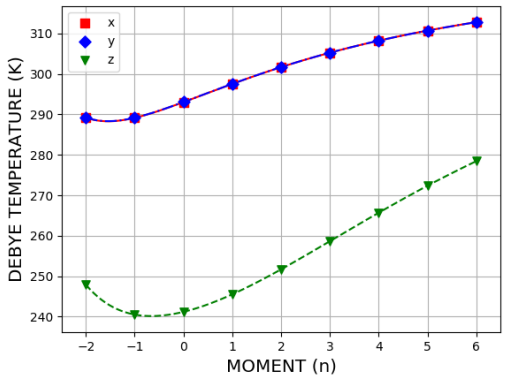

(f) Second substrate layer Debye tempteratures

Figure 5.60. Densities of states and Debye temperatures for a full monolayer of Cs on the (111) surface of W, projected on to the x, y, and z directions.

Once again, we summarize the above results by examining the modes obtained when freezing the W substrate and only allowing the K atoms to be dynamic, as well as the height of the K layer and the binding energy of the K layer. These results are shown in Table 5.3.

Table 5.3. Calculated frequencies, binding energies, and K layer heights for a full monolayer of Li, Na, K, and Cs on the (111) surface of W.

Alkali	h (ang)	E_{coh} (eV)	ν_1 (THz)	ν_2 (Thz)	ν_3 (Thz)
Li	1.29	3.22	10.56	10.56	10.70
Na	1.56	3.58	6.31	6.31	6.92
K	2.67	2.26	2.24	2.24	4.78
Cs	2.92	1.80	0.79	0.79	1.94

We see that the height of the K layer on the (111) surface is signifigantly lower than the K layer on the (100) surface. We also see that the Li layer height on the (111) surface is much less than its heights on the (110) surface. This difference is due to the (111) surface being much less dense than the other surfaces. The relative density of the (111) surface also explains the lower in-plain modes we see in Table 5.3.

5.4. Summary

There are a few key features we can extract from the numerous results above. These include the high dispersion of the full monolayer of Li on W and Mo (110) when compared to the other coverages, the mixing of the vertical modes of the alkali atoms with the bulk modes, and the new resonance modes observed in the bimetallic systems.

First, we see that the full monolayer of Li on the (110) surfaces of W and Mo show far more dispersion in the alkali layer than any of the other systems (see Figures 5.15 and 5.16). This indicates that, in the case of a full monolayer of Li on W and Mo (110), the Li atoms are interacting very strongly with each other. However, all the other systems showed nearly flat dispersion curves for the alkali layers. Therefore, we can conclude that in these systems, the alkali metals are only weakly interacting, if at all. This suggests that the most influential part of

our models are the heterogeneous potential energy functions, as these functions will dominate the dynamics of the alkali atoms.

Second, we see a significant difference in the alkali layer density of states of alkali atoms whose vertical modes coincide with the substrate. Consider the density of states of Li on W(111) in Figure 5.51. We see a sharp spike in the z-direction density of states at 10.7 THz, corresponding to the vertical mode. However, in the K on W(111) density of states, the z-direction projection is much more spread out. This suggest heavy mixing of the modes between the alkali and substrate atoms in the K-W and Cs-W systems, and to a small extent the Na-W system.

The third key feature in these results is a subtle change in the projection of modes onto the first substrate layer. We consistently see a significant projection of modes on this layer which are of the same frequency as the alkali layer. This suggests that the substrate and alkali layers are resonating together, and therefore considerably alters the vibrational properties of a clean surface.

This resonance can most clearly be seen by examining the densities of states. Consider the first layer clean surface density of states of W(100), shown in Figure 5.37, compared to a half monolayer of K on W(100) shown in Figure 5.43. In the bimetallic system, we see a significant spike in the density of states projected onto the first substrate layer at around 2.8 and 3.2 THz, which is where the alkali layer also sees a spike. This spike is not present in the clean surface, and therefore represents an emergent features of the bimetallic system.

CHAPTER 6
CONCLUSIONS

The goal of this project was to model the vibrational properties of the alkali-metal/transition-metal interface using the Embedded Atom Method (EAM) framework. Specifically, we sought to study adsorbed layers of alkali metals on the (100), (110), and (111) surfaces of tungsten and molybdenum substrates. The results of pursuing this goal can be split into four important contributions. First, we have developed a computer program which is able to perform the calculations necessary to describe the vibrational properties of a wide variety of crystal lattices and materials. Second, we have developed simple two-shell potential energy models to describe the bulk interactions of the alkali metals, as well as tungsten and molybdenum. Third, we have developed heterogeneous potential energy models to describe the interaction between tungsten or molybdenum atoms with alkali atoms. Finally, we have used the tools developed in this work to calculate the vibrational properties of transition-metal substrates with adsorbate layers of alkali metals.

When this project began, all of the calculations were done using previously developed Matlab code. This code was only able to perform calculations for bulk BCC, FCC, and HCP lattices, as well as BCC surfaces. Our new computer program, which we call Alkali Lattice Explorer (ALE), has several key advantages over its predecessors. First, it has been designed to perform calculations on an arbitrary lattice. To produce this lattice-agnostic program, we developed the mathematics of the vibrational properties of a lattice without making any assumptions about the symmetry of the underlying lattice. We formalized this mathematics in a previously published paper [19]. Our new approach allows us to calculate the vibrational properties of any lattice by only specifying the primitive vectors which describe the lattice, and the basis vectors which describe the arrangement of the atoms in the unit cell. Importantly, our approach generalizes to crystal surfaces, giving us the tools we need to describe the alkali-metal/transition-metal interface.

Second, ALE runs much more quickly than the old Matlab code. The reduction in computation time comes from two sources. First, ALE is written in Fortran, a compiled language which easily outperforms the scripted Matlab language. Second, and most importantly, ALE runs many of its key algorithms in parallel. This has allowed us to do far more complex calculations that would have taken a prohibitively long time using the old Matlab code.

We used a previously developed model of the embedding energy portion of the EAM model [29] for the alkali metals, as well as tungsten and molybdenum. We also used Hartree Fock calculations to accurately describe the electron charge density contribution of the alkali and transition metals [26]. Both of these functions are required for a full EAM model.

Our original approach to modeling the potential interaction between alkali and transition metals was the Johnson prescription [72], which has been widely used to describe alloy systems. This prescription builds the heterogeneous potential out of the homogeneous potentials describing the bulk interactions. Accordingly, we developed simple two-shell potential models for all of the alkali metals, as well as tungsten and molybdenum. We chose simple short range models over more accurate long range five-shell models in order to avoid over-fitting. Since little is known about the precise form of the potential interaction between alkali metals and tungsten and molybdenum, we decided that using the simplest possible potential energy model would introduce the least chance of imposing false structure on the interaction.

From our homogeneous potentials, we then constructed the heterogeneous potential. However, our attempt at the Johnson prescription showed that, although the prescription worked well for lithium on tungsten and molybdenum, the larger alkali metals performed poorly, with the performance getting worse as the alkali atoms got larger. Specifically, the Johnson prescription predicted frequencies much higher than was expected, as well as predicting unreasonable binding energies and alkali layer heights.

To remedy this problem, we attempted a slight variation of the Johnson prescription. We attempted to describe the heterogeneous potential interaction between an alkali metal and tungsten or molybdenum as a simple linear combination of the homogeneous potentials of the substrate and adsorbate layer. We fit the coefficients of the linear combination to heuristically

derived target model outputs of the frequencies obtained when holding the substrate fixed and only allowing the alkali layer be dynamic, as well as target alkali binding energies and alkali layer heights. However, we found that the same problems that plagued the Johnson prescription persisted in the linear combination approach. Our analysis suggests that the cause of this problem is the large difference in potential well positions of the homogeneous potentials. This also explains why the lithium/transition metal systems performed well with both the Johnson prescription and linear combination approach; since lithium atoms are around the same size as tungsten and molybdenum atoms, their homogeneous potential energies have wells in approximately the same locations, thus avoiding the problem we discovered.

In order to accurately model the interaction between the alkali metals and tungsten and molybdenum, we decided to use a simple short range model developed by Zhou *et. al* [43], which we call the ZWJ potential. This model was fit to the target outputs we used to test the Johnson prescription and linear combination approach. The ZWJ potential model outperformed the Johnson prescription and linear combination approach in all tested cases, and was therefore chosen to model our chosen systems.

Finally, we have used the ZWJ heterogeneous potential to calculate dispersion curves, densities of states, Debye temperatures, adsorbate layer heights and binding energies of a variety of systems. These systems include lithium on the (110) surface of tungsten in coverages of a full, third, quarter, and sixth monolayer, potassium on the (100) surface of tungsten in coverages of a half and quarter monolayer, and lithium sodium, potassium, and cesium on the (111) surface of tungsten using a full monolayer. These results are tabulated in chapter five of this thesis. We found that, with the exception of the full monolayer of Li on W (110), the alkali atoms forming the adsorbate layer interacted very weakly with each other, which indicates that the dynamics of the alkali layer are mostly driven by the alkali/transition metal interaction. We also consistently saw resonance modes appear in the first substrate layer of the bimetallic systems which were not present in the clean surface calculations.

Moving forward, we hope to use the tools developed throughout this research project to model more bimetallic systems. Understanding the vibrational properties of alkali-metal/transition-

metal interfaces gives deep insight into the thermal properties of these systems. Our work here contributes to the understanding of effective modeling of these systems.

REFERENCES

[1] Salaway R, Hopkins P, Norris P and Stevens R 2008 *International Journal of Thermophysics* **29** 1987–1996

[2] Kang H, Zhang Y and Yang M 2011 *Applied Physics A* **103** 1001

[3] Evteev A V, Momenzadeh L, Levchenko E V, Belova I V and Murch G E 2015 *Computational Materials Science* **96** 229–236

[4] Lipschultz B, Pappas D, LaBombard B, Rice J, Smith D and Wukitch S 2001 *Nuclear Fusion* **41** 585

[5] Dux R, Bobkov V, Herrmann A, Janzer A, Kallenbach A, Neu R, Mayer M, Müller H, Pugno R, Pütterich T *et al.* 2009 *Journal of Nuclear Materials* **390** 858–863

[6] Kaufmann M and Neu R 2007 *Fusion Engineering and Design* **82** 521–527

[7] Johnson D F and Carter E A 2010 *Journal of Materials Research* **25** 315–327

[8] Yi S, Li G, Liu Z, Hu W and Deng H 2018 *Plasma Physics Reports* **44** 692–701

[9] Wertheim G, Riffe D M and Citrin P 1994 *Physical Review B* **49** 2277

[10] Medvedev V, Naumovets A and Fedorus A 1970 Structure and adsorption behavior of sodium films on (011) faces of tungsten. Tech. rep. Inst. of Physics, Kiev

[11] Fedorus A and Naumovets A 1970 *Surface Science* **21** 426–439

[12] Mlynczak A and Niedermayer R 1975 *Thin Solid Films* **28** 37–58

[13] Steinhage P and Mayer H 1975 *Thin Solid Films* **28** 131–147

[14] MacRae A, Müller K, Lander J, Morrison J and Phillips J 1969 *Physical Review Letters* **22** 1048

[15] Naumovets A 1994 Two-dimensional phase transitions in alkali-metal adlayers *The Chemical Chysics of Solid Surfaces* vol 7 (Elsevier) pp 163–213

[16] Vitek V 1996 *MRS Bulletin* **21** 20–23

[17] King D A 2012 *The chemical physics of solid surfaces and heterogeneous catalysis* vol 5 (Elsevier)

[18] Li J, Dai X, Liang S, Tai K, Kong Y and Liu B 2008 *Physics Reports* **455** 1–134

[19] Riffe D M, Christensen J D and Wilson R B 2018 *Journal of Physics: Condensed Matter* **30** 455702

[20] Anderson E, Bai Z, Bischof C, Blackford S, Demmel J, Dongarra J, Du Croz J, Greenbaum A, Hammarling S, McKenney A and Sorensen D 1999 *LAPACK Users' Guide* 3rd ed (Philadelphia, PA: Society for Industrial and Applied Mathematics) ISBN 0-89871-447-8 (paperback)

[21] OpenMP Architecture Review Board 2008 OpenMP application program interface version 3.0

[22] Powell M J 1994 A direct search optimization method that models the objective and constraint functions by linear interpolation *Advances in optimization and numerical analysis* (Springer) pp 51–67

[23] Johnson R and Oh D 1989 *Journal of Materials Research* **4** 1195–1201

[24] Hu W and Masahiro F 2002 *Modelling and Simulation in Materials Science and Engineering* **10** 707

[25] Guellil A and Adams J 1992 *Journal of materials research* **7** 639–652

[26] Mann J B 1968 Atomic structure calculations. II. hartree-fock wavefunctions and radial expectation values: Hydrogen to lawrencium. Tech. rep. Los Alamos Scientific Lab., N. Mex.

[27] Kittel C 2004 *Introduction to Solid State Physics* 8th ed (Wiley) ISBN 9780471415268

[28] Wang Y and Boercker D 1995 *Journal of applied physics* **78** 122–126

[29] Wilson R and Riffe D M 2012 *Journal of Physics: Condensed Matter* **24** 335401

[30] Finnis M and Sinclair J 1984 *Philosophical Magazine A* **50** 45–55

[31] Smith H, Dolling G, Nicklow R, Vijayaraghavan P and Wilkinson M 1968 Phonon dispersion curves in lithium *Neutron Inelastic Scattering Vol. I. Proceedings of a Symposium on Neutron Inelastic Scattering*

[32] Woods A, Brockhouse B, March R, Stewart A and Bowers R 1962 *Physical Review* **128** 1112

[33] Cowley R, Woods A and Dolling G 1966 *Physical Review* **150** 487

[34] Copley J and Brockhouse B 1973 *Canadian Journal of Physics* **51** 657–675

[35] Nücker N and Buchenau U 1985 *Physical Review B* **31** 5479

[36] Bohnen K P 1984 *Surface Science* **147** 304–328

[37] Sklyadneva I Y, Chulkov E and Bertsch A 1996 *Surface science* **352** 25–31

[38] Kokko K, Salo P, Laihia R and Mansikka K 1995 *Physical Review B* **52** 1536

[39] Rodach T, Bohnen K and Ho K M 1989 *Surface Science* **209** 481–491

[40] Bohnen K P 1982 *Surface Science* **115** L96–L102

[41] Quong A, Maradudin A, Wallis R, Gaspar J, Eguiluz A and Alldredge G 1991 *Physical review letters* **66** 743

[42] Ryu S and Cai W 2008 *Modelling and Simulation in Materials Science and Engineering* **16** 085005

[43] Zhou X, Wadley H, Johnson R A, Larson D, Tabat N, Cerezo A, Petford-Long A, Smith G, Clifton P, Martens R *et al.* 2001 *Acta materialia* **49** 4005–4015

[44] Oh D J and Johnson R A 1988 *Journal of Materials Research* **3** 471–478

[45] Larose A and Brockhouse B 1976 *Canadian Journal of Physics* **54** 1819–1823

[46] Buyers W, Powell B and Woods A 1972 *Canadian Journal of Physics* **50** 3069–3070

[47] Buchholz J, Wang G C and Lagally M 1975 *Surface Science* **49** 508–528

[48] Van Hove M and Tong S 1976 *Surface Science* **54** 91–100

[49] Smith R, Hennessy C, Kim M, Whang C, Worthington M and Mingde X 1987 *Physical review letters* **58** 702

[50] Arnold M, Sologub S, Hupfauer G, Bayer P, Frie W, Hammer L and Heinz K 1997 *Surface Review and Letters* **4** 1291–1295

[51] Teeter G, Erskine J, Shi F and Van Hove M 1999 *Physical Review B* **60** 1975

[52] Meyerheim H, Sander D, Popescu R, Steadman P, Ferrer S and Kirschner J 2001 *Surface science* **475** 103–108

[53] Lee B, Ignatiev A, Tong S and VanHove M 1977 *Journal of Vacuum Science and Technology* **14** 291–293

[54] Debe M, King D A and Marsh F 1977 *Surface Science* **68** 437–447

[55] Kirschner J and Feder R 1979 *Physical Review Letters* **42** 1008

[56] Feder R 1981 *Journal of Physics C: Solid State Physics* **14** 2049

[57] Altman M, Estrup P and Robinson I 1988 *X-ray diffraction study of multilayer W (001) surface reconstruction* Ph.D. thesis American Vacuum Society

[58] de la Garza L M and Clarke L 1981 *Journal of Physics C: Solid State Physics* **14** 5391

[59] Methfessel M, Hennig D and Scheffler M 1992 *Physical Review B* **46** 4816

[60] Brejnak M and Modrak P 1994 *Surface science* **310** L614–L620

[61] Moriarty J A and Phillips R 1991 *Physical review letters* **66** 3036

[62] Foiles S 1993 *Physical Review B* **48** 4287

[63] Lee B J, Baskes M, Kim H and Cho Y K 2001 *Physical Review B* **64** 184102

[64] Ackland G and Finnis M 1986 *Philosophical Magazine A* **54** 301–315

[65] Ignatiev A, Jona F, Shih H, Jepsen D and Marcus P 1975 *Physical Review B* **11** 4787

[66] Overbury S 1986 *Surface Science* **175** 123–140

[67] Arnold M, Fahmi A, Frie W, Hammer L and Heinz K 1999 *Journal of Physics: Condensed Matter* **11** 1873

[68] Che J, Chan C, Jian W and Leung T 1998 *Physical Review B* **57** 1875

[69] Balden M, Lehwald S, Preuss E and Ibach H 1994 *Surface science* **307** 1141–1147

[70] Kröger J, Lehwald S and Ibach H 1997 *Physical Review B* **55** 10895

[71] Fu T, Peng X, Chen X, Weng S, Hu N, Li Q and Wang Z 2016 *Scientific reports* **6** 35665

[72] Johnson R 1989 *Physical Review B* **39** 12554

[73] Zhou Y, Smith R, Kenny S D and Lloyd A L 2017 *Nuclear Instruments and Methods in Physics Research Section B: Beam Interactions with Materials and Atoms* **393** 122–125

[74] Davoodi J, Dadashi S and Yarifard M 2016 *Philosophical Magazine* **96** 2300–2310

[75] Ren G and Sehitoglu H 2016 *Computational Materials Science* **123** 19–25

[76] Zhou Y, Zu X, Nie J and Xiao H 2009 *Surface Review and Letters* **16** 589–597

[77] Kröger J, Bruchmann D, Lehwald S and Ibach H 2000 *Surface science* **449** 227–235

[78] Vella J R, Chen M, Fürstenberg S, Stillinger F H, Carter E A, Debenedetti P G and Panagiotopoulos A Z 2017 *Nuclear Fusion* **57** 116036

[79] Müller J, Dahmen K and Ibach H 2002 *Physical Review B* **66** 235407

[80] Kawano H 2008 *Progress in surface science* **83** 1–165

[81] Lopinski G and Estrup P 1996 *Surface science* **365** 149–158